

https://dspace.org/

The aqueous electrophoretic deposition (EPD) of diamond-diamond laminates

Džepina, Branislav

2013-02-11
http://hdl.handle.net/10539/12410

Downloaded from a DSpace repository. https://dspace.org/

THE AQUEOUS ELECTROPHORETIC DEPOSITION (EPD) OF DIAMOND-DIAMOND LAMINATES

Branislav Džepina

A Dissertation submitted to the Faculty of Engineering and the Built Environment, University of the Witwatersrand, in fulfilment of the requirements of the degree of Master of Science in Engineering

June 2012

i. Declaration

I declare that this dissertation is my own unaided work. It is being submitted for the degree of Master of Science in Engineering to the University of the Witwatersrand, Johannesburg. It has not been submitted before for any degree or examination to any other University.

_____
Branislav Dzepina

_____ day of _____ 2012

ii. Abstract

It is known that the wear resistance of polycrystalline diamond (PCD) is inversely proportional to the particle size of the diamond powder which is to be sintered. Fracture toughness on the other hand is directly proportional to the particle size of the starting powder. Therefore, fracture toughness and wear resistance work antagonistically. A layered PCD structure made by using powders with a relatively small particle size could result in a more fracture resistant cutter while still retaining desirable wear properties. The focus of this project was to determine if a layered diamond structure could be made by electrophoretic deposition (EPD) and whether the sintered laminate showed crack deflection during fracture.

The aqueous EPD of a diamond/diamond laminate with two alternating grades of diamond was investigated. Diamond particles, 0.5µm and 2µm in size, were deposited in an alternating manner onto tungsten carbide substrate. The layered diamond deposit was sintered with the carbide substrate in a high-pressure, high-temperature press. The sintered deposit was examined for evidence of alternating residual stresses. Differences of cobalt content in the 0.5 and 2µm layers were observed by EDS and image analysis.

The sintered diamond laminate was subjected to three-point bending until fracture. Although the sample had demonstrated only minimal crack deflection during the bend test, further analysis revealed that a sintering cooling crack showed evidence of crack deflection.

iv. Acknowledgements

I would like to express my gratitude to the following for their contribution to this body of work:

1) God who blessed me with this wonderful opportunity
2) Prof. I. Sigalas for supervising the research
3) Dr. M. Herrmann for his much appreciated contribution to this body of work
4) DST/NRF Centre of Excellence in Strong Materials for their financial support of this project
5) The staff at Element 6 (Pty) Ltd. Namely Dr. R. Nilen for his interest in the project and Mr. K. Kekana for all his assistance with sintering
6) BV Profiling for building and programming the robotic arm
7) My colleagues Ms. A. McKie and Mr. P. Bush for their invaluable input and assistance
8) My parents Nikola and Ivanka, my friends, and the rest of my family for their support and inspiration
9) Daniela for her continual love, encouragement and understanding

v. List of figures

Figure 1.1: Schematic diagram showing the alternating layers of 0.5µm and 2µm grade diamond on a carbide substrate. 3
Figure 2.1: a) Longitudinal and b) cross-section microstructure of the fibrous monolithic Si_3N_4/BN resembling the structure of bamboo [2] 5
Figure 2.2: Typical load-displacement curve of fibrous monolithic Si3N4/BN showing the plots for extruded fibres of diameter 1mm, 0.5mm and 0.3mm. [2] 6
Figure 2.3: Dumbbell-like SiC whiskers resembling bone. [14] 7
Figure 2.4: a) Microstructure of vapor-grown carbon fibers resembling tree roots b) structure of a branching point [16] 8
Figure 2.5: An SEM image of the micro-structure of nacre [19] 9
Figure 2.6: Typical EPD setup. 10
Figure 2.7: Diagram of the double layer surrounding a charged particle. The potential at the surface of shear is termed the zeta potential. It is the main parameter determining electro-kinetic behaviour [24]. 13
Figure 2.8: Diagram of the typical EPD setup for aqueous deposition with a membrane between the two electrodes [30]. 18
Figure 2.9: Alpha-Al_2O_3 deposits formed using (a) 100 V DC for 1200 s and (b) a 50 Hz asymmetric AC field with an amplitude of 500 V_{p-p} [34]. 19
Figure 2.10: SEM picture of the diamond deposit obtained using an isopropanol suspension with acetone, iodine and water as additives [33] 20
Figure 2.11: Boundaries between the sintered alumina/zirconia laminates by Sarkar and Nicholson [37]. 21
Figure 2.12: SEM image showing the pressureless sintered SiC/TiC laminates achieved by You et al. [38] 22
Figure 2.13: Alumina/zirconia laminates prepared by EPD using a suspension of each of the materials with 0.6% deflocculant [39] 23
Figure 2.14: SEM micrograph of a typical PCD sintered at 8.5GPa and 1400ºC [45]. 26

Figure 2.15: SEM of the micro-structure of the cross section of a PCD sintered compact made using 2µm diamond powder exhibiting AGG. [46]..... 27
Figure 2.16: Schematic of a functionally graded material achievable by particle agitation [50]..... 29
Figure 2.17: Another schematic of a functionally graded material achievable by the agitation of multimodal powders [50]..... 30
Figure 2.18: Illustration of the expected crack path through the sintered layered material. 31
Figure 3.1: Particle size distribution of AKP-50 alumina..... 34
Figure 3.2: Particle size distribution of diamond powders used. 34
Figure 3.3: Schematic of the working electrode used for alumina deposition..... 39
Figure 3.4: Schematic showing the experimental setup of both the working electrode and the counter-electrode. 40
Figure 3.5: Robotic arm to automate movement of electrodes between two different suspensions for laminate deposits. 41
Figure 3.6: A typical HPHT assembly used for the sintering of PCD. 1) Pyrophyllite disc, 2) Mo end disc, 3) alumina disc, 4) Crucible, 5) salt nest, 6) WC-Co substrate, 7) diamond powder, 8) Nb cup and Ta double-cup, 9) current ring, 10) graphite heater, 11) pyrophyllite case. Adapted from [46]. 43
Figure 3.7: A picture of the Malvern Nanosizer with the auto-titrator and pH meter on the right. 47
Figure 3.8: Schematic of the 3-point bend jig apparatus used to produce a controlled crack. 51
Figure 4.1: A typical electrode after deposition. This deposit was made at pH 5.7, 10% (w/v) alumina in isopropanol, 10 min at 100V/cm. 54
Figure 4.2: Effect of PEG-400 addition on the formation of cracks in the deposit. Weight per cent PEG-400 addition to suspension: a) 0% b) 0.1% c) 0.2% d) 0.3% e) 0.4%. 56
Figure 4.3: A graph showing the weight of the deposit versus % PEG-400 addition. Deposits were made using 175V/cm, 10% (w/v) for 1 hour..... 57

Figure 4.4: A schematic of the side view of the electrode illustrating the trapped isopropanol underneath the membrane. 58
Figure 4.5: Deposit weight versus applied voltage for a suspension of pH 5.0, 10% (w/v) for 15 minutes..... 59
Figure 4.6: Deposit weight versus time for a suspension of pH 5.0, 10% (w/v) at 100V/cm..... 60
Figure 4.7: Photograph showing Sample 41 prepared using a 10% (w/v) alumina suspended in isopropanol at pH 3.7, 50V/cm for 1 hour. 61
Figure 4.8: Photograph showing Sample 42 prepared using a 10% (w/v) alumina suspended in isopropanol at pH 3.7, 32.5V/cm for 1 hour. 62
Figure 4.9: SEM micrographs of sample 42 at a) 5000x b) 10000x magnification..... 63
Figure 4.10: FTIR spectra of as received (uncleaned), oxidized and acid washed 0.5µm powder superimposed for comparison of surface groups. 64
Figure 4.11: Zeta-potential measurements of as-received, acid cleaned as well as oxidized/acid cleaned powders plotted against time in isopropanol media. 66
Figure 4.12: Graph of zeta-potential versus pH for the various powders in aqueous media. 68
Figure 4.13: First diamond deposit obtained (Sample 47). The deposit was made using 3% (w/v), pH 8.5, 1.88 V/cm, 60 minutes. 70
Figure 4.14: SEM image of the fracture surface of a green deposit made using a 0.5µm diamond suspension with the same conditions as sample 50. 72
Figure 4.15: SEM image of the green deposit of a sample 53 made using a 2µm diamond suspension. 73
Figure 4.16: SEM of the cross section of sample 48 which was made by depositing 0.5µm diamond. 75
Figure 4.17: SEM of the cross section of sample 49 which was made by depositing 0.5µm diamond. 76
Figure 4.18: SEM of the cross section of sample 50. 77
Figure 4.19: SEM of the cross section of sample 51. 78
Figure 4.20: SEM of 0.5µm powder pressed standard. 79

Figure 4.21: SEM showing light and dark spots in the diamond table of the 0.5µm powder pressed standard. 80
Figure 4.22: SEM of the 2µm powder pressed standard. 81
Figure 4.23: SEM showing light and dark spots in the diamond table of the 2µm powder pressed standard. 82
Figure 4.24: SEM micrograph of the fracture surface of the interface between a 0.5µm and a 2µm grade layer in a green deposit. 83
Figure 4.25: Optical microscope picture of the diamond laminate sample showing the overall structure. 84
Figure 4.26: SEM micrograph of a uniform section showing the morphology of the layers. 85
Figure 4.27: EDS scans for the first 2µm layer (a) and the first 0.5µm layer (b) of the diamond laminate sample. 86
Figure 4.28: Comparison of polishing techniques: a) 0.5µm layer standard polish, b) 2µm layer standard polish, c) 0.5µm ion polish, 2µmion polish. 88
Figure 4.29: SEM Image analysis showing the phase thresh-holding for the 2µm layer in a) and b) and the 0.5µm layer in c) and d). 89
Figure 4.30: SEM micrograph of layer defects present in the diamond laminate. 91
Figure 4.31: Optical microscope picture showing damage sustained at the edge of the sample. 92
Figure 4.32: SEM showing the inclusion of larger grains in the fine grade layer. 93
Figure 4.33: An optical microscope picture showing the direction of a forced crack path. 94
Figure 4.34: Load vs. displacement graph of the sintered diamond laminate as recorded during 3-point bend testing. 95
Figure 4.35: SEM micrograph of a pre-existing crack showing crack deflection in the laminate material. 96
Figure 5.1: (Top) Mechanism of surface charging for alumina in ethanol. (Bottom) Effect of charged surface after the addition of HCl. [61] 99

Figure 5.2: Graph showing the difference between predicted and experimental yield of deposited Al_2O_3 from ethanol-HNO_3 suspensions using a constant voltage of 42.7V/cm [62]. 102
Figure 5.3: Effect of the shaping method and green density on the temperature effect on isothermal sintering for the same alumina powder [66]. 105
Figure 5.4: Some of the possible surface groups on diamond [59]. 106
Figure 5.5: Zeta-potential vs. pH plot for detonated nano-diamond treated with: a) perchloric acid; b) sulphuric acid and potassium permanganate; c) perchloric acid and 10^{-3} mol.dm^{-3} sodium oleate; d) sulphuric acid, potassium permanganate and 10^{-3} mol.dm^{-3} sodium oleate [68]. 109
Figure 5.6: The effects of Optapix polymer binder on the zeta-potential of 0.5µm acid washed diamond in water [75] 111
Figure 5.8: Illustration showing the effect of the cup tapering on the edges of the diamond laminate. 121
Figure 5.9: Schematic illustration of the compressive forces generated due to the mismatch in thermal expansion between the diamond and the substrate. 122
Figure 5.10: A schematic diagram showing the stress distribution in the layers..... 125

vi. List of tables

Table 1.1: Fracture toughness of representative ceramic materials. 1
Table 2.1: Summary of monolithic deposits obtained by EPD. 15
Table 2.2: Summary of laminate deposits obtained by EPD in literature. 24
Table 2.3: Comparison of linear thermal expansion coefficients for diamond and cobalt at room temperature. 31
Table 3.1: Ceramic powders used. 33
Table 3.2: Deposition substrates used. 35
Table 3.3: Grinding and polishing steps for sintered alumina deposits. 45
Table 3.4: Theoretical densities of the pure materials used in this project 49
Table 4.1: Various techniques attempted to facilitate crack-free drying of alumina deposits. 55
Table 4.2: EPD parameters for Sample 41 and 42. 61
Table 4.3: General properties of Sample 41 and 42 62
Table 4.4: Characteristic FTIR peaks present in diamond. 65
Table 4.5: Summary of the EPD attempts using isopropanol suspensions of 0.5µm diamond 67
Table 4.6: Summary of EPD experiments of non-layered samples performed at pH 8.5. 71
Table 4.7: Comparison of the green density, and open porosity of the 0.5 µm and 2µm green deposits 74
Table 4.8: Summary of EPD experiments of multi-layered samples deposited at pH 8.5 83
Table 4.9: Table showing the EDS results of the first four layers taken at a uniform area in the EPD laminate 87
Table 4.10: Table showing the phase composition of layers 3 and 4 as measured by image analysis. 90
Table 5.1: Comparison of alumina deposition rates and green density obtained in this work and literature. 103

Table 5.2: Comparison of monolayer and multilayer diamond deposition rates with literature. 114
Table 5.3: Summary of the various sintering experiments performed and whether AGG resulted. 116
Table 5.5: Table showing the comparison in phase analysis between EDS and image analysis for layers 3 and 4. 119
Table 5.6: Physical properties of PCD, WC-Co and Co. 123

vii. List of symbols

α- Thermal expansion coefficient m/m K)

$\bar{\alpha}$- Averaged thermal expansion co-efficient of the laminate(MPa or GPa)

AC- Alternating current

AGG- Abnormal grain growth

C- Suspension concentration (g/100mL)

d- Average length of the diagonals of the indent (mm)

DC- Direct current

E- Electric field (V or V/cm)

E_i- Young's Modulus (MPa or GPa)

ε_0- Permittivity of a vacuum (F/m)

ε_τ - Relative permittivity of the solvent.(F/m)

η- Viscosity of the liquid meda (Pa.S)

F- Force (N)

HPHT- High-pressure high-temperature

H_v- Vicker's Hardness (GPa)

k- Collective term for numerous constants

KIc- Fracture toughness ($MPa.m^{0.5}$)

l- Separation of the electrodes (cm)

m_w- Wet mass (g)

m_s- Suspended mass (g)

m_d- Dry mass (g)

N- Number of layers in a laminate

v_i- Poisson's Ratio of the i^{th} layer

NGG- Normal grain growth

P_{0-} Open porosity (%)

φ- Electrostatic potential

ρ- Density (g/cm^3)

$\sigma_{res,i}$- Residual stresses due to thermal mismatch (MPa or GPa)

t- Time of deposition (min)

t_i- Thickness of the i^{th} layer in a laminate

To- Room temperature (25°C)

T_{Ref}- Stress relax temperature during sintering

TD- % of theoretical density

V- Voltage

vol%- Volume %

w- Weight of the deposit (mg or g)

wt%- Weight %

ξ- Zeta-potential (mV)

viii. Table of contents

i. Declaration ii

ii. Abstract iii

iv. Acknowledgements iv

v. List of figures v

vi. List of tables x

vii. List of symbols xii

viii. Table of contents xiv

1. Introduction 1

2. Literature survey 4

2.1 Introduction 4

2.2 Biomimetic materials 4

2.2.1 Bamboo 5

2.2.2 Bone 6

2.2.3 Tree roots 7

2.2.4 Nacre 8

2.3 Electrophoretic deposition (EPD) 9

2.3.1 Considerations 12

2.3.1.1 Liquid media 12

2.3.1.2 Zeta-potential 12

2.3.1.3 Electrodes 14

2.4 Monolithic deposits 15

2.5 Laminate deposits 20
2.6 Poly-crystalline diamond (PCD) 25
2.6.1 Sintering of PCD 25
2.6.1.1 Background 25
2.6.1.2 Considerations 26
2.6.2 Functionally graded PCD 28
3. Materials and method 33
3.1 Introduction 33
3.2 Raw materials 33
3.3 Treatment of powders 35
3.3.1 Acid washing 36
3.3.2 Oxidation 36
3.4 Powder pressed standards 36
3.5 EPD 37
3.5.1 Suspension preparation 37
3.5.2 Deposition 38
3.5.3 Drying 41
3.6 Sintering 42
3.6.1 Pre-sintering preparation 42
3.6.2 Alumina Sintering 43
3.6.3 HPHT diamond Sintering 44
3.7 Preparation of sintered materials for characterization 44
3.7.1 Cutting, grinding, polishing and etching 44
3.8 Characterization 45

3.8.1 FTIR 46
3.8.2 Particle size distribution 46
3.8.3 Zeta-potential 46
3.8.4 Density and porosity 47
3.8.5 Hardness testing 49
3.8.6 Crack propagation 50
3.8.7 Microscopy 51
3.8.7.1 Optical microscopy 51
3.8.7.2 SEM 51
4. Results 53
4.1 Introduction 53
4.2 Alumina EPD results 53
4.2.1 Initial observations 53
4.2.2 Deposition rates 59
4.2.3 Representative samples 60
4.3 Diamond EPD results 63
4.3.1 Suspension optimization 63
4.3.1.1 Surface chemistry 63
4.3.1.2 Organic suspensions 66
4.3.1.3 Aqueous suspensions 68
4.3.1.4 Deposition of monolithic diamond. 69
4.3.1.5 Sintered monolithic diamond deposits 74
4.3.2 Diamond powder pressed standards 78
4.3.2.1 0.5µm powder pressed standard 78

4.3.2.2 2µm powder pressed standard 80
4.3.3 Deposition of laminate diamond. 82
4.3.4 Sintered laminate deposit 84
4.3.5 Defects 90
4.3.6 Fracture of diamond laminate 93
5. Discussion 97
5.1 Introduction 97
5.2 EPD experiments with alumina powder 97
5.2.1 Alumina surface chemistry 97
5.2.2 Alumina deposition 100
5.2.2.1 Experimental considerations 100
5.2.2.2 Deposition rates and green densities 100
5.2.3 Alumina sintering 104
5.3 EPD experiments with diamond powders 105
5.3.1 Diamond surface chemistry 105
5.3.2 Diamond deposition 112
5.3.2.1 Experimental considerations 112
5.3.2.2 Deposition rates and green densities 113
5.3.3 Sintered diamond 116
5.3.3.1 Sintering of monolithic diamond deposits 116
5.3.3.2 Comparison with powder pressed standards 117
5.3.3.3 Sintered diamond laminate 118
5.3.3.4 Defects 120
5.3.3.5 Fracture analysis 121

6. Conclusion and recommendations 126

7. Bibliography 128

1. Introduction

One of the biggest challenges facing structural ceramics these days is the brittleness of the material. The fracture toughness of polycrystalline diamond (PCD), although reasonably high by ceramic standards (Table 1.1) [3-11], is often insufficient when it comes to meeting the increasingly more stringent requirements placed on this class of materials by new, ever more demanding applications [1]. Thus, scientists have looked to nature as inspiration to increase the fracture toughness of their materials. [2]

Table 1.1: Fracture toughness of representative ceramic materials.

Material	K_{1c} (MPa.m$^{1/2}$)	Ref.
Al_2O_3	3-5	[3]
ZrO_2 (TZP)	11.1-17.2	[4]
SiC/ SSiC	3.1-4	[5]
Si_3N_4	5-10	[6]
TiC/Binderless	1-3	[7]
TiB_2	5.2-5.6	[8]
Mullite	2.5	[9]
TiN (5% Binder)	5.3-5.5	[10]
B_4C	3.0	[8]
PCD	13	[11]

In nature, one is able to find many tough materials such as wood, bones and the shell of molluscs. It is the interest of a new field of science called “biomimetics” to try and mimic or derive inspiration from these natural materials. The word biomimetics is constructed from the two words “bio”- meaning life/living organisms and “mimetic” coming from the word mimicry- meaning imitation. Thus biomimetic in the broader

sense refers to imitating nature. One such extremely tough natural material that scientists have looked to for inspiration is nacre found in the shells of abalone molluscs. Despite nacre being very hard due to its high calcium carbonate content, it boasts impressive toughness by means of thin organic interlayers [12].

The purpose of this project was to evaluate electrophoretic deposition as a forming technique to create sintered diamond/diamond layers using two different alternating grades of diamond (Figure 1.1) so as to create a biomimetic structure similar to that found in nacre. Electrophoretic deposition was used as a forming technique to achieve this structure. In nacre, the main reason for toughening is the weak protein interlayers. In this project however, the expected toughening mechanism should arise from residual stresses and fluctuations in cobalt content in the alternating layers after sintering. The resulting laminate sample was analysed for crack deflection as evidence of alternating residual stresses.

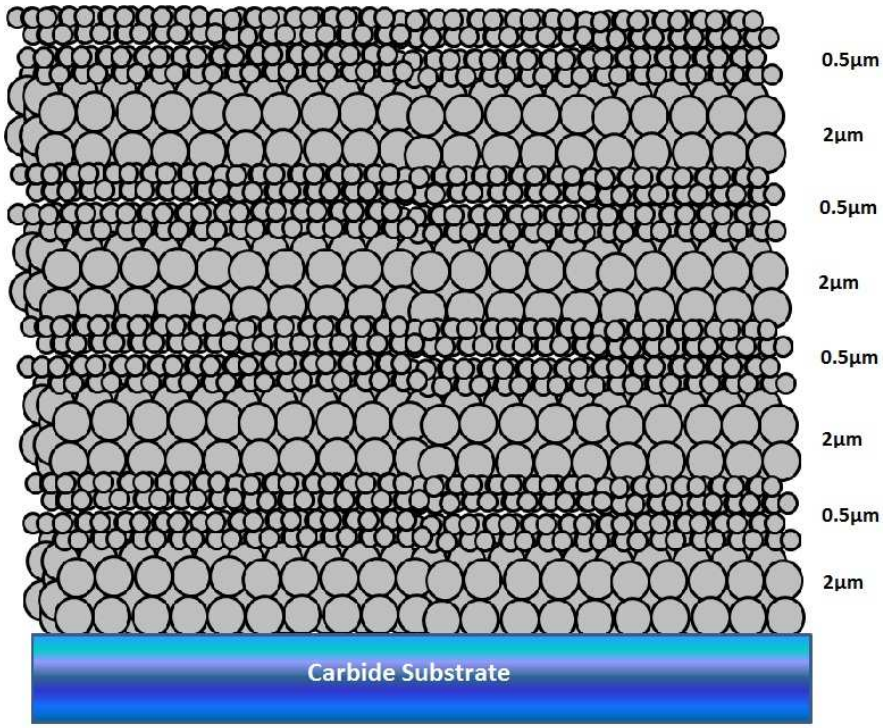


Figure 1.1: Schematic diagram showing the alternating layers of 0.5µm and 2µm grade diamond on a carbide substrate.

As an introduction to electrophoretic deposition, sintered deposits of alumina were prepared to learn and develop the EPD technology prior to the commencement of diamond work.

In Section 2 that follows, a literature survey is presented. Section 3 provides the materials and method used to prepare and analyse the materials. Section 4 presents the results obtained and observations made. Section 5 discusses the results offered in the previous section. Section 6 which concludes this work is followed by a detailed bibliography in Section 7.

2. Literature survey

2.1 Introduction

This literature survey features some examples of biomimetic materials. In addition to this, the technology of electrophoretic deposition (EPD) is introduced as a forming technique and examples of both monolithic and laminate materials manufactured using EPD are shown. Lastly, an introduction to sintering of poly-crystalline diamond (PCD) is offered

2.2 Biomimetic materials

Extremely hard and tough natural materials have been found in nature. These materials have a number of applications. Some of these applications include:

1. Structural [2]: Bamboo and wood which are often used in construction of buildings and furniture,
2. Load bearing and impact protection [13]: Bones, which make up the exoskeleton of vertebrates,
3. Wear [14]: Teeth, which are used to cut, chew and grind food.

Biomimetic materials are materials that have been made to mimic materials found in nature. These materials are made to mimic the shape, structure or composition of a natural material to improve the properties of the synthetic material. In the interest of ceramic science, the survey that follows will focus on toughening mechanisms derived from naturally occurring tough materials. Examples of synthetic biomimetic materials are also provided.

2.2.1 Bamboo

Bamboo is a natural material that shows superior toughness. This property makes it attractive as a building material for homes and furniture. Wang et al. [2] prepared both fibrous monolithic Si_3N_4/BN composites, trying to imitate the structure of bamboos or trees; and laminate Si_3N_4/BN structures, imitating nacre. The materials were made using plastic forming methods such as extrusion and roll compaction.

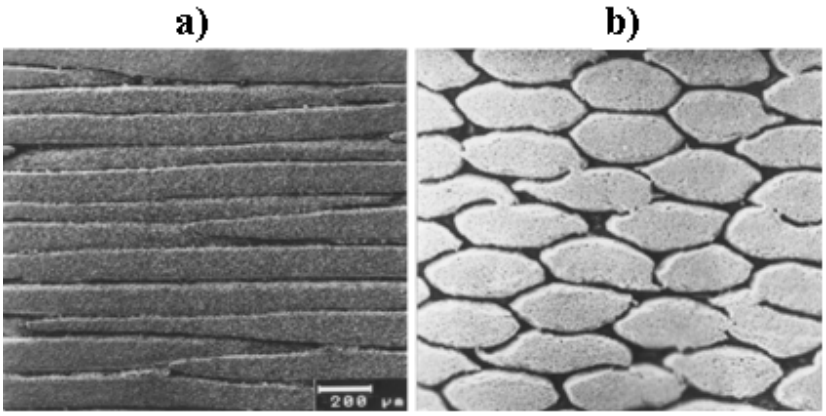


Figure 2.1: a) Longitudinal and b) cross-section microstructure of the fibrous monolithic Si_3N_4/BN resembling the structure of bamboo [2]

The samples were sintered using a hot-press. The fibrous monolithic Si_3N_4/BN had a fracture toughness of 24 MPa.$m^{½}$. The area under the curve (Figure 2.2) calculates the work of fracture for the fibrous monolithic Si_3N_4/BN, which was estimated to be more than 4000 J/m^2, while that of monolithic Si_3N_4 ceramics was only 100 J/m^2. In the experiments, it was found that the load-displacement curves reveal that the material exhibits non-brittle fracture. The high toughness of the samples arised from a combination of multi-level toughening mechanisms such as weak interfaces, whiskers and elongated grains toughening in ceramic matrix cells as revealed in the load-displacement curves (Figure 2.2). It was also found that the diameter of the extruded

fibres (1mm, 0.5mm and 0.3mm) plays an important structure parameter influencing the mechanical behaviour of the composites.

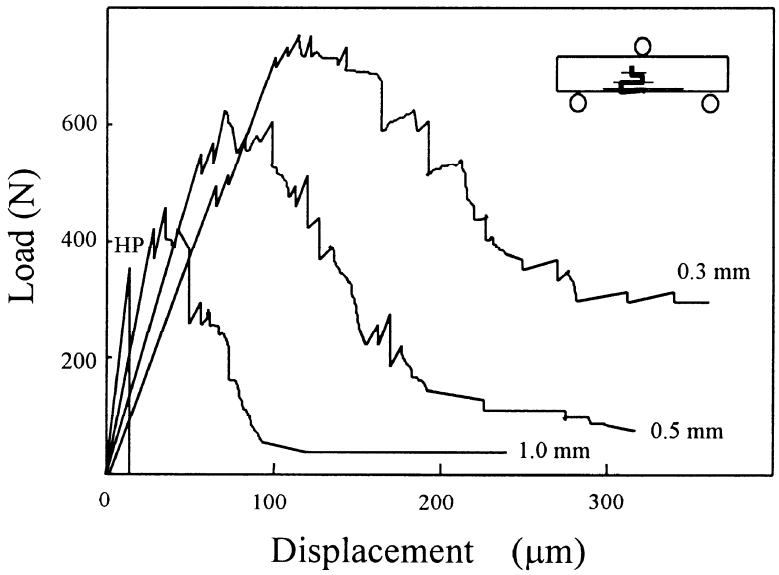


Figure 2.2: Typical load-displacement curve of fibrous monolithic Si3N4/BN showing the plots for extruded fibres of diameter 1mm, 0.5mm and 0.3mm. [2]

2.2.2 Bone

Bones are strong, hard and lightweight mineralized tissue. They make up the endoskeleton of vertebrates. The bones in vertebrate animals come in many shapes and sizes. They serve to support soft tissue for movement and protect vital internal organs such as the heart, lungs and brain from impact [13].

Tian et al. [15] [16] did experiments using material composites which contained SiC whiskers with dumbbell shaped ends at the interfaces. These fibres resemble that of animal bone. It was found that these fibres transferred stress from the matrix to the fibre during compression. The fibre increases the strength of bonding at the fibre-matrix interface.

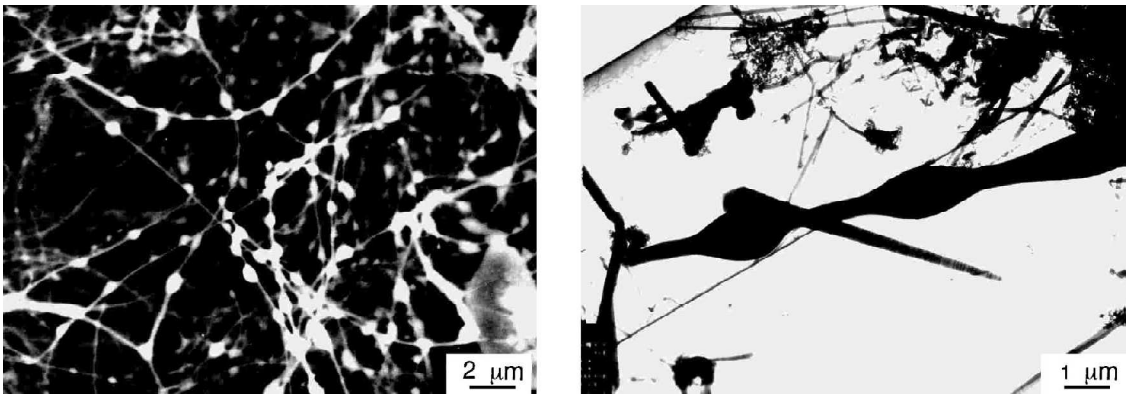


Figure 2.3: Dumbbell-like SiC whiskers resembling bone. [17]

2.2.3 Tree roots

Besides nutrient and water collection, roots help to fix and stabilize trees to the ground. Tree roots also prevent the soil, to which they are rooted, from washing away at river banks and during heavy rains. These properties are desirable for synthetic materials.

Biomimetic materials have been constructed using fibres for reinforcement. Fu et al. [18] [19] used carbon fibres which resemble the roots of trees. The idea behind the design was that the fibres will simulate the strengthening and toughening properties that tree roots impart on soil at riverbanks. In the experimental observation, the force and energy required for the pull-out of synthetic fibres increases with the branching angle.

Fu et al. [18] [19] expect that the fracture toughness and strength of the materials with these branched fibres should be greater than that of the un-branched fibres.

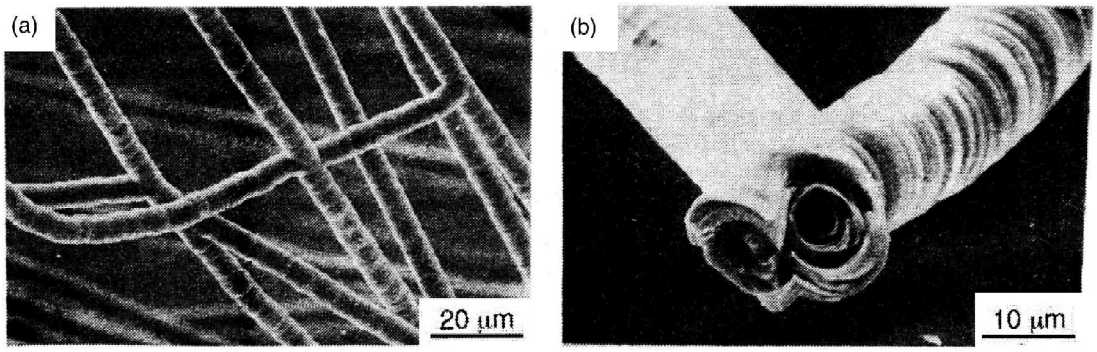


Figure 2.4: a) Microstructure of vapor-grown carbon fibers resembling tree roots b) structure of a branching point [19]

2.2.4 Nacre

One of the key natural materials in the biomimetic field is nacre. This material is found in the inner shell of many mollusc organisms in the sea such as the abalone. The reason for such an interest in this material is due to the fact that nacre boasts an eightfold increase in toughness as compared with its monolithic $CaCO_3$ counterpart [20]. This material boasts fracture toughness values of 8±3 $MPa.m^{1/2}$ in four-point bend tests, and a fracture strength of 185±20 $MPa.m^{1/2}$ in three-point bend tests [21]. This fracture toughness value was higher than the fracture toughness of some technical ceramics (Table 1.1). Its work of fracture when wet is 1240 J/m^2 which is approximately 3000 times higher than that of monolithic calcium carbonate [22].

Some of the key toughening mechanisms of nacre were found to be [12]:

1. Material properties of aragonite and organic matrix, especially the unique properties of the organic phase in the confined space between platelets.
2. Structure at micro scale: size, shape of platelets etc.
3. Interlocking of aragonite platelets: progressive failure of interlocks guides the fracture path.

4. Molecular interactions at the organic–inorganic interface.

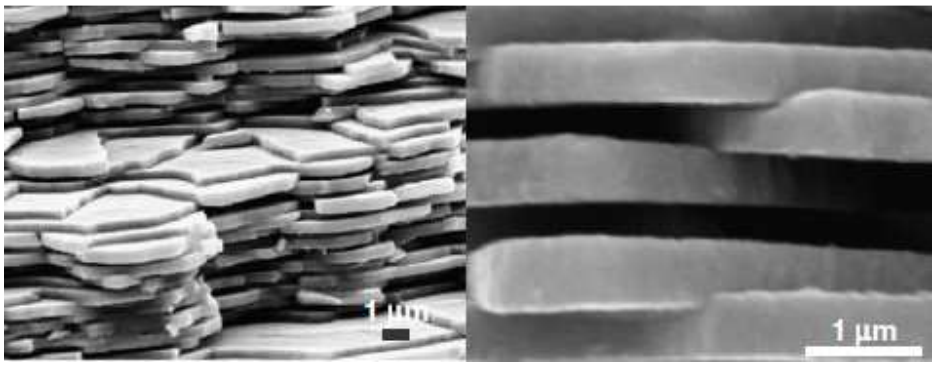


Figure 2.5: An SEM image of the micro-structure of nacre [12].

Due to nacre's impressive toughness figures, it is the primary inspiration for the biomimetic diamond material made in this project. In nacre, the main reason for toughening is the weak protein interlayers. Weak interlayers increase the fracture toughness of the material by crack deflection, delamination and crack blunting [23]. In this project however, the expected toughening mechanism should arise from residual stresses and fluctuations in cobalt content in the alternating layers after sintering.

2.3 Electrophoretic deposition (EPD)

Electrophoretic deposition (EPD) is a relatively old concept that has been applied to the modern field of material science. EPD was first discovered in 1803 when Russian scientist Reuss noticed the movement of suspended clay particles under the influence of an electric field [24]. It was only by 1933 that EPD received practical consideration when it was used to deposit thoria particles onto platinum electrodes as an emitter for electron tube applications [24]. Nowadays, the technique of EPD receives a lot more attention in the ceramics field as a shaping tool. Some of the reasons for this is that EPD is versatile thus it can be used for depositing a number of different powders in

various suspension media, it allows deposits and coatings of complex shapes which may otherwise be difficult to achieve using traditional shaping techniques, it allows for deposits of controllable thickness through adjustment of the EPD parameters. The equipment required for EPD is simple and, as a result, the process is relatively cost effective..

Electrophoretic deposition, as the name may suggest, is a two-step process. The first part of the process is electrophoresis, which is the movement of charged particles in an electric field. The second step is deposition, which is the collection of particles on the electrode [25].

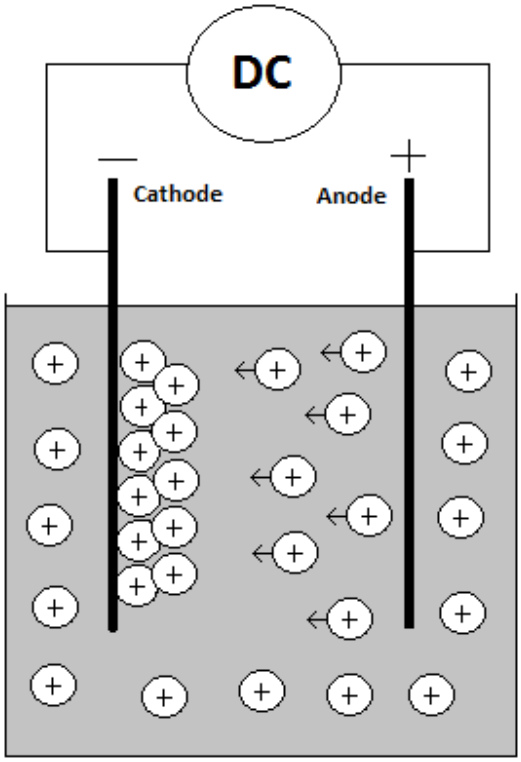


Figure 2.6: Typical EPD setup.

The setup of an EPD experiment is relatively simple (Figure 2.6). It generally involves a container holding a suspension of the material to be deposited and two electrically conductive electrodes that are connected to a DC power supply and submerged in the suspension. When the power supply is switched on, the positively charged particles in Figure 2.6 would move towards to the negative electrode. However, as simple as the design of an EPD cell is, there are many important factors to consider.

2.3.1 Considerations

2.3.1.1 Liquid media

The liquid media for suspending the particles should be considered carefully. Although using an aqueous media is attractive because it has the advantages of a high dielectric constant and its industrial processes being environmentally friendly [26], serious problems do exist. At relatively low voltages (~5V) [27], water will electrolyse into hydrogen and oxygen gas. The developing gas bubbles interfere with the deposit at the electrode and cause an increased porosity in the green body. Therefore most researchers conducting EPD experiments opt for short chain alcohols such as methanol, ethanol and isopropanol which will not electrolyse even at higher voltages. Alcohols, due to their lower dielectric constants, require higher voltages to achieve the same deposition rates at their aqueous counterparts [28].

2.3.1.2 Zeta-potential

The surface of charged particles in suspension will cause ions and polar molecules to experience Coulombic forces. These forces will cause like charged ions and polar molecules to repel and oppositely charged ones to be attracted, thus resulting in an increase in their concentration at the surface of the particle relative to that of the bulk. Therefore, due to the law of charge conservation, a potential difference between the surface of the particle and the bulk solution develops. As a result, the particles will have a relatively immobile adsorbed layer, as well as a less rigidly attached diffuse layer of ions and polar molecules surrounding the particles. This is known as the electrical double-layer [29].

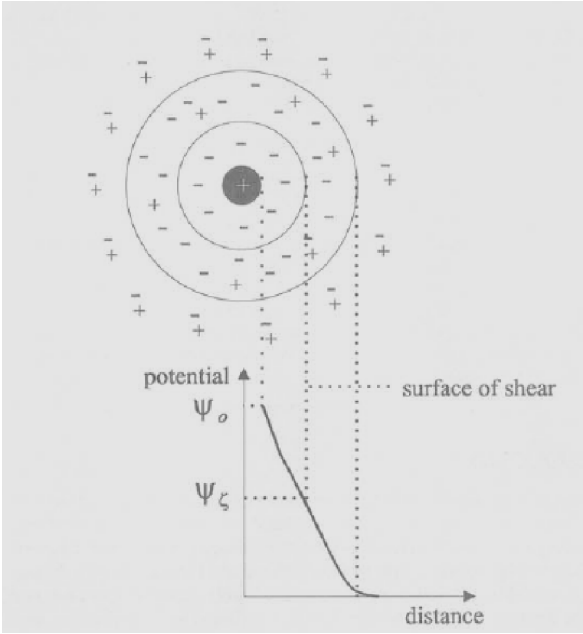


Figure 2.7: Diagram of the double layer surrounding a charged particle. The potential at the surface of shear is termed the zeta potential. It is the main parameter determining electro-kinetic behaviour [27].

Charged particles in suspension will experience movement when an electric field is applied. The velocity of these particles is called the electrophoretic velocity. In much the same way, the ionic solution adjacent to the wall of a capillary with an electrical double layer will flow once an electric field is applied. This is called electro-osmotic flow. During this flow, a hydrodynamic slippage plane forms somewhere in the double layer. The potential at this slippage plane is called the zeta-potential [29].

For optimal deposition rate and highest suspension stability, the absolute zeta-potential on the particles should be at a maximum. This can be achieved either by adjusting the pH of the solution or by the use of ionic additives. In most cases, these additives are either adsorbed or react on the surface of the particle to increase its charge. This extra charge will result in a more stable suspension due to the enhanced electrostatic repulsion between the particles, as well as better movement in the applied electric field. While adding ionic additives to the suspension may enhance the zeta-potential, it

is important to note that the conductivity resulting from dissolved species should be kept at a minimum so that most of the current generated in the system results from movement of the charged particles to be deposited.

2.3.1.3 Electrodes

The material from which the electrode material is to be chosen should have a high conductivity and should not react during the EPD process [28]. Typical electrodes used are nickel, graphite, platinum and stainless steel. The deposit should also be easily removed from the electrode for materials requiring stand-alone sintering, or should have adequate adhesion for materials where deposit and substrate are sintered together. Electrodes should be kept at a constant separation and their geometry parallel during deposition.

2.4 Monolithic deposits

A multitude of papers (Table 2.1) reporting monolithic (non-layered) EPD experiments have been published. Due to their relative simplicity, monolithic EPD experiments provide valuable data before tackling the much trickier laminate deposition.

Table 2.1: Summary of monolithic deposits obtained by EPD.

Reference	Deposited Material	Voltage V/cm	Colloidal suspension Formulation		Deposition Rate g/(cm^2.min)	Green Density % TD
			Media	Additives		
Besra et al. [30]	Al_2O_3	166	Butan-1-ol		0.0012	
Van der Biest [31]	Al_2O_3	16.5	Ethanol	HCl (pH<5)	~0.1	53
De Riccardis et al. [32]	Al_2O_3 and Al_2O_3/Zr	15-20V	Ethyl Alcohol	Citric acid/ TEA		
Clasen [33]	Fumed Silica	3	Water	TMAH, acetic acid, salt acid	0.5 (~1mm/min)	>80
Valdes et al. [34]	Diamond	5-40	Water	HCl (pH<5.6)		
Affoune et al. [35]	Diamond	6.67	Isopropanol	Iodine, Water, Acetone		
Zhitomirsky [36]	Diamond	~33.3-200	Isopropanol	Iodine, Water, Acetone	~0.024	

Besra et al. [30] performed the electrophoretic deposition of alumina particles onto stainless steel electrodes in a butan-1-ol media. A derivation of the Hamaker equation (Equation 2.4-1) ,which allows the calculation of deposit weight (*w*) by comparing the EPD process to sedimentation, was reported.

$$w = \frac{2}{3} C \varepsilon_0 \varepsilon_\tau \xi \left(\frac{1}{-}\right) \left(\frac{E}{l}\right) t \qquad \textbf{Equation 2.4-1}$$

In Equation 2.4-1, C is the suspension concentration, ε_0 is the permittivity of a vacuum, ε_τ is the relative permittivity of the solvent. ξ is the zeta-potential, η is the viscosity of the liquid meda, E is the electric field strength, l is the separation of the electrodes and t the time of deposition. A change in the rate of deposition is thus brought about by manipulation of the variables in Equation 2.4-1.

Therefore, for a particular liquid medium, powder and experimental setup (i.e. electrode separation), the weight of the deposit is proportional to the concentration of the suspension, electric field applied across the electrodes and deposition time (Equation 2.4-2).

$$\boldsymbol{w = (k)ECt} \qquad \textbf{Equation 2.4-2}$$

This simplification of the equation is possible when a particular solvent, powder and experimental setup is used and thus k becomes the embodiment of the constants. From this equation it is evident that controlling the weight of the deposit is a function of three variables, namely electric field strength, concentration of the suspension and time of deposition.

Besra et. al. [30] also report the surface morphology of the deposited film made from a higher suspension concentration was not as smooth as compared to those obtained from the lower suspension concentrations. They suggest that this may possibly be due to the high deposition rates at higher concentrations. At such rates, the particles do not have enough time to sit at the closest possible packing positions before deposition of

incoming particles. No mention is made of the effect of suspension concentration on green density.

In an effort to make EPD processes more environmentally friendly, aqueous suspensions have become the more attractive alternative to organic media. However, higher voltages (>5V) will cause the electrolysis of water, and thus cause gas bubbles forming on the electrodes which will lead to a higher porosity on the deposit [30]. This problem has been solved by Clasen [33] by placing a cellulose membrane at some distance in front of the electrode thus keeping a distance between the deposit and the bubbles developing at the electrodes (Figure 2.8). Since water has such a high dielectric constant, Clasen [33] managed to achieve a deposition rate as high as 0.5g/(cm^2.min) from an aqueous suspension of nano-sized fumed silica.

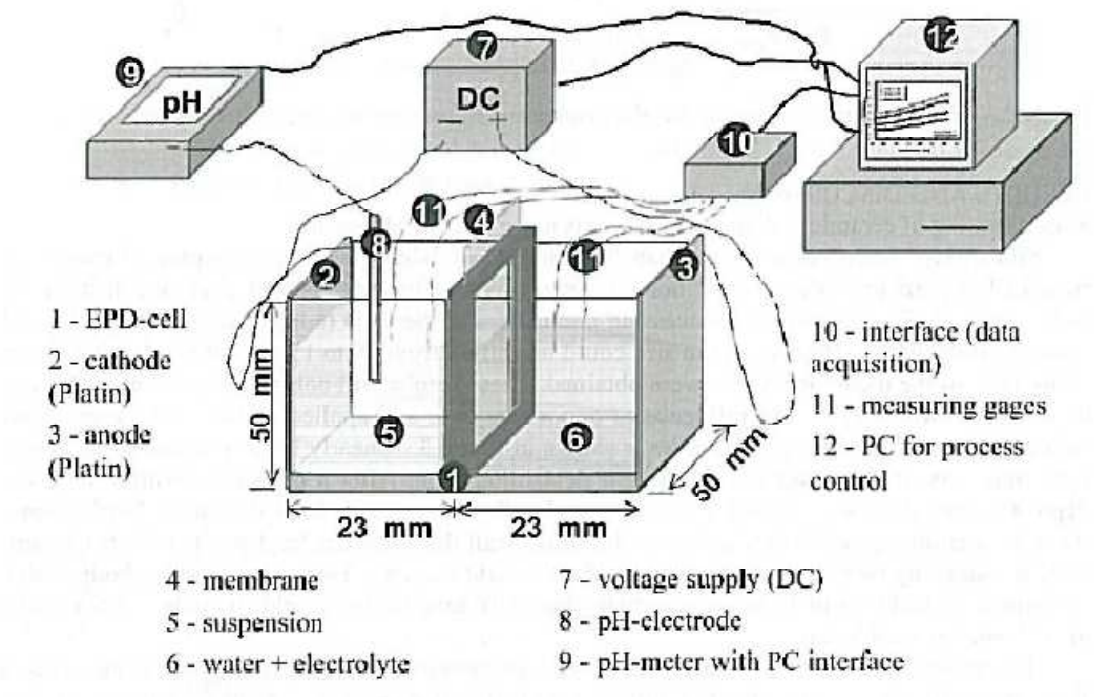


Figure 2.8: Diagram of the typical EPD setup for aqueous deposition with a membrane between the two electrodes [33].

Another solution to the gas formation problem was discovered by Neirinck et al. [37] An unbalanced alternating current was used instead of the traditional DC current that is used in most setups. Neirinck et al. [37] suggest that the electrochemical decomposition of water is a sluggish process and that frequencies of 50 Hz are sufficient to stop the reaction from happening. The deposits made using this were free of pores caused by bubble formation (Figure 2.9). It was also found that the deposits made in this way had a green density which is intrinsically higher than those formed by traditional DC EPD from ethanol based suspensions.

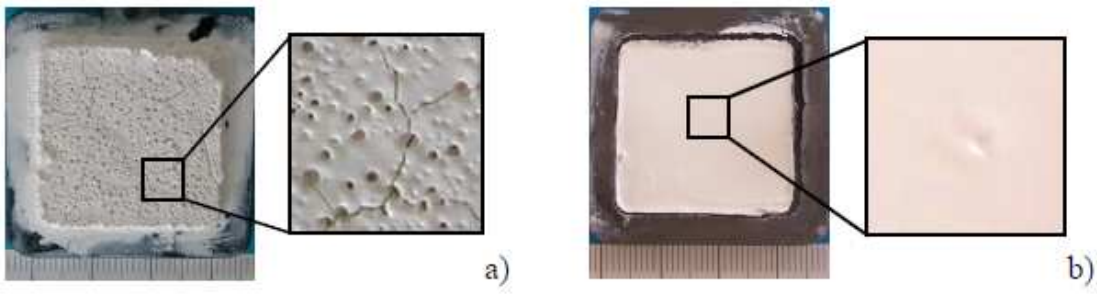


Figure 2.9: Alpha-Al_2O_3 deposits formed using (a) 100 V DC for 1200 s and (b) a 50 Hz asymmetric AC field with an amplitude of 500 V_{p-p} [37].

Very little literature exists on the EPD of diamond particles. An important contribution of work on the deposition of diamond has been done by Affoune et al. [35] and Zhitomirsky [36]. Both used isopropanol suspensions of the diamond with iodine, water and acetone (25-50mg, 1-2mL and 2-3mL respectively for a 100mL isopropanol suspension) as additives to improve the zeta-potential of the diamond via an in situ reaction that produces hydrogen ions by the following equations:

$$CH_3COCH_3 \rightleftharpoons CH_3C(OH)CH_2 \qquad \textbf{Equation 2.4-3}$$

$$CH_3C(OH)CH_2 + I_2 \rightarrow CH_3C(OH)CH_2I + H^+ + I^- \qquad \textbf{Equation 2.4-4}$$

It is hypothesized that diamond particles acquire a negative charge in water and organic solvents. The protons generated by the reaction of water, iodine and acetone are adsorbed onto the surface on the diamond and thus give the diamond particles a positive zeta-potential which causes them to deposit onto the cathode during EPD [36].

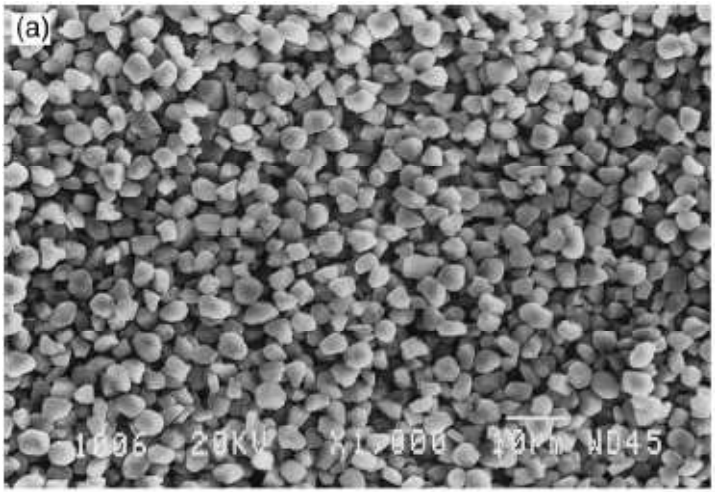


Figure 2.10: SEM picture of the diamond deposit obtained using an isopropanol suspension with acetone, iodine and water as additives [36].

Zhitomirsky's [36] deposit made from 3-6µm size diamond is shown in Figure 2.10. Deposition rates of approximately 0.024g/cm^2.min were achievable and various thicknesses (up to 100mm) were claimed.

2.5 Laminate deposits

It is known that layered materials are generally tougher than their monolithic counterparts. In laminates, the increase in toughness usually arises from the incorporation of weak interlayers [38] or a stressed interface [39]. Laminate EPD experiments in literature (Table 2.2) generally involve using two suspensions, each with a different ceramic powder. Thus multi-layered deposits are made by moving the electrodes from one suspension to another once a layer achieves the desired thickness.

Amongst first researchers to perform ceramic/ceramic laminates were Sarkar and Nicholson [40]. In this work, alternating layers of yttria-stabilized zirconia and

alumina (Figure 2.11) were made. Sarkar and Nicholson [40] succeeded in making 80 layers of average thickness of 20 μm for the alumina layers and 2 μm for the zirconia layers. The final composite was greater than 2mm thick. In the EPD experiments a 10 wt% suspensions of the respective powders in an ethanol medium was used. In the experiment it was found that the boundaries between the layers were straight and well defined. A deposition rate of ~135μm/min at 125V/cm was achieved, thus showing that EPD was a reliable and relatively fast process of creating laminate layers.

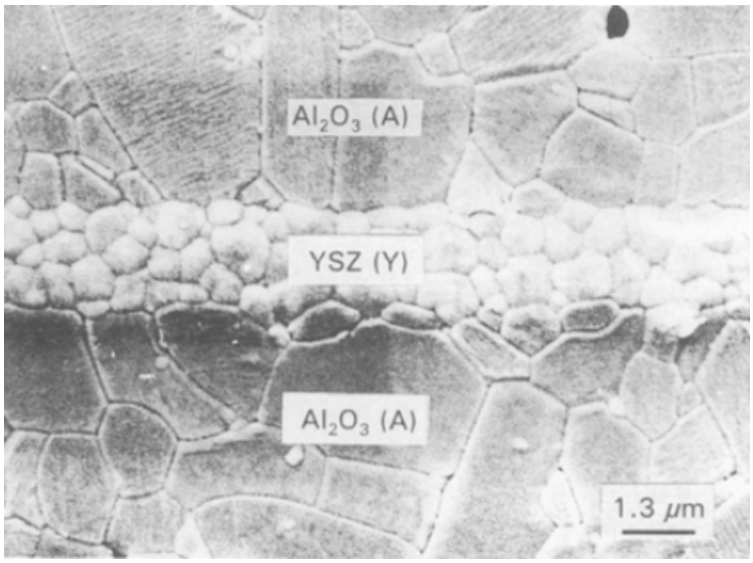


Figure 2.11: Boundaries between the sintered alumina/zirconia laminates by Sarkar and Nicholson [40].

SiC/TiC layers (Figure 2.12) were produced by You et al. [41]. This was achieved by suspensions of a concentration for 50g/L of the respective powders in an acetone medium. An ultrasonic bath was used for 15min prior to deposition in order to break up any agglomerates. The deposition cell was constructed using a glass beaker, a working electrode made of carbon paper and a counter electrode made of stainless

steel. Each layer was formed by one minute deposition which was repeated up to 20 times. A deposition rate of ~0.075g/cm^2.min was achieved.

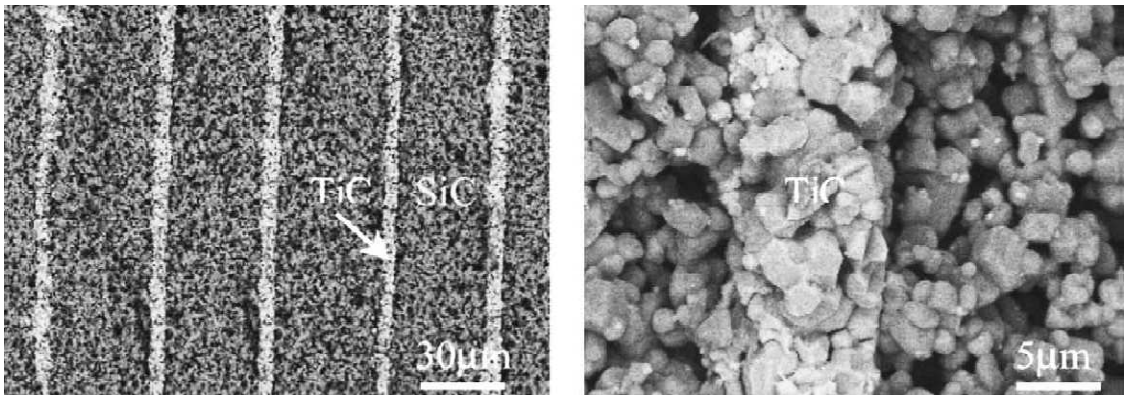


Figure 2.12: SEM image showing the pressureless sintered SiC/TiC laminates achieved by You et al. [41]

Van Der Biest et al. [31] managed to produce silicon carbide/graphite laminates in a cylindrical shape by using a hollow cylindrical graphite deposition electrode with a rod placed in the centre of the cavity as a counter electrode. It was found that the deposit shrank during drying and thus allowed for easy release of the deposit from the electrode. The process of adding sequential layers was automated by attaching the electrode set-up to an existing apparatus used for multi-layered electro deposition. Thus with this apparatus, it was possible to place the electrode in 4 different bath solutions, automatically adjust the voltage, and the time spent in each. Van Der Biest et al. [31] found that the laminate did indeed exhibit crack deflection along the weaker layers of graphite.

A potential drop is expected as the deposit thickness increases. This is due to the insulating effect of the deposit on the electrode which causes a higher specific resistance than the volume of suspension it releases. The potential drop has a negative impact on the deposition rate due to the lower driving force of the particles. Van Der

Biest et al. [31] also used suspensions with different media and additives to see the effect of potential drop over time. It was found that ethanol and nitric acid had the largest potential drop which is more suitable for thin homogenous coatings.

Ferrari et al. [42] and Fischer et al. [26] produced alumina/zirconia laminates in aqueous media. Aqueous suspensions are attractive in that water has a high dielectric constant and aqueous processes are more desirable in a world becoming more “green” conscious.

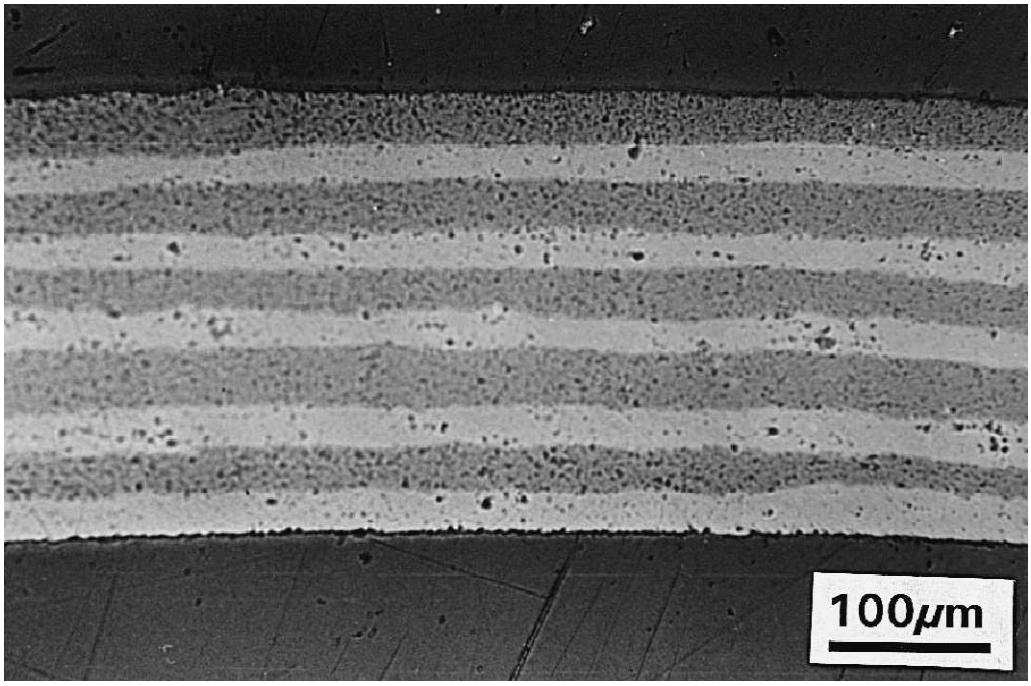


Figure 2.13: Alumina/zirconia laminates prepared by EPD using a suspension of each of the materials with 0.6% deflocculant [42]

Table 2.2: Summary of laminate deposits obtained by EPD in literature.

Reference	Deposited Material	Voltage V/cm	Colloidal suspension Formulation		Deposition Rate	Green Density % TD	Final material characteristics		
			Media	Additives			Geometry	Laminate Thickness	Layer Thickness (µm)
Sarkar et al. [40]	Al_2O_3/Y-TZP	75-125	Ethanol	HCl (pH<5)	~110µm/min-135µm/min	~60%	Planar	1.5mm (80 layers)	1-2
Fisher et al. [26]	Al_2O_3/Y-TZP	~2-5	Water	Dolapix CA, Ammonia (pH>11)	0.012g/cm^2.min	High porosity	Planar	0.193mm (5 layers)	8-20
Ferrari et al. [42]	Al_2O_3/Y-TZP	7-30	Water	Dolapix CE64	~0.006g/cm^2.min		Planar	10 layers	25-50
Zhitomirsky et al. [43]	Al_2O_3/Ce-TZP	~33.3	Isopropanol		~14µm/min		Raidal	20 layers	1-10
Vandeperre et al. [44]	SiC/C	145V	n-Butylamine, Acetone, Isopropanol	HCl (pH<6)	~150µm/min		Radial	57µm (21 layers)	10-100
You et al. [41]	SiC/TiC	~8	Acetone		~0.075g/cm^2.min	SiC: ~60.1%, TiC:~59.6 %	Planar	20 layers	~5-30

2.6 Poly-crystalline diamond (PCD)

2.6.1 Sintering of PCD

2.6.1.1 Background

Due to the unique properties of diamond, it has been used in a variety of applications such as cutting, drilling, milling and abrasives. Initially, diamond was sintered by Katzman and Libby [45] using diamond powder and 20% cobalt as binder at a high pressure of 6.2GPa and a high temperature of 1590ºC. It was found that these conditions were above the diamond-cobalt eutectic. When diamond particles were sintered with a metallic solvent, the metal promoted inter-crystalline bonding between the diamond grains.

Wentorf and Rocco [46] described the manufacture of a layer of diamond onto a cemented layer of tungsten carbide (WC). This was achieved by having a 0.5-1mm diamond powder layer on top of a 10mm WC-10%Co layer. During pressures greater than 5GPa and temperatures of 1400-1600ºC, the cobalt from the WC layer would become liquid and the diamond would be sintered in a liquid phase fashion.

Nowadays, diamond is sintered on top of pre-sintered tungsten carbide-cobalt (WC-Co) substrates by the method described by Veraschagin et al. [47]. With this method of sintering one could achieve a better packing density of the diamond. Cobalt binder would also end up in the voids rather than between the grains. This meant that there were diamond to diamond bonds.

In the SEM image in Figure 2.14, the PCD (black) was sintered on top of a WC substrate (white) by the infiltration of cobalt (grey) from the WC layer into the diamond table.

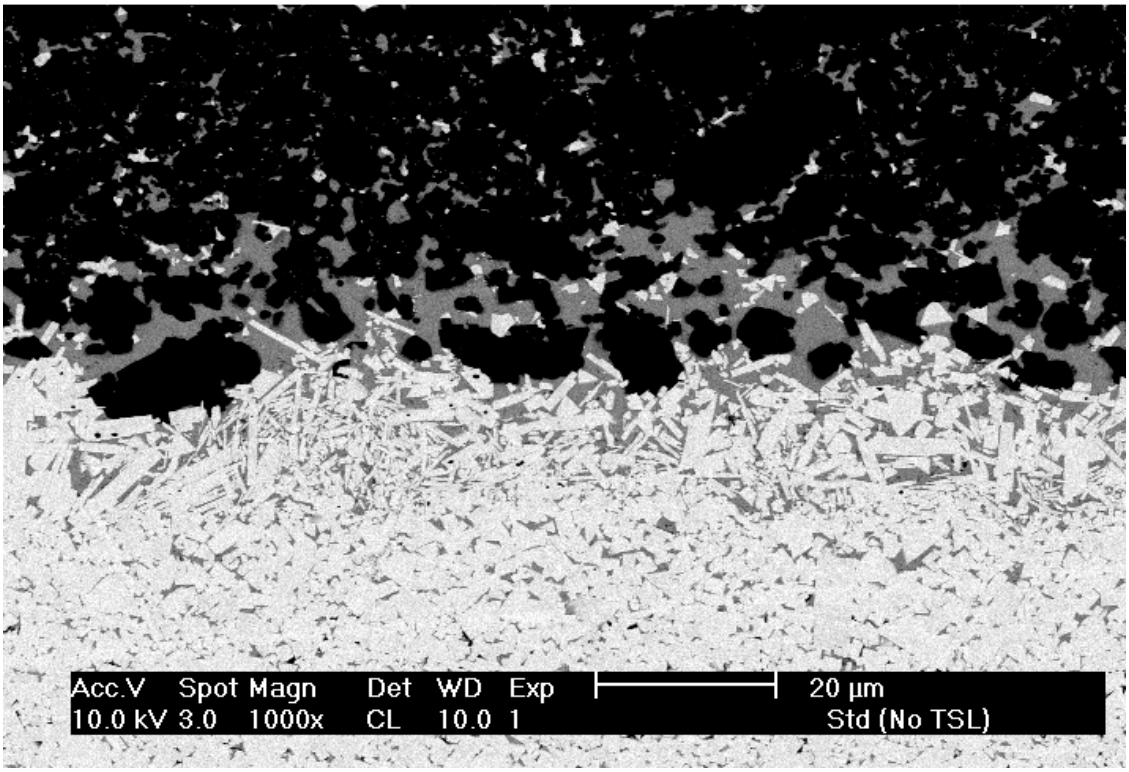


Figure 2.14: SEM micrograph of a typical PCD sintered at 8.5GPa and 1400ºC [48].

2.6.1.2 Considerations

At the cooling stage of the sintering cycle, residual stresses develop at the WC-diamond interface. This is due to differences in thermal expansion coefficients [49]. In some cases this may lead to delamination of the diamond table from the substrate. Similarly, fractures can occur in the diamond table due to differences in thermal expansion coefficients between the cobalt binder and the diamond skeleton [50].

Another important factor to consider during the sintering of fine-grained PCD is abnormal grain growth (AGG). Using submicron diamond powder (<1µm), it was observed that some grains will grow to sizes of over 100µm. The AGG region is considered a weak spot in cutter tool and fracture and delamination from the WC-Co substrate may occur at this site [51].

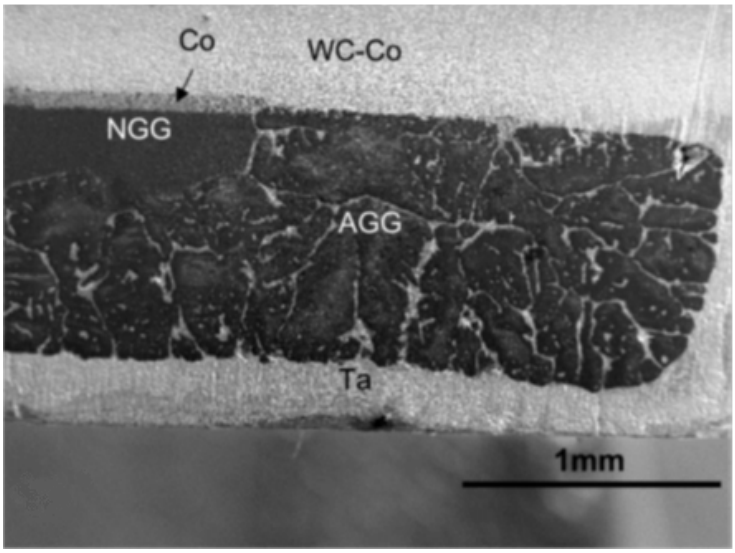


Figure 2.15: SEM of the micro-structure of the cross section of a PCD sintered compact made using 2µm diamond powder exhibiting AGG. [51].

In Figure 2.15, the huge grains are visible in the AGG area. The normal grain growth is visible in the NGG area. Grain growth occurs due to Ostwald ripening by a mechanism of solution-reprecipitation. During sintering, the small diamond grains dissolve into the molten cobalt metal and reprecipitate onto the larger diamond grains, thus causing them to grow. Because the smaller particles have a higher interfacial energy than the larger particles, they will more readily dissolve in the cobalt to lower the total energy of the system. This is the criterion for Ostwald ripening. Various techniques have been

used to supress the grain growth problem. Such technique include: addition small amounts of cubic boron nitride [52] and using Ni-Zr alloys as sintering aids [53].

2.6.2 Functionally graded PCD

It is known that the wear resistance of polycrystalline diamond (PCD) is inversely proportional to the particle size of the diamond powder which is to be sintered [54]. Thus the smaller the particle size of the starting diamond powder, the more wear resistant the tool is going be.

Fracture toughness on the other hand increases with increasing particle size of the starting powder [54]. The amount of catalysing metal binder within the composite is also found to have a link to the fracture toughness. In general, small amounts of the metal (i.e. cobalt) tend to increase the fracture toughness of the tool.

Therefore, fracture toughness and wear resistance work antagonistically. It is of industrial importance to try and increase the wear resistance of the PCD without negatively impacting on its fracture resistance. One of several techniques trying to solve this issue is the use of multimodal diamond layers which consist of variations in particle size across the composite. This kind of material is called functionally graded. Other techniques include trying to change the content of the catalysing metal within the diamond table in a functionally graded manner [55].

Matthias [55] described a method for forming functionally graded green bodies. The first step of the invention involves providing a mixture of diamond particles of different particle size. The second step requires the agitation (for example by vibration) of these particles such that they begin to segregate based on particle size by the “Brazil nut effect” as in Figure 2.16. This is then followed by immobilization of the particles with a fixing agent and then sintering.

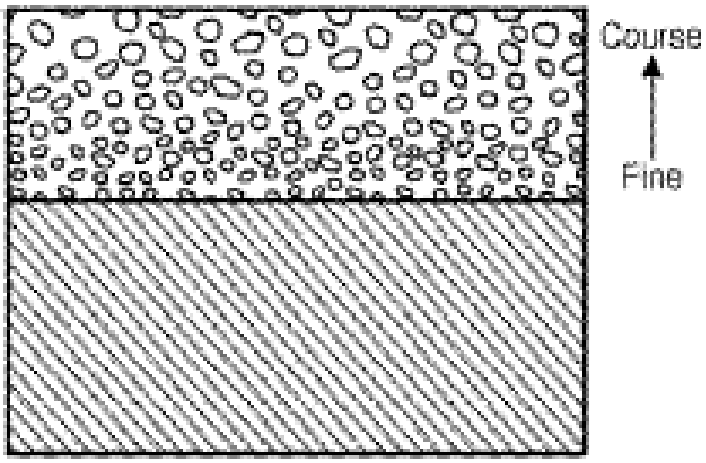


Figure 2.16: Schematic of a functionally graded material achievable by particle agitation [55].

Another method described by Matthias [55] was having adjacent layers of differently sized particles which were then agitated to promote separation within the layers as is shown in Figure 2.17. It was hypothesized that a diamond cutter made with this structure is more fracture resistant.

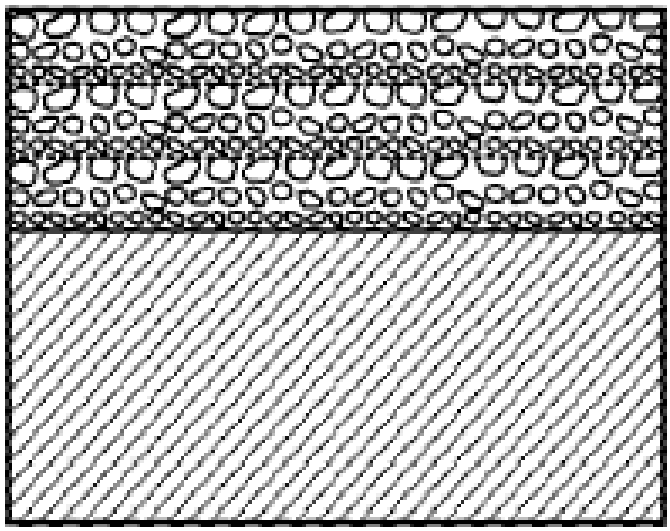


Figure 2.17: Another schematic of a functionally graded material achievable by the agitation of multimodal powders [55].

While keeping the information presented above in mind, it is in the interest of this project to produce a sintered functionally graded diamond having alternating discrete layers of two different particle sizes. Diamond particles of mean particle size 0.5µm and 2µm respectively, will be deposited in a layer structure as shown in Figure 1.1Figure 2.1 using EPD.

It is hypothesized that during the cold compaction stage of diamond sintering, coarser grade diamond experiences more plastic deformation . This allows for re-arrangement of the particles and leads to a lower porosity. Since the pores in the compact will be infiltrated by liquid cobalt during the heating stage of sintering, the coarser grade diamond due to its lower porosity will result in a lower residual cobalt concentration. Therefore, the finer grade layers will contain more cobalt than the coarser grade layers.

Table 2.3: Comparison of linear thermal expansion coefficients for diamond and cobalt at room temperature.

Material	Linear thermal expansion co-efficient. α (10^{-6} m/m K)	Ref.
Diamond	1.0	[56]
Cobalt	13.0	[57]

Because cobalt has a higher thermal expansion co-efficient than diamond (Table 2.3), it should contract faster during cooling. However, due to the constraint of the diamond skeleton on the cobalt, residual stresses arise. In a multi-layer material where alternating layers have different cobalt content, it is expected that the extent of these stresses will vary.

The cobalt rich diamond layers should experience more tensile forces than the cobalt deficient layers. Thus, a crack propagating through the material is expected to deflect when moving from a cobalt rich layer (finer grade) and a cobalt poor layer (coarse grade) as in Figure 2.18.

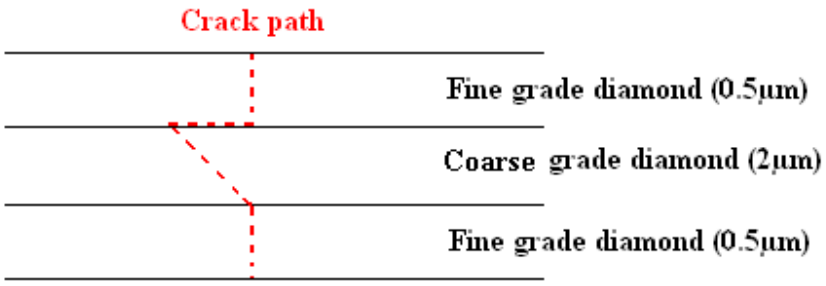


Figure 2.18: Illustration of the expected crack path through the sintered layered material.

This crack deflection caused by the residual stress should result in a longer fracture path and as a result, the layered diamond is expected to have higher fracture toughness. This, in theory, would improve the properties of the PCD material.

3. Materials and method

3.1 Introduction

This section describes the experimental procedures as well as equipment used for preparing, testing and characterizing samples. Each section herein is sub-divided and describes work done on both alumina and diamond materials.

3.2 Raw materials

AKP-50 Alpha Alumina powder was obtained from Sumito Chemical Co. Ltd. Average particle size for the alumina was 0.1-0.3µm. A particle size distribution graph of the alumina powder is shown in Figure 3.1.

Diamond powders of average particle size distribution 0.5µm and 2µm were obtained from Element Six (Pty) Ltd. A particle size distribution graph of the diamond powders is shown in Figure 3.2.

Table 3.1: Ceramic powders used.

Material	Grade	Average particle size	Supplier	d_{10}	d_{50}	d_{90}
Alumina powder		0.1-0.3µm	Sumitomo Chemical Co.	0.147	0.226	0.337
0.5 Micron diamond powder	0.5	0.5µm	Element Six	0.314	0.432	0.603
Grade 2 diamond powder	2	2µm	Element Six	1.01	1.66	2.67

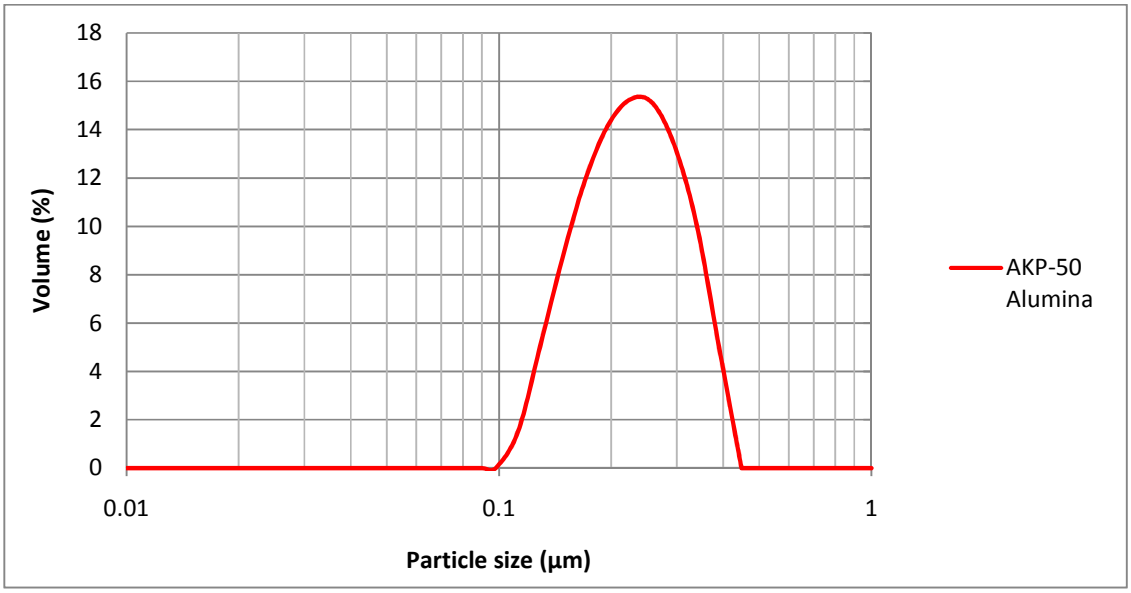


Figure 3.1: Particle size distribution of AKP-50 alumina.

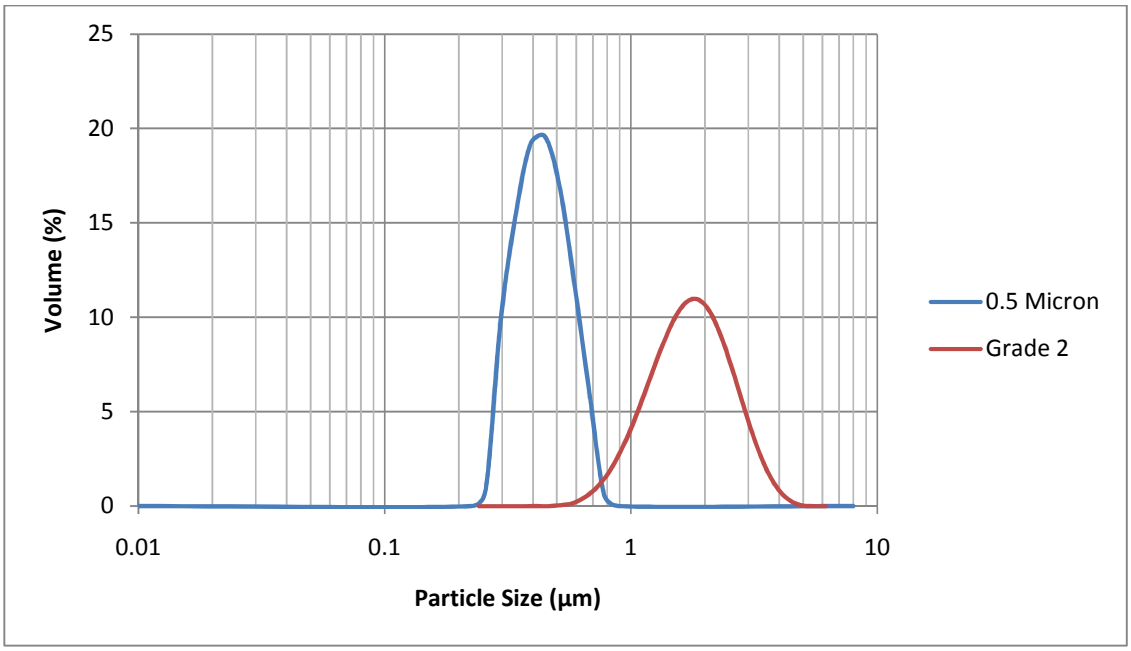


Figure 3.2: Particle size distribution of diamond powders used.

Deposition substrates (electrodes) used for alumina were 316 grade stainless steel plates wrapped with aluminium foil. The dimensions of the plates were 25mm x 100mm x 0.1mm. These plates were masked to reveal a deposition area of $2cm^2$.

Deposition substrates for diamond were tungsten carbide with 13 vol. % cobalt (WC-Co 13%). WC-Co 13% with 10 vol. % graphite-diamond enhanced tungsten carbide (DEC substrate) was also used for diamond deposition. These were obtained from and cut at Element Six into discs 2mm thick with a diameter of 18mm. The deposition surface of these discs were ground and polished to a 1µm finish.

Table 3.2: Deposition substrates used.

Substrate	Additives	Source
316 grade stainless steel	Aluminium foil cover	WITS university workshop
WC discs	13% (v/v) Cobalt	Element Six
WC discs	13% (v/v) Cobalt with 10% graphite	Element Six

Tungsten carbide electrodes were used for diamond deposition as they will also serve as the diamond substrates during sintering. This allows for the convenient elimination of the transfer from EPD substrate to sintering substrate.

3.3 Treatment of powders

In order to achieve stable suspensions and successful deposition, treatment of powders is necessary. The various treatments are presented in this section.

3.3.1 Acid washing

During the manufacturing process of diamond, metallic impurities such as nickel and copper are introduced in the powders. These metal impurities can be removed by washing of the powder with acid. The as received diamond powder to be used for EPD was washed by mixing 10g of diamond powder with 100ml of 32% HCl. The mixture was stirred and boiled on a hot plate for 10 minutes. The mixture was left to cool and the supernatant was decanted off. The acidic slurry of powder was then rinsed five times consecutively with water to remove the remaining acid and dissolved trace metals. The last rinse was conducted with distilled water to ensure removal of ionic species. After the final wash, the supernatant again was discarded and 50ml of acetone was added to the diamond slurry to facilitate drying of the powder. The slurry was placed in a drying oven over-night.

Since alumina was used only for training purposes, washing was not performed on this powder.

3.3.2 Oxidation

Oxidation of diamond is known to occur in air at temperatures above 450ºC and is known to introduce oxygen containing species onto the surface thus making the diamond more polar. The diamond powder was oxidized at 500ºC for 20 minutes using a ramp rate of 5ºC/min.

3.4 Powder pressed standards

0.5µm and 2µm standards were prepared by the traditional powder pressing technology by placing 2g of the as received powder was placed into alumina coated niobium cups. A DEC substrate was placed on top of this powder. The powder was then compacted using a hand press. These samples were then prepared and sintered under the same conditions as the EPD samples.

3.5 EPD

A detailed experimental procedure for conducting EPD is described in this section.

3.5.1 Suspension preparation

Alumina suspensions were prepared by stirring 10 of alumina powder into 100mL of isopropanol. The concentration of the suspension was calculated in a mass per volume fashion. Thus, for example, 10g of alumina powder added to 100ml suspension media will give a concentration of 10% (w/v). The suspension was then ultrasonically treated using a Bandelin Sonoplus HD 2200 ultrasonic probe which has a maximum power output of 200W. The treatment lasted for a time of 2 minutes with a power output of 20% of the maximum (40W). Polyethylene glycol (PEG-400) was added to the suspension (0-0.4wt %). The pH of the suspension was then adjusted either with HCl (acidic) or NaOH (basic) solutions until the desired pH was achieved. pH measurements were performed using a Eutech pH 510 pH meter (calibrated before each use using a three point calibration technique using standard solutions of pH 4.00, 7.00 and 10.00 respectively).

Diamond suspensions were prepared by stirring 3 or 5g for the 0.5µm powder ,and 7 or 10g of 2µm diamond powder into 100mL of the respective media. For alcoholic suspension, the diamond powder was mixed in isopropanol (i-PrOH). For aqueous suspensions the diamond was dispersed in distilled water (dH_2O). Diamond suspensions were subjected to the same ultra-sonic treatment as the alumina suspensions. The pH of the diamond suspension was also adjusted either with HCl or NaOH solutions until the desired pH was achieved. No PEG was used with the diamond suspension since this would introduce unnecessary organic contamination to the sample before sintering.

.

3.5.2 Deposition

Before deposition, the suspension was made up and then left to age for 1 hour. The suspension was then ultrasonically treated to break up any agglomerates. The working electrodes were washed with Sunlight liquid soap, then rinsed with their respective EPD solvent and dried before being weighed. Counter electrodes were washed with the same procedure.

Alumina deposition was carried out on stainless steel electrodes wrapped in aluminium foil. The aluminium foil wrap was used to facilitate deposit removal at a later stage and prevent cracking of the deposit during drying. Wax and/or plastic tape were used as masking agents to ensure a constant deposition area of $2cm^2$ as shown in Figure 3.3. The counter electrode, an 25mm x 100mm x 0.1mm stainless steel plate, was intentionally bigger than the exposed area on the working electrode so as to provide a smooth electric field across the two electrodes. The electrodes were held parallel in a vertical fashion using a Perspex separator. For alumina deposition, the electrodes had a separation of 2cm.

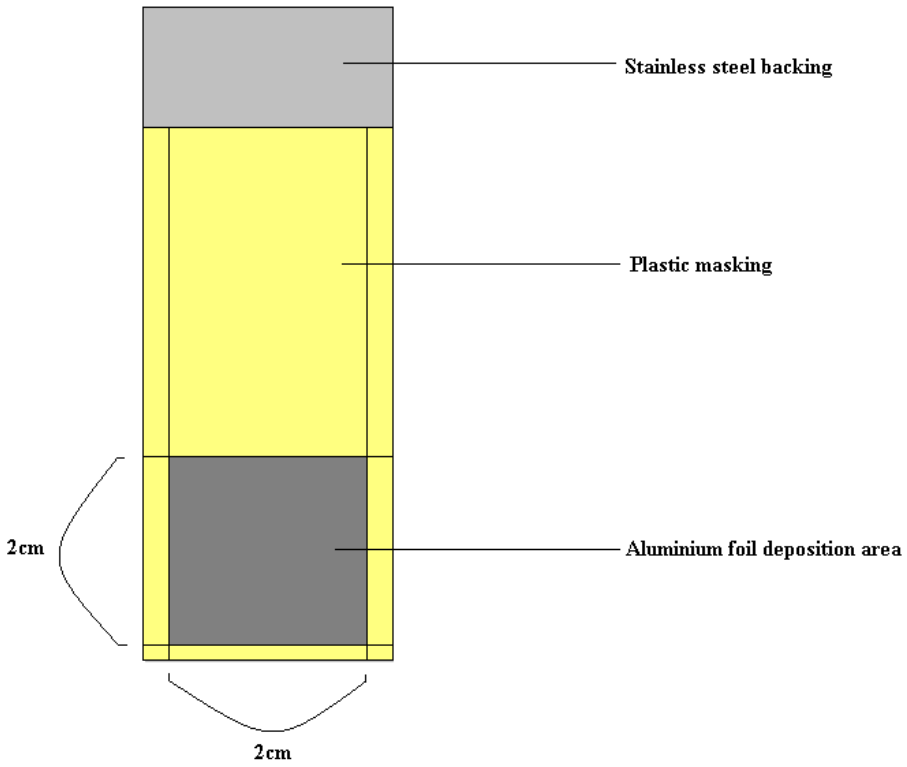


Figure 3.3: Schematic of the working electrode used for alumina deposition.

Diamond deposition was carried out onto the carbide discs with stainless steel plates acting as counter electrodes. The same counter-electrode was used as in the alumina experiments. The Perspex holder ensured a constant separation of 1.2cm. The carbide working electrodes were held in a plastic holder which also served to ensure deposition did not occur on the back or sides of the disc. The plastic holder was mounted onto a glass backing to ensure the electrodes were parallel as is shown in Figure 3.4.

The electrodes were connected by wire either to a Heathkit power supply which was used for voltages 5-400V, or a Current Automation power supply which was used for voltages of 1-5V. Exact voltages were ensured using a Major Tech MTD81 digital multimeter. The multimeter had a claimed accuracy of ±0.5% rdg + 2dgt when measured in either the 2V or 200V range. Deposition time was measured from the

point the electrodes were submerged in the suspension and the power supply was switched on, to the point it was switched off. A constant, gentle (150rpm) stirring action was applied to the suspensions during deposition by means of a magnetic stirrer bar to help reduce settling during deposition.

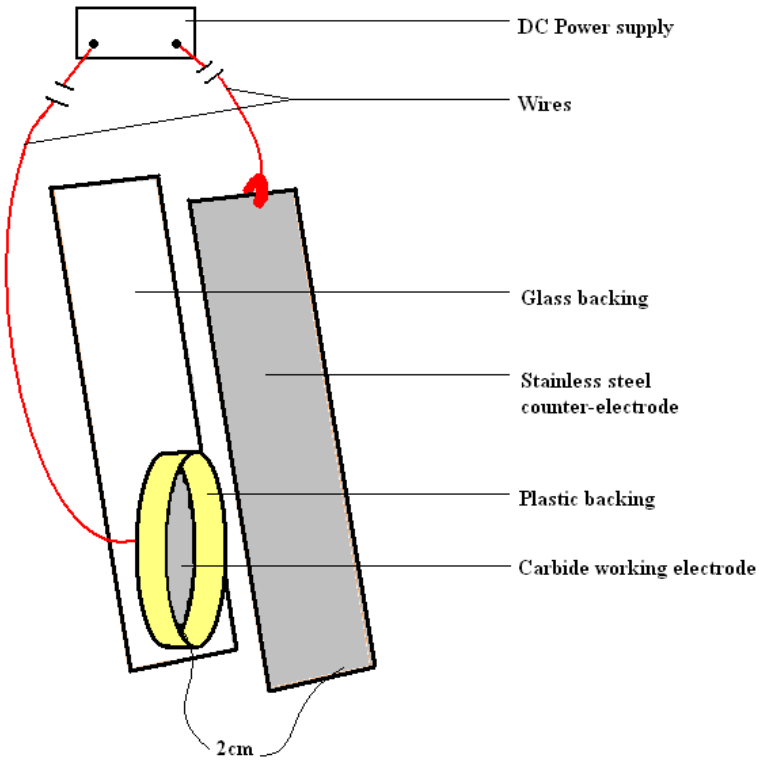


Figure 3.4: Schematic showing the experimental setup of both the working electrode and the counter-electrode.

For laminate deposits, a robotic arm (Figure 3.5) to automate the process was invented and developed by the author. The arm, which was built by BV Profiling, was programmed to move and submerge the electrodes into the two different suspensions automatically. The time and the number of cycles were adjustable on the machine. Once deposition of one layer was achieved, the power was disconnected and the

electrodes were immediately removed from the one suspension and placed into the second suspension. The power was then switched on again for deposition of the next layer.



Figure 3.5: Robotic arm to automate movement of electrodes between two different suspensions for laminate deposits.

3.5.3 Drying

After deposition, alumina deposits were left to dry in air overnight. Once dry, the alumina deposit was removed from the aluminium foil and weighed.

For diamond deposits, the carbide substrate along with the adhered diamond deposits were carefully removed from the plastic holder and placed in a desiccator with self-indicating silica gel to dry for 3 days. Once dry, the deposit and carbide substrate were

weighed. The weight of the deposit was calculated by subtracting the mass of the carbide disc from the mass of the carbide disc with the dried, adhered deposit.

3.6 Sintering

Sintering of ceramics leads to densification of the material by means of grain growth, grain-to-grain bonding and pore elimination. The procedure of sintering both alumina and diamond is described in this section.

3.6.1 Pre-sintering preparation

The alumina deposits required no special pre-sintering preparation.

The carbide discs with the adhered diamond deposit were carefully placed deposit-side down into niobium cups. Alumina-coated niobium cups were also used. The cups were then outgassed in a Bulzer vacuum furnace for about 10 hours. The vacuum furnace is used to remove adsorbed gases and surface impurities which may oxidize before sintering. Once outgassed, the sample is double cupped using a tantalum cup and sealed using electron beam (EB) welding.

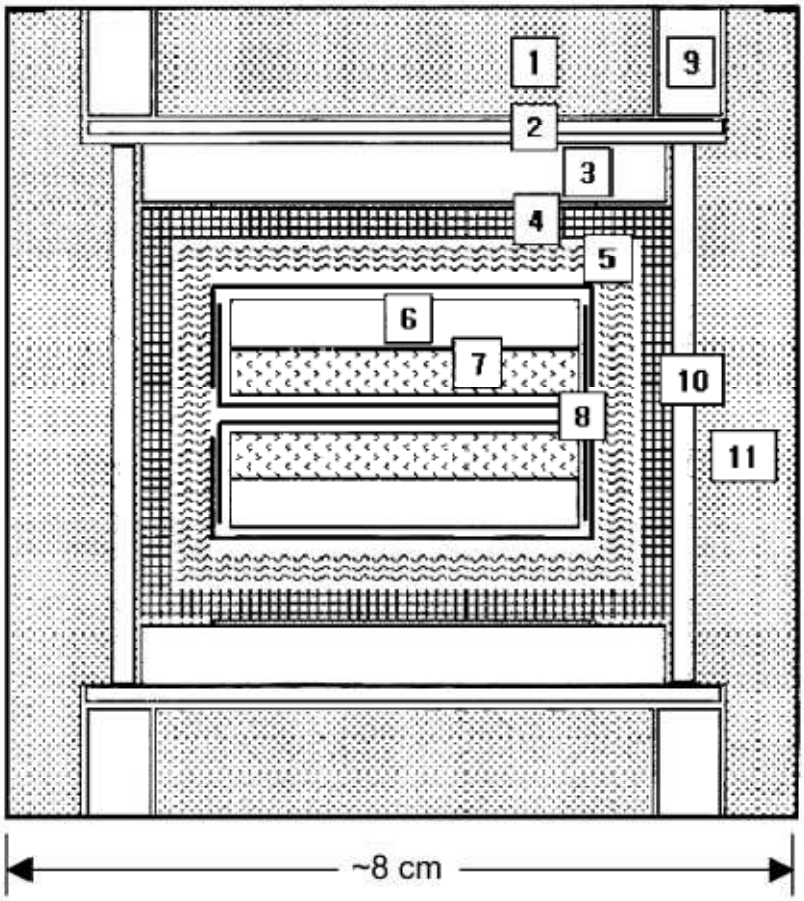


Figure 3.6: A typical HPHT assembly used for the sintering of PCD. 1) Pyrophyllite disc, 2) Mo end disc, 3) alumina disc, 4) Crucible, 5) salt nest, 6) WC-Co substrate, 7) diamond powder, 8) Nb cup and Ta double-cup, 9) current ring, 10) graphite heater, 11) pyrophyllite case. Adapted from [51].

3.6.2 Alumina Sintering

Densification of alumina deposits was achieved by means of pressure-less sintering in a muffle furnace at a temperature of 1550ºC for 6 hours. The ramp rate of the furnace was 5ºC/min.

3.6.3 HPHT diamond Sintering

High Pressure High Temperature of (HPHT) sintering of diamond was carried out according to Element Six's standard diamond sintering procedure in a belt-type press. The simplified setup is shown in Figure 3.6. Sintering promotes bonding between the diamond grains and leads to densification of the diamond layer. All samples were sintered at the same conditions at a pressure between 5.6GPa and 6.8GPa, and a temperature between 1400^0C and 1600^0C. In order to protect trade secrets, the exact details of the sintering conditions and procedures will not be divulged.

0.5µm and 2µm grade samples were also made using the traditional powder-pressed preparation as standards for comparison. These samples were made by the traditional powder-compaction technique rather than EPD. Other than this step, the preparation of these samples was the same as the EPD samples.

3.7 Preparation of sintered materials for characterization

Various preparation steps are necessary prior to characterization. These procedures are described in this section.

3.7.1 Cutting, grinding, polishing and etching

Sintered alumina samples were cut with a circular diamond blade using a Struers Secotom-10 cutting machine at a feed rate of 0.1mm/min. In order to ensure a flat surface, various steps of grinding and polishing were performed. The cut piece was then hot mounted into Bakelite resin using a 30mm diameter Struers Citopress-10 hot mount press. The mounted sample was then placed into a Leco Spectro System automatic grinder and polisher. The exact steps used during the grinding and polishing procedure are listed in Table 3.3.

Table 3.3: Grinding and polishing steps for sintered alumina deposits.

Step No.	Description	Grit	Speed (rpm)	Load (N)	Time (min)
1	Coarse grinding	220	300	35	Until level
2	Fine grinding	1200	150	35	2
3	Fine grinding	9µm	150	35	10
4	Polishing	3µm	150	30	8
5	Fine polishing	1µm	150	25	2
6	Ultra-fine polishing	0.04µm	150	25	1

In order to analyse the microstructure of the sintered alumina samples an etching step was necessary. Etching of samples is achieved by selectively attacking the material at the grain boundaries. Alumina samples were etched at 1200ºC for 2 hours in a muffle furnace at a ramp rate of 5ºC/min.

Diamond samples were wire EDM (Electrical Discharge Machining) cut to reveal the cross-section. The cross-section was then ground to remove damage at the heat affected zone. The final step involved polishing the cross-section for microstructural analysis. For the diamond laminate, an ion-beam polishing technique was incorporated.

3.8 Characterization

Success or failure of experimental work is judged by means of various characterization techniques. The techniques and equipment used are described in this section.

3.8.1 FTIR

FTIR or Fourier Transform Infrared spectroscopy is a technique that uses infrared radiation to determine important information about the functional groups present on the surface of the particles. FTIR measurements of the alumina powder were not necessary.

A ThermoNicolet Avatar 370 FT-IR was used to obtain spectra of the 0.5µm diamond powder. Since the 0.5µm and the 2µm powders are manufactured in similar processes, it was assumed that the surface groups of the two powders would be the same.

3.8.2 Particle size distribution

The particle size analyser uses the scattering of light to determine the particle size. Particle size distribution of the alumina and diamond powders was obtained by a Malvern Mastersizer 2000. A dispersant (Dolapix CE 64) was used to prevent agglomeration of particles during particle size analysis.

3.8.3 Zeta-potential

The Zetasizer uses a pulsed voltage together with a light detector to determine the scattering and thus is able to give information about the zeta-potential of the suspended particles. Zeta-potential measurements were not performed on alumina powders. Zeta-potential measurements of the 0.5µm diamond powder were obtained using a Malvern Zetasizer Nano (Figure 3.7) at Frauenhofer IKTS. Measurements were performed in both aqueous and alcoholic suspensions of the 0.5µm diamond. Hydrochloric acid and potassium hydroxide were used to control the pH of the suspensions. Topas UDS751 was used as a diamond dispersant. Since the 0.5µm and the 2µm powders are

manufactured in similar processes, it was assumed that the powders would exhibit similar behaviour in water due to their similar surface chemistry and treatments.



Figure 3.7: A picture of the Malvern Nanosizer with the auto-titrator and pH meter on the right.

3.8.4 Density and porosity

Density (ρ) and open porosity (P_o) of samples were calculated using the Archimedes' method.

The sintered alumina samples were dried in a drying oven for 20 minutes, allowed to cool to room temperature and weighed to determine the dry mass (m_d). These were then boiled in distilled water for three hours in order to saturate the open pores with the liquid and displace the trapped air. Once the samples were boiled and allowed to cool

to room temperature, they were suspended in distilled water to determine the suspended mass (m_s). The sample was then removed from the liquid and rolled three times on paper towel to soak up excess water from the surface. The samples were then weighed to determine the wet mass (m_w). All measurements were done in triplicate and the average value was calculated. The density was calculated using Equation 3.8-1 and the open porosity using Equation 3.8-2.

$$\boldsymbol{\rho} = \left(\frac{\boldsymbol{m_d}}{\boldsymbol{m_d - m_s}}\right)\boldsymbol{\rho_{solvent}} \qquad \textbf{Equation 3.8-1}$$

$$\boldsymbol{P_o} = \left[\mathbf{1} - \left(\frac{\boldsymbol{m_s - m_d}}{\boldsymbol{m_s - m_w}}\right)\right]\mathbf{100}\% \qquad \textbf{Equation 3.8-2}$$

The density was then calculated as a percentage of the theoretical density of the material by using Equation 3.8-3.

$$\boldsymbol{\rho_{\%theoretical}} = \left(\frac{\boldsymbol{\rho}}{\boldsymbol{\rho_{theoretical}}}\right)\mathbf{100}\% \qquad \textbf{Equation 3.8-3}$$

.

The densities of the 0.5µm and the 2µm monolithic green deposits were obtained using the Archimedes method in hexane to avoid destruction of the green body. Since the surface of the diamond particles is relatively polar due to the various polar groups, using a non-polar solvent such as hexane would allow measurements to be made without destroying the sample. This method may give unreliable results and is thus an approximation at best. Samples were submerged in hexane and placed in a vacuum desiccator for 30 minutes in order for the hexane to penetrate the pores. A beaker of hexane was placed in the weighing compartment for 20 minutes in order to increase the

vapour pressure of hexane during weighing. This was done in an attempt to limit the evaporation of solvent during weighing. Even with the precaution of leaving a beaker of hexane in the weighing compartment to reduce evaporation of the solvent, it is expected that a fair amount of solvent evaporates from the sample. Thus, measurements performed using the Archimedes method in hexane could underestimate the green density of the samples by around 10%.The green density using the hexane was calculated using Equation 3.8-1. The density was also calculated as a percentage of the theoretical density of the material by using Equation 3.8-3. The sintered density of the diamond was not determined. The reason for this is that the sintered product contains diamond in addition to tungsten and cobalt and thus the only significance of the density value would be to determine the amount of metal in the diamond which was already achieved through image analysis.

The theoretical densities of pure alumina and diamond are presented in Table 3.4.

Table 3.4: Theoretical densities of the pure materials used in this project

Substance	Theoretical density (g/cm^3)	Reference
Alumina	3.98	[58]
Diamond	3.52	[59]

3.8.5 Hardness testing

Hardness of sintered alumina samples were measured by Vickers indentation. The hardness of diamond was not determined since measurement would break the indenter tip. A Leco V-100-A2 micro-indenter was used to with a 1kg load. Indentations were measured using the optical microscope under a 200x magnification. The Vickers hardness was calculated using Equation 3.8-4.

$$H_v = \frac{1.8544}{d^2} F$$ **Equation 3.8-4**

Measurement *d* is the average length of the diagonals of the indent in millimetres and *F* is the applied load in N.

3.8.6 Crack propagation

A controlled crack was forced through the material by using a 3-point test jig to qualitatively investigate for evidence of crack deflection. Before crack analysis could commence, it was necessary to introduce a notch in the sample. A pre-notch was done by EDM cutting into the carbide. The pre-notch served as a guide for the blade during notching. Notching was accomplished by placing the sample into an Exakt V-notcher machine. The V-notcher works by moving a fastened sample forwards and backwards continuously while a fixed stainless steel razor blade is pressed into the pre-notch. This results in the blade cutting into the pre-notch. Progressively finer slurries of diamond were introduced to the razor blade to produce an increasingly sharper notch. Diamond slurries used were 9, 3 and 1µm diamond powder mixed with water. The notch was progressed through the carbide and extended as close to the diamond table as possible.

The notched sample was then placed into a 3-point bend jig as shown in Figure 3.8. The sample was then tested using a Tinius Olsen H50K-TUTM equipped with a 50kN load cell. The test was controlled and recorded by the program QMAT (v5.43). The load piston advance speed during testing was at minimum value (0.001mm/min) so as to provide the best possible conditions to observe crack deflection. The load was applied until sample failure.

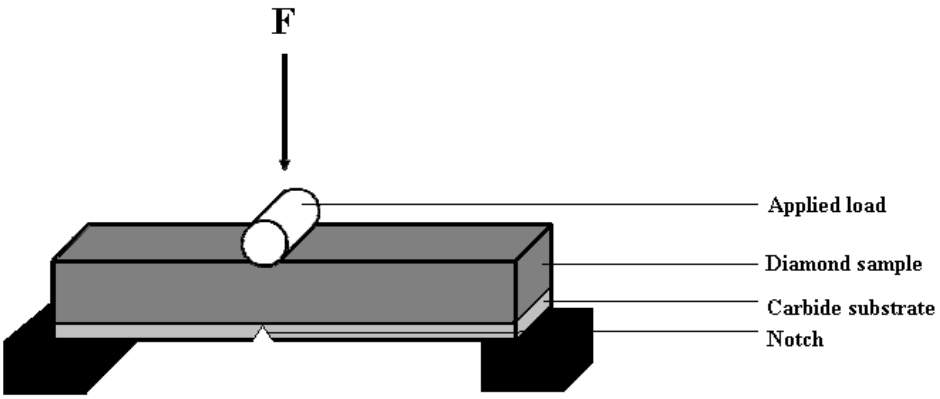


Figure 3.8: Schematic of the 3-point bend jig apparatus used to produce a controlled crack.

3.8.7 Microscopy

3.8.7.1 Optical microscopy

A Carl Zeiss AxioCam MRc AV31-KS light microscope was used to obtain images of general microstructure requiring less than 1000x magnification. Axiovision v3.1 image processing software was used to capture images and make measurements.

3.8.7.2 *SEM*

For samples requiring a magnification of more than 1000x, a Philips XL 30 ESEM-FEG series was used to obtain SEM (Scanning Electron Microscope) images. The field electron gun was capable of operating in the range of 3 to 30kV.

SEM pictures of both the 0.5µm and the 2µm diamond green deposits were obtained to investigate the particle packing. A micrograph of the interface between the 0.5µm and the 2µm laminate green deposit was also taken to show the morphology between the layers.

SEM images of the cut, ground and polished cross sections of both alumina and diamond samples were obtained. Images of the alumina samples were used to show structure of the grains and general microstructure. Images of the diamond samples were used to observe diamond to diamond bonding, evidence of grain growth and morphology of the layers.

EDX and image analysis (analySIS Five) was done across the sintered diamond laminate deposit to show fluctuations in cobalt content.

4. Results

4.1 Introduction

This section presents the results, measurements and observations obtained from the experiments. The results are divided into two main sub-sections. One subsection contains work done on alumina another contains work done on diamond.

4.2 Alumina EPD results

4.2.1 Initial observations

Alumina deposition was achieved onto stainless steel electrodes. Coatings were well adhered and were relatively uniform as seen in Figure 4.1. Deposition did not occur on the wax masking as is shown in Figure 4.1. Deposits only formed on the cathode for alumina deposition.

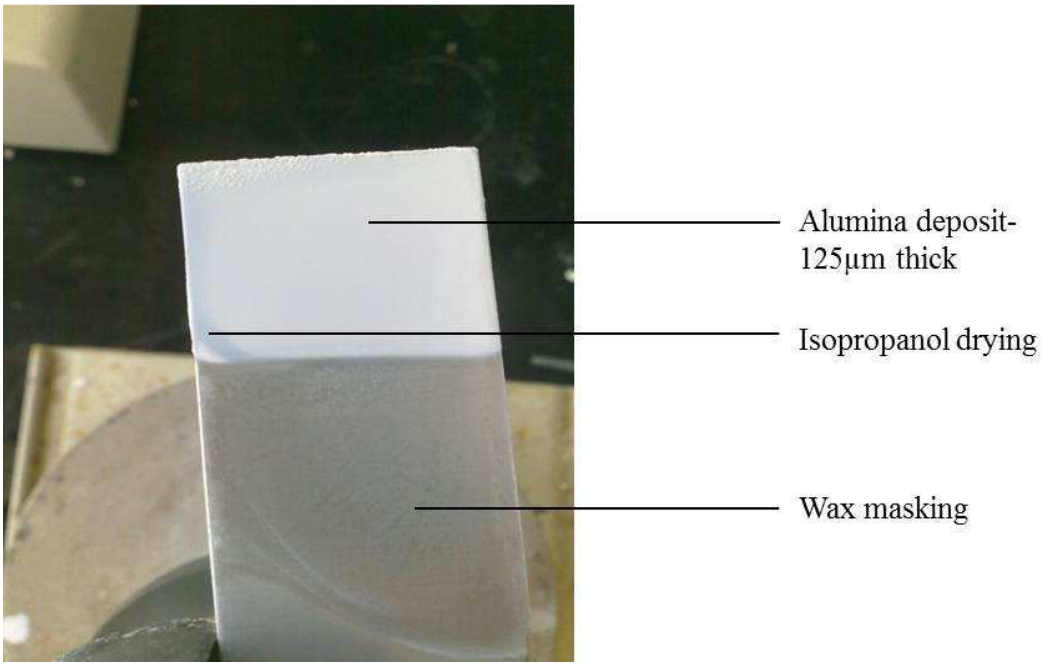


Figure 4.1: A typical electrode after deposition. This deposit was made at pH 5.7, 10% (w/v) alumina in isopropanol, 10 min at 100V/cm.

Although the principle of EPD is relatively simple, several challenges were encountered during deposition of alumina. One such problem was the formation of cracks in the deposit after deposition during the drying step. These cracks occurred primarily in deposits thicker than 200µm.

Several techniques were attempted to prevent the deposit cracking during drying. The techniques attempted, the deposition variables and deposit thickness are summarised against the observations made in Table 4.1.

Table 4.1: Various techniques attempted to facilitate crack-free drying of alumina deposits.

Technique	Parameters				Deposited on edges	Crack Description	Deposit Thickness	Final Observation
	Voltage (V/cm)	Conc. (g/100mL)	Time (hr)	% PEG (mass %)				
Solvent Mixture (50% iPrOH, 50% acetone)	150	10%	2	0	Yes	Large network of cracks	~500µm	No visible improvement
Varying PEG-400 amounts	175	10%	1	0-0.4%	Yes	Decreasing with Increasing PEG	50-500µm	Improvement due to thinner deposits (PEG causes weight decrease of deposit)
Deposit onto cellulose membrane	150	10%	1	0	No	*	*	Bulge of i-PrOH trapped under membrane leading to curved deposit
iPrOH rich atmosphere	150	10%	2	0	Yes	Large network of cracks develops when removed from isopropanol atmosphere	~500µm	No cracks develop while in saturated atmosphere however instantly appear when placed in ambient atmosphere
Deposit onto alumium foil	150	10%	1	0.1	No	No visible cracks on centre of deposit. Cracks form where deposit adheres to masking agent	~2mm	Deposit densifies while drying without any major cracking unless in contact with mask.

* No deposit formation

The first attempt to reduce cracking was changing the suspension make-up to include 50% acetone 50% isopropanol. This was done in order reduce the viscosity of the suspension media. This efficacy of this method was evaluated visually and it was found that no improvements were made.

The second attempt involved adding PEG-400 binder to the suspension in order to give deposits higher strength.

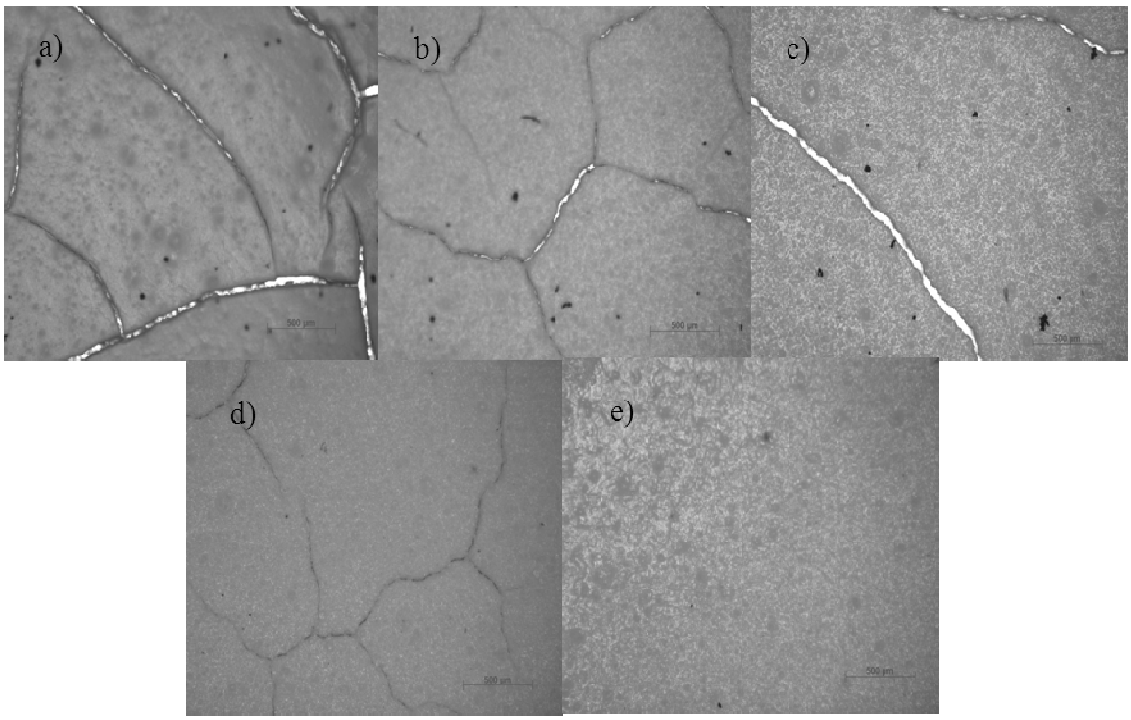


Figure 4.2: Effect of PEG-400 addition on the formation of cracks in the deposit. Weight per cent PEG-400 addition to suspension: a) 0% b) 0.1% c) 0.2% d) 0.3% e) 0.4%.

The results of PEG-400 addition are shown in Figure 4.2. Although it may seem that the number and size of the cracks are reduced, it is important to note the weight of each of the deposits. A graph of deposit weight versus PEG-400 addition is shown in Figure 4.2.3.

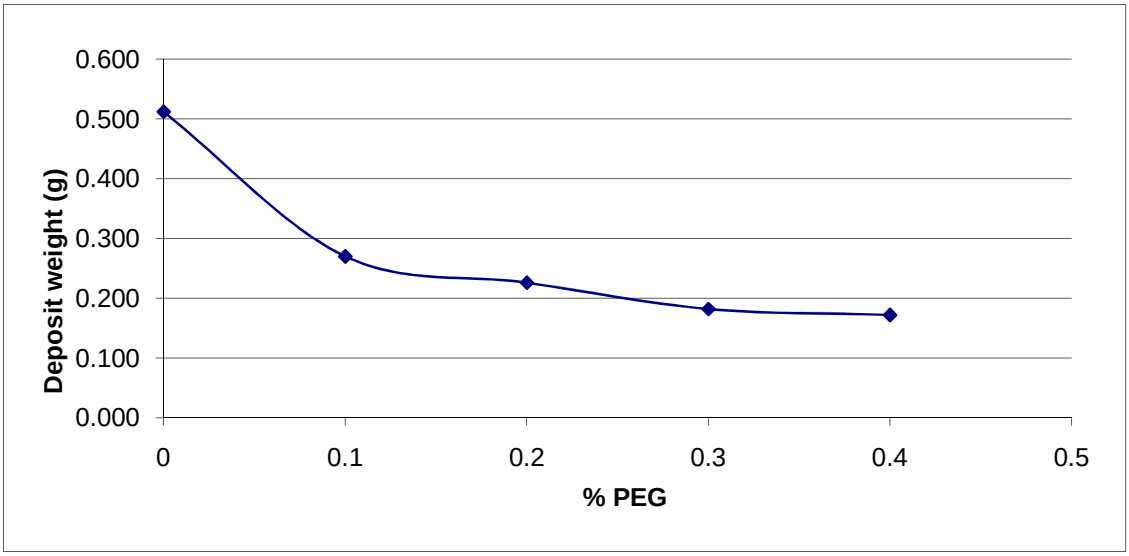


Figure 4.3: A graph showing the weight of the deposit versus % PEG-400 addition. Deposits were made using 175V/cm, 10% (w/v) for 1 hour.

As is evident in Figure 4.3, the deposit weight decreases with increasing PEG content. Therefore one is not able to conclusively say that PEG reduces crack size.

It was suspected that depositing on the edges (side surface of the electrode) played a role in crack formation. Another method to attempt the reduction of cracking involved depositing onto a cellulose membrane wrapped around the stainless steel electrode. In this experiment, a bubble of isopropanol developed underneath the membrane. This was probably due to electro-osmotic flow of the isopropanol through the membrane towards the electrode where it was eventually trapped. This was problematic since deposits were no longer planar. A schematic of the result of this method is shown in Figure 4.4.

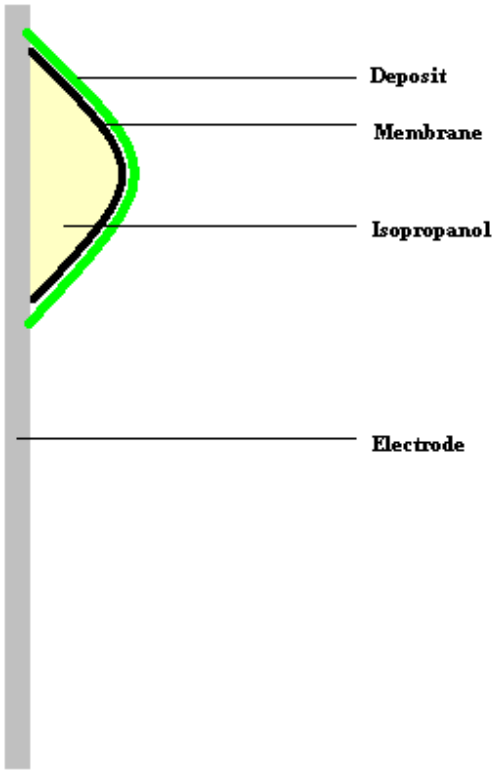


Figure 4.4: A schematic of the side view of the electrode illustrating the trapped isopropanol underneath the membrane.

Control of the drying environment was also attempted. Deposits were dried in isopropanol rich environments such that the drying rate is reduced. This showed no visible improvements in stopping crack formation. The cracks took longer to form while in the isopropanol rich environments, but inevitably formed when deposits achieved full dryness.

Another technique to try and avoid cracks was depositing onto a layer of aluminium foil that was wrapped around the electrode as in Figure 3.3. During the drying process, the deposit would lift off of the aluminium foil during drying and thus dried independently from the electrode. Deposits made in this manner did not crack upon drying unless the deposit was in contact with the plastic masking. Thus, straight after

deposition, edges that were in contact with the masking were carefully cut away from the main body of the deposit. Using this method insured all subsequent alumina deposits were free from cracks caused by drying.

4.2.2 Deposition rates

The deposited weight versus the applied voltage is given in Figure 4.5. These measurements were performed while keeping all other variables constant

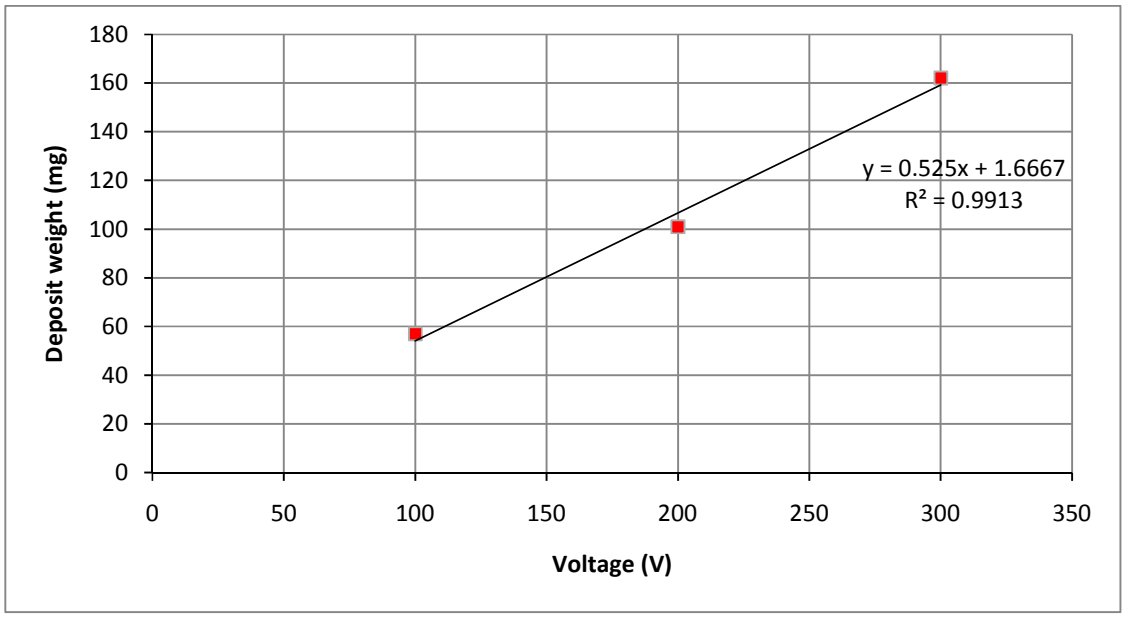


Figure 4.5: Deposit weight versus applied voltage for a suspension of pH 5.0, 10% (w/v) for 15 minutes.

A graph of deposit weight versus time is shown in Figure 4.6. The slope of the graph gives the deposition rate. The deposition rate of a 10% (w/v) suspension made with a pH 5.0 at 100V/cm is 1.84mg/(cm^2.min).

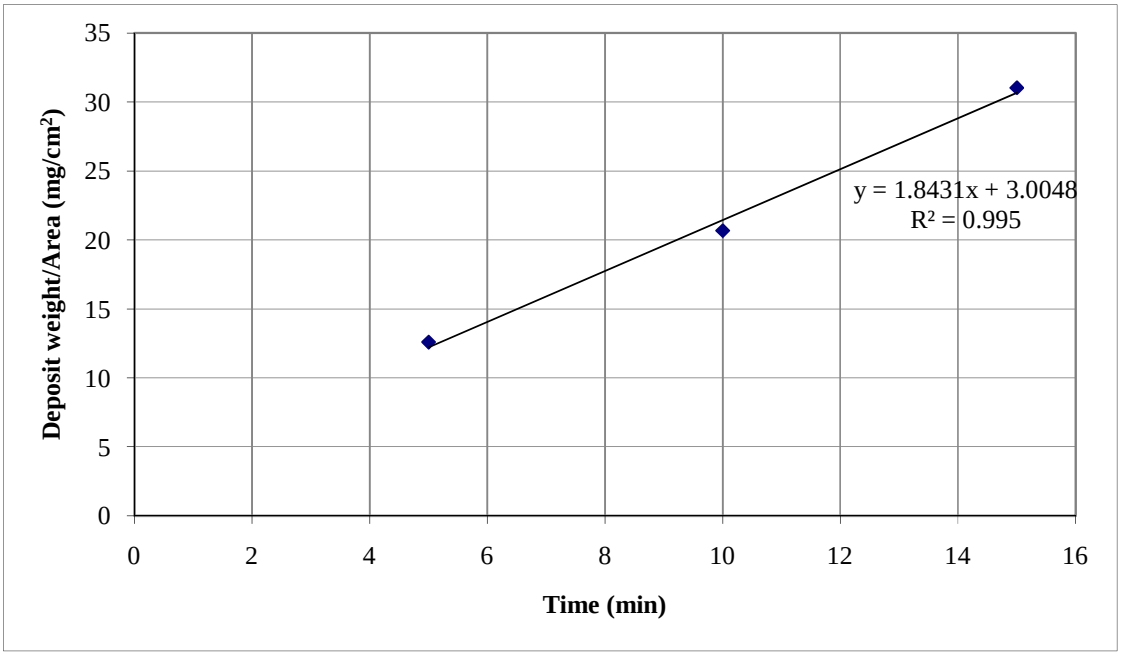


Figure 4.6: Deposit weight versus time for a suspension of pH 5.0, 10% (w/v) at 100V/cm.

The dependence of concentration against deposit weight was not measured due to the fact that pH control in isopropanol proved to be extremely difficult and thus it was near impossible to make alcoholic suspensions with the same pH.

4.2.3 Representative samples

Two samples were chosen and were representative of alumina deposits. The two samples: Sample 41 and Sample 42 were made using the conditions listed in Table 4.2.

Table 4.2: EPD parameters for Sample 41 and 42.

Sample	Conc. (g/100ml)	Voltage (V/cm)	Time (hours)	PEG-400 (mass %)
41	10	50	1	0.1
42	10	37.5	1	0.1

Sample 41 shown in Figure 4.7 is a square with sides measuring about 18mm and thickness measuring about 2mm. The green deposit showed good strength for a green compact and this allowed it to be handled easily without damaging it. The surface of the deposit was slightly rippled and had a blow-hole in the top left corner. This blow-hole is an artefact that occurred only once and thus can be ignored.

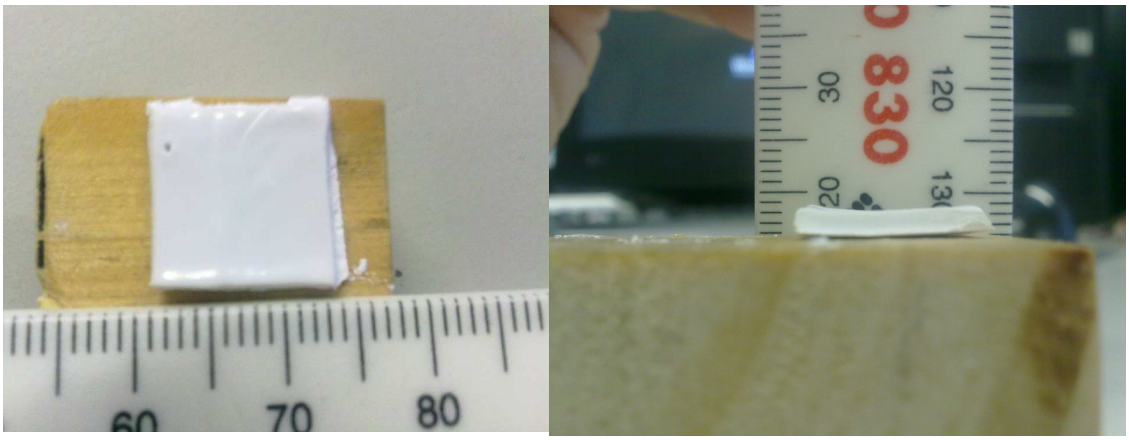


Figure 4.7: Photograph showing Sample 41 prepared using a 10% (w/v) alumina suspended in isopropanol at pH 3.7, 50V/cm for 1 hour.

Sample 42 is shown in Figure 4.8. The green deposit was machined into two pieces. The one half, shown at the top, is the unsintered green body and the other half, shown at the bottom, is a sintered piece. Sample 42 was thinner than Sample 41, and it had a

slightly smoother surface. The green density of sample was estimated at around 46% by measuring the dimensions and weight of the sample.



Figure 4.8: Photograph showing Sample 42 prepared using a 10% (w/v) alumina suspended in isopropanol at pH 3.7, 32.5V/cm for 1 hour.

The general properties of the sintered samples 41 and 42 are listed in Table 4.3. The hardness of sample 41 was not measured. Both samples had impressive densities which were very close to the theoretical densities.

Table 4.3: General properties of Sample 41 and 42.

Sample	Voltage used (V/cm)	Sample Density (g/cm^3)	% Theoretical density (%)	Open Porosity (%)	Hv_{10} (GPa)
41	50	3.96	99.1	0.81	-
42	32.5	3.94	98.9	0.46	21.6

SEM images of the sintered, cut and polished cross-sections of Sample 42 are shown in Figure 4.9. The sample was thermally etched at 1200ºC for 2 hours. From the images, it is evident that the grain boundaries were well defined. The average grain size was smaller than 5µm and the sample had a low porosity.

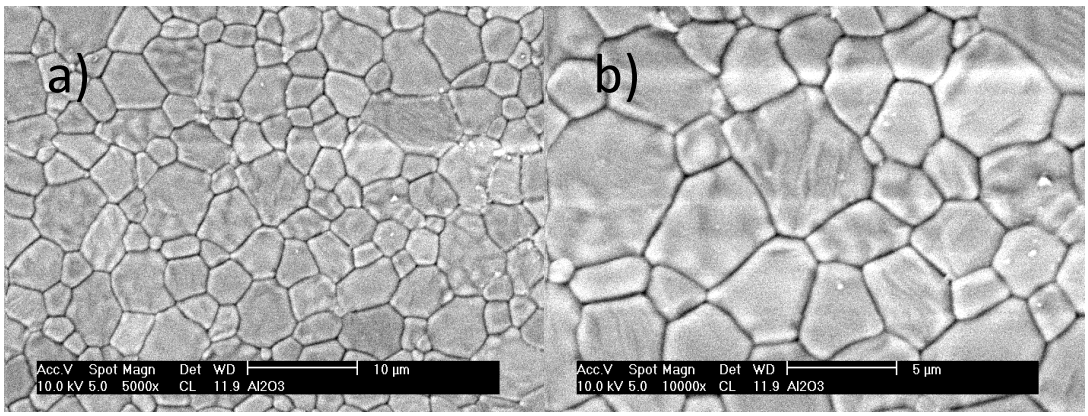


Figure 4.9: SEM micrographs of sample 42 at a) 5000x b) 10000x magnification.

4.3 Diamond EPD results

4.3.1 Suspension optimization

4.3.1.1 Surface chemistry

In order to understand the behaviour of diamond in suspension, it is important to understand the surface chemistry of the particles.

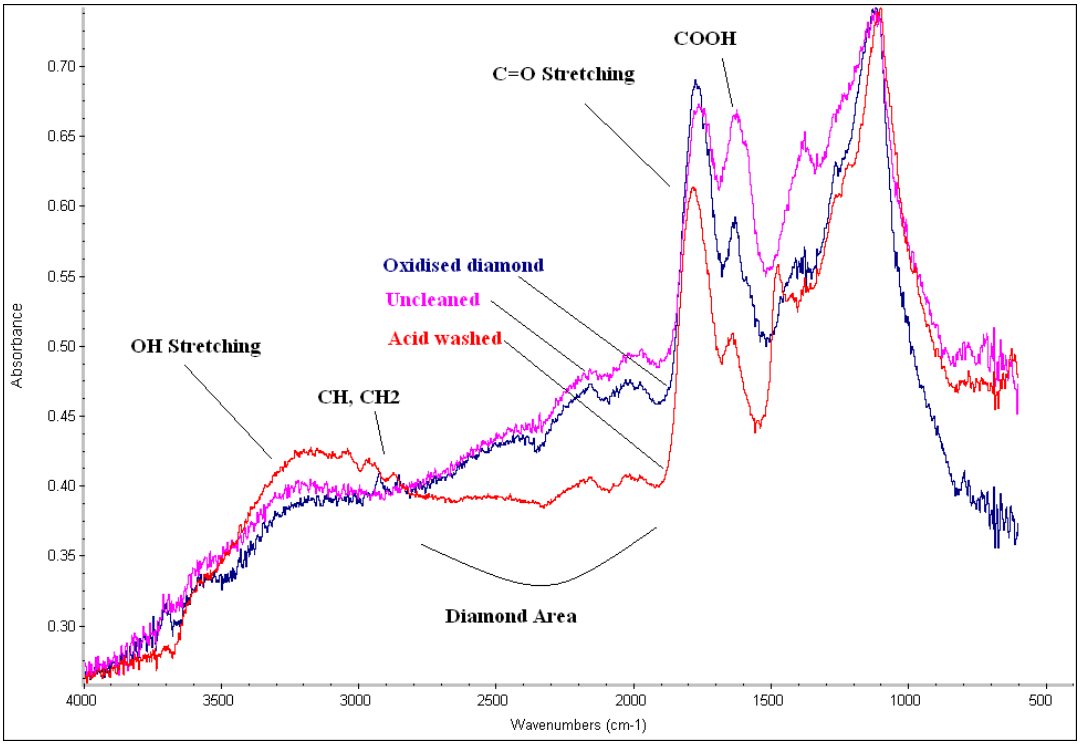


Figure 4.10: FTIR spectra of as received (uncleaned), oxidized and acid washed 0.5µm powder superimposed for comparison of surface groups.

An FTIR spectrum of the as received, acid washed and oxidised 0.5µm were superimposed for comparison (Figure 4.10). The peaks in the spectrum were labelled using from information gathered in Table 4.4. Peaks in the range 900cm^{-1} to 1400cm^{-1} are the one phonon absorption bands of diamond [60] and thus were not labelled.

Table 4.4: Characteristic FTIR peaks present in diamond.

Vibration Frequency	Functional Group	Ref.
900-1400^{-1}	One phonon absorption of diamond	[60]
1650 cm^{-1}	C-O-O-H	[61]
1714 cm^{-1}	C=O stretch	[62]
2852 cm^{-1}	C–H2 symmetric stretch	[63]
2921 cm^{-1}	C–H2 asymmetric stretch	[64]
3380 cm^{-1}	O–H stretch	[65]

The spectrum reveals that hydroxyl, carbonyl and hydrocarbon groups are present which correlates well with literature [66]. In an attempt to achieve polar surface groups, the diamond powder was oxidized to introduce oxygen containing species onto the surface. It is known that diamond powder oxidizes at temperatures above 496ºC [67]. The diamond was oxidized in air at 500ºC.

Diamond powder was also acid washed to remove metal impurities introduced during the manufacture of the powder. After the boiling of the diamond in the acid solution was complete, the supernatant liquid turned green thus indicating the presence of dissolved metals.

The acid washed diamond showed an increase in the -OH stretching band between 3500cm^{-1} and 3200cm^{-1} as well as a definite decrease in the carbonyl stretching band between 1800cm^{-1} and 1600cm^{-1}. The oxidized diamond shows a decrease in the carboxylic stretching frequency at around 1650cm^{-1}.

From the information presented above, it is difficult to predict exactly how the different treatments will affect the stability of the powder in suspension. Zeta-potential measurements were necessary.

4.3.1.2 Organic suspensions

In order to better understand the difference in behaviour of the particles following the various treatments, zeta-potential measurements in isopropanol of as-received, acid cleaned as well as oxidised/acid cleaned powder were plotted against time (Figure 4.11).

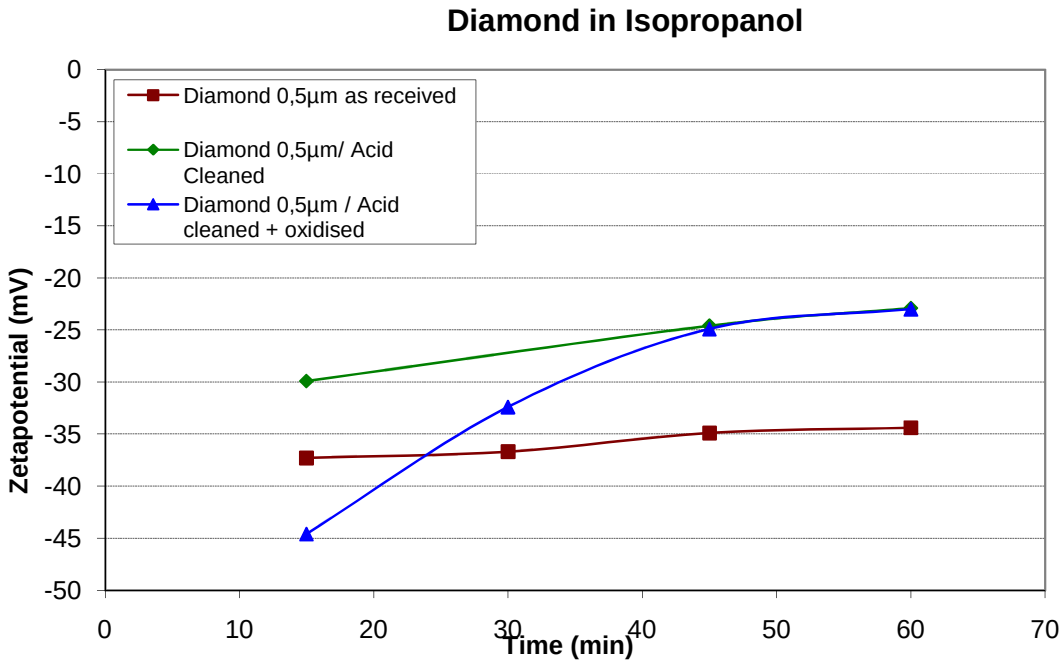


Figure 4.11: Zeta-potential measurements of as-received, acid cleaned as well as oxidized/acid cleaned powders plotted against time in isopropanol media.

Initially, the acid cleaned/oxidized diamond starts off with the most negative zeta-potential. However, after some time (45min), the zeta-potential of the powder approaches the same value as the powder that was only acid cleaned. The powders acquire the same value indicating that after some time there is no difference between

the two powders. From the data provided in Figure 4.11, it was evident that the isopropanol suspensions used for EPD work must be aged for at least one hour to allow the zeta-potential to stabilize and achieve a plateau.

After aging of the isopropanol suspensions, it is evident that the as received powder has the most negative zeta-potential (Figure 4.11). Due to the fact that there was no real difference in the measured zeta-potential between the oxidized and acid washed/oxidised powder after aging, it was decided that the oxidation step was unnecessary. Since the as received powder attained the highest zeta potential, it would thus appear to be the obvious candidate for the EPD process. However, due to the unpredictable amounts of metallic impurities present on the as received powder, an acid washing step is necessary to eliminate this variable.

Diamond suspensions made using isopropanol were highly unstable and rapid sedimentation of the particles would take place. This occurs when the force of gravity is higher than the forces that keep the particle suspended. The attempts at EPD in isopropanol are summarised in Table 4.5. This made diamond-isopropanol suspensions unusable for EPD experiments.

Table 4.5: Summary of the EPD attempts using isopropanol suspensions of 0.5µm diamond.

Action	Comment
EPD 0.5µm diamond at pH 2.3 (HCl addition)	No deposit. Suspension not stable
EPD 0.5µm diamond at pH 12.0 (NaOH addition)	No deposit. Suspension not stable
EPD 0.5µm diamond using acetone, iodine and water [36].	Conductivity too high. Suspenion became hot and bubbled

4.3.1.3 Aqueous suspensions

The diamond showed vastly improved stability in water, even without the addition of any additives. In order to find an appropriate working pH and maximize the charge on the particles, a zeta-potential scan across various pH values is needed.

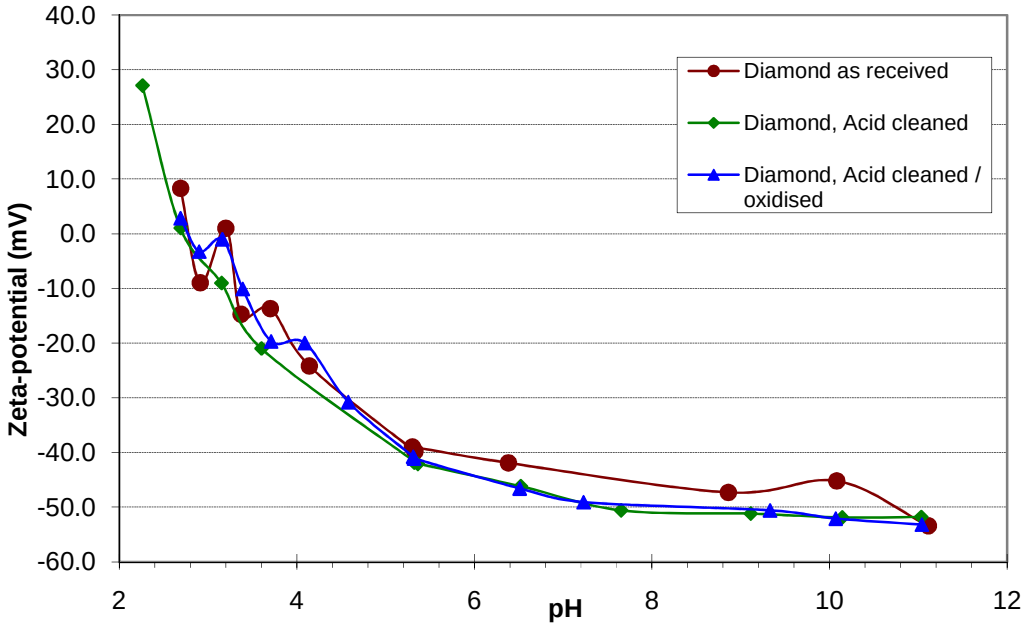


Figure 4.12: Graph of zeta-potential versus pH for the various powders in aqueous media.

Zeta-potential measurements of 0.5µm diamond powder, along with powder after the various treatments, were plotted against pH in Figure 4.12. The acid cleaned and acid cleaned/oxidised curves reach maximum plateaux at around -50mV between pH 7.5 and pH 11. Acid washing the diamond increases the negative charge on the particles by about 5mV at higher pH values as compared to the unwashed diamond. Very little difference was observed in the zeta potential plots of the powders with the various treatments.

.

4.3.1.4 Deposition of monolithic diamond.

Deposition of monolithic diamond was performed as a precursor to laminate deposition in order to learn more about the technique. Once the pH of 8.5 was chosen from the suspension optimisation stage, the first successful diamond deposit was obtained. WC-13% Co was used as the anode with a stainless steel plate as the cathode. The separation of the electrode was 0.8cm. The deposit, made by using a 3% (w/v) suspension of the 0.5µm powder, deposition time of 60 minutes and a voltage of 1.5 V/cm, formed on the positive anode thus indicating the particles had a negative charge. This is in good correlation with the zeta-potential measurements at this pH. The deposit was well adhered to the carbide substrate but was however very brittle and would break if not handled carefully. The deposit showed no evidence of gas formation at the electrode thus indicating that a voltage of 1.88 V/cm was well below the critical voltage needed for the disassociation of water.

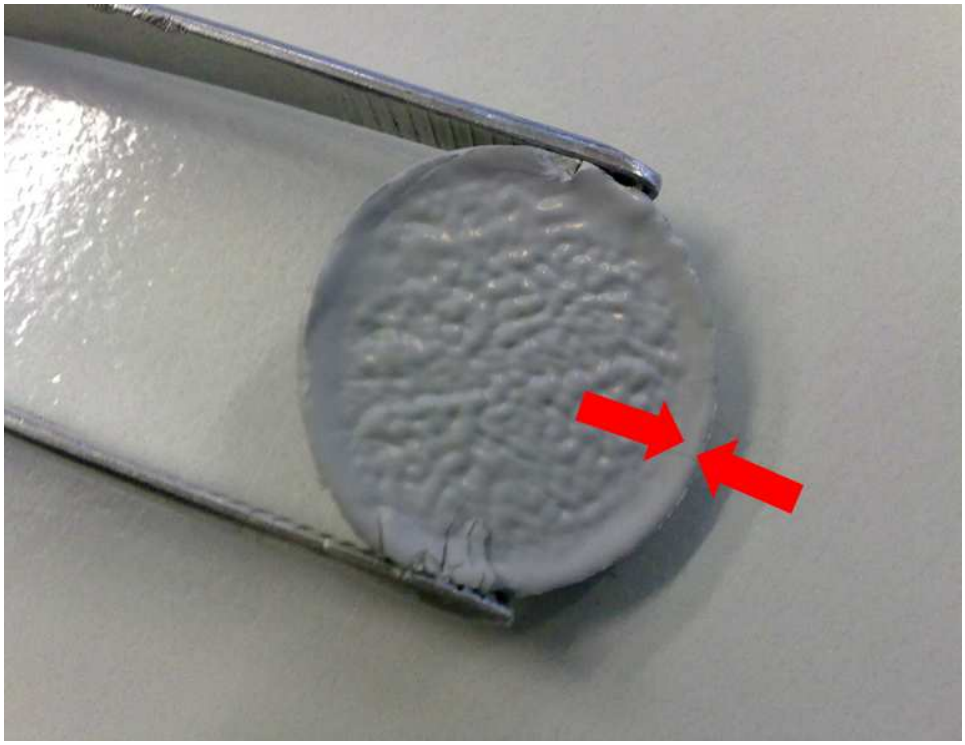


Figure 4.13: First diamond deposit obtained (Sample 47). The deposit was made using 3% (w/v), pH 8.5, 1.88 V/cm, 60 minutes.

In Figure 4.13, a top view of the diamond deposit adhered to the carbide disc is shown. The surface of the diamond contained bumps and ridges. As highlighted by the arrows in the image, the edges experienced higher deposition rates due to the fact that sharp points or edges concentrate the electric field. In this picture, the forceps are holding the carbide disc onto which the deposit is adhered. The cracks at the edges of the deposit in contact with the forceps serve to show just how brittle the deposit was.

After the information gathered from the first diamond deposit, numerous samples were made. A summary of these deposits are listed in Table 4.6.

Table 4.6: Summary of EPD experiments of non-layered samples performed at pH 8.5.

Sample No.	Particle Size (µm)	Substrate	Time (minutes)	Voltage (Volts/cm)	Concentration (g/100mL)	Deposit Weight (mg/cm^2)	Deposition Rate ($mg.cm^{-2}.min^{-1}$)
47	0.5µm	WC-13% Co	60	1.88	3%	14.2	0.24
48	0.5µm	WC-13% Co	120	1.25	3%	20.2	0.17
49	0.5µm	WC-13% Co	120	1.88	5%	53.9	0.45
50	0.5µm	DEC substrate	120	1.25	5%	40.2	0.34
51	0.5µm	DEC substrate	120	1	5%	15.8	0.13
52	0.5µm	DEC substrate	120	0.83	5%	11.6	0.10
53	2µm	DEC substrate	60	1.25	7%	10.5	0.18
54	2µm	DEC substrate	60	1.25	10%	17.5	0.29

An SEM image of a monolithic 0.5µm green deposit of a duplicate of sample 50 was obtained (Figure 4.14).

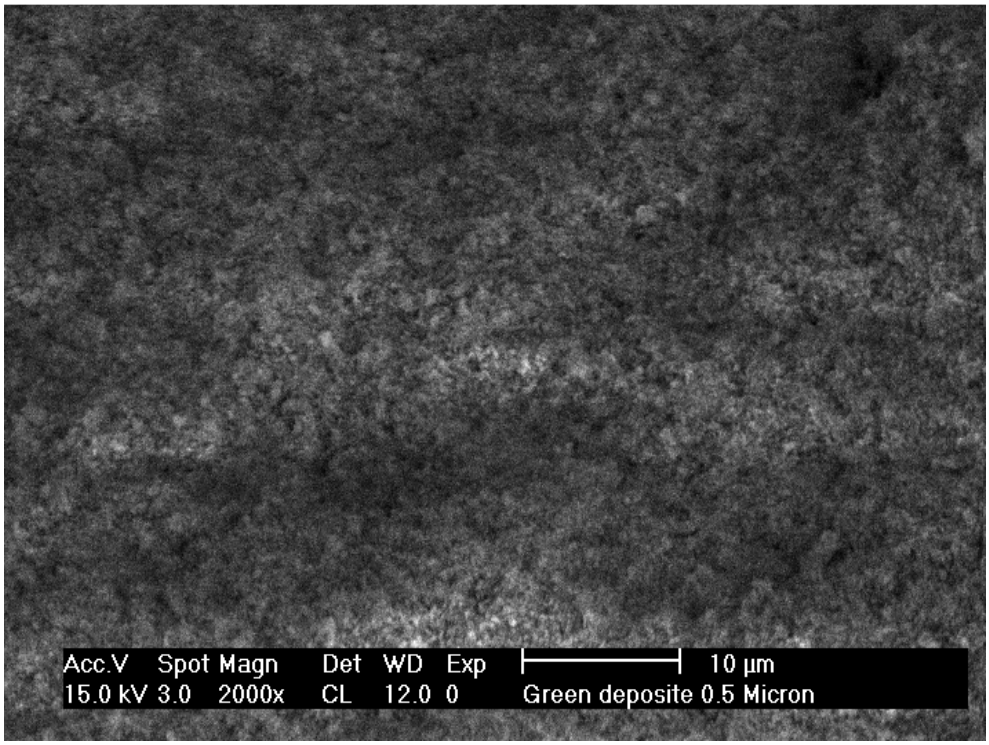


Figure 4.14: SEM image of the fracture surface of a green deposit made using a 0.5µm diamond suspension with the same conditions as sample 50.

The resolution of the SEM image is not adequate enough for a thorough microstructural analysis. It does however appear that particles are homogenously packed. The sample also seems void of large flocculated structures which are commonplace for sub-micron powders.

An SEM of a 2µm green deposit of sample 50 was obtained in Figure 4.15. From this image it was evident that particles were well packed. There was no evidence to suggest particle agglomeration.

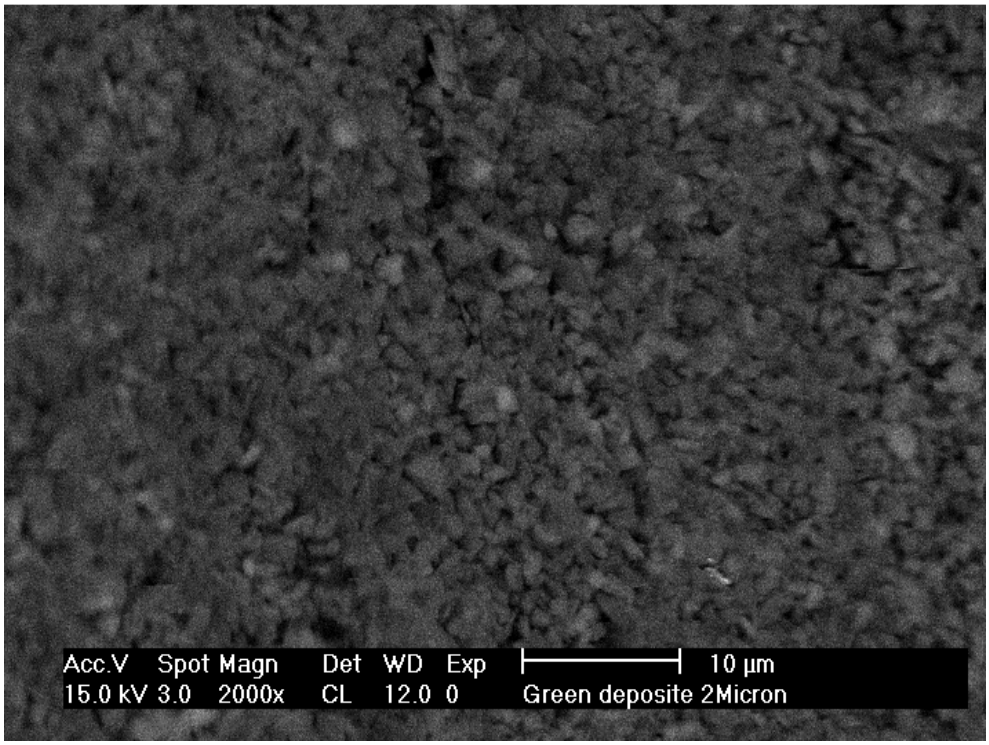


Figure 4.15: SEM image of the green deposit of a sample 53 made using a 2µm diamond suspension.

The green density and open porosity of the 0.5µm and 2µm green deposit as measured using the Archimedes method in hexane are tabulated in Table 4.7. This method may give unreliable results and is thus an approximation at best, however no better alternative to measuring green density was available. This method of calculating green density does however give an indication that the green density was around 50% of the theoretical. In the 0.5µm sample, the bulk density and observed porosity values are in agreement with each other. In the 2µm sample, there is a larger discrepancy which could be connected with the faster evaporation of hexane due to the larger pore size.

Table 4.7: Comparison of the green density, and open porosity of the 0.5 µm and 2µm green deposits.

Sample	Time (minutes)	Voltage (Volts/cm)	Concentration (g/100mL)	Green Density (g/cm^3)	% Theoretical density (%)	Open Porosity (%)
0.5µm green deposit	120	1.25	5%	1.69	48.1	48
2µm green deposit	60	1.25	10%	1.65	46.9	47

4.3.1.5 Sintered monolithic diamond deposits

Samples 48 through to 52 were sintered, cut and polished to examine for evidence of abnormal grain growth (AGG) and the efficacy of the DEC substrates in helping prevent the same. All of these samples suffered from varying degrees of AGG. Examination of each sample was necessary to determine the causes.

Sample 48 was deposited onto ordinary WC-13% Co. The approximate thickness of the diamond layer is 200µm. This entire sample suffered from abnormal grain growth as is evident in Figure 4.16. The grains grew very large indeed with some grains growing larger than 100µm in length. This phenomenon is known to occur in sub-micron diamond [51].

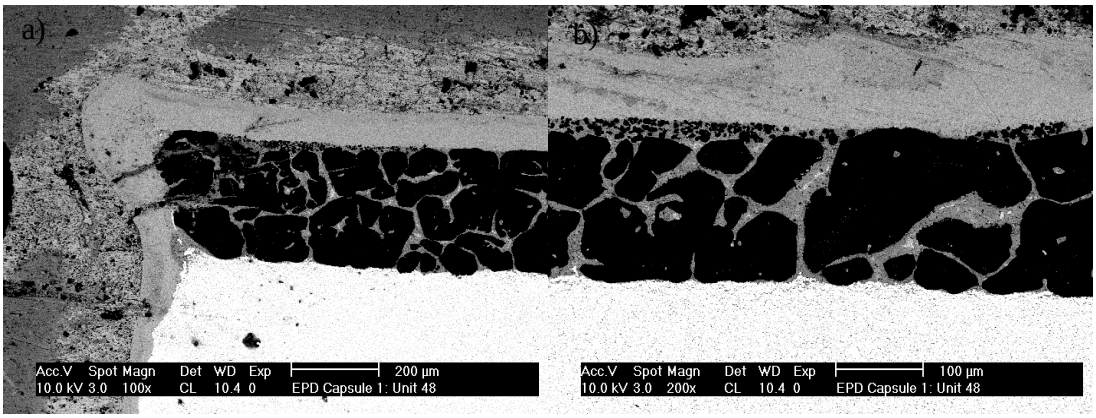


Figure 4.16: SEM of the cross section of sample 48 which was made by depositing 0.5µm diamond.

Sample 49 was produced under the same conditions as sample 48 except that the concentration of the suspension was increased from 3% to 5%. The approximate sample thickness was about 500µm after sintering. In Figure 4.17a) some grain growth is evident to the left of the micrograph. However, AGG was expected throughout the entire sample. Upon closer inspection at the diamond-WC interface in Figure 4.17b), it was evident that infiltration of the cobalt had occurred into the diamond table. Thus since grain growth had occurred to the left of Figure 4.17a)where the sample was in contact with the side of the cupping, it can be assumed that the grain growth had occurred from the niobium cup and not the carbide-diamond interface.

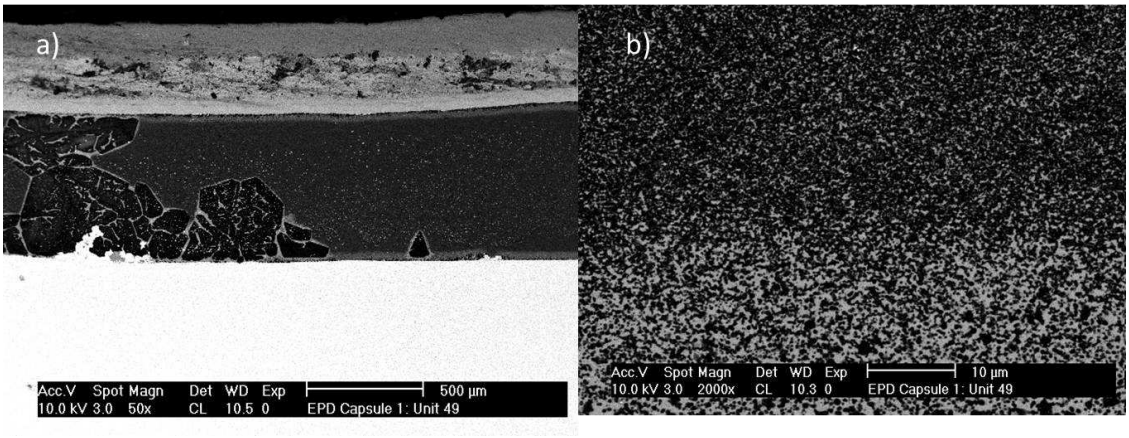


Figure 4.17: SEM of the cross section of sample 49 which was made by depositing 0.5µm diamond.

.

Sample 50 was deposited onto a DEC substrate. The thickness of the diamond layer is about 500µm. This sample was expected to show no AGG. However, upon examination of the cross-section in Figure 4.18, massive grains were evident. The diamond-carbide interface shows discontinuous AGG and the top of the diamond table shows continuous AGG along the niobium-diamond interface.

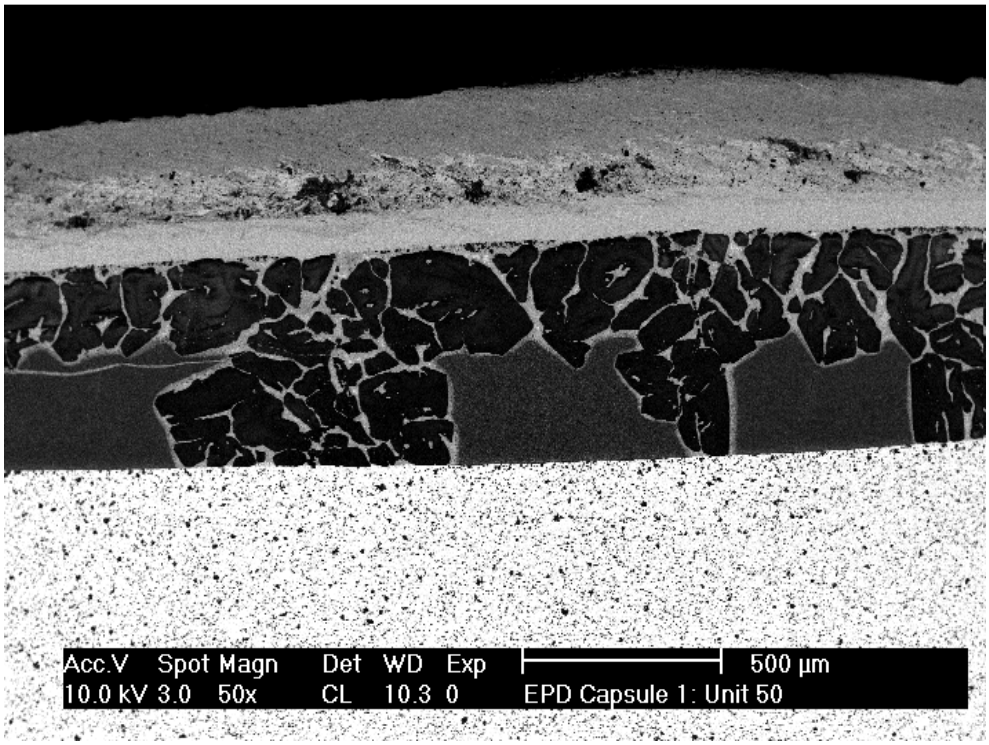


Figure 4.18: SEM of the cross section of sample 50.

Samples 51 and 52 were made at a lower voltage of 0.83V/cm onto DEC substrates. This resulted in very thin deposits which were about 150µm in thickness. Sample 51 is shown in Figure 4.19. The entire sample suffered from AGG. Sample 52 had much the same appearance as Sample 51.

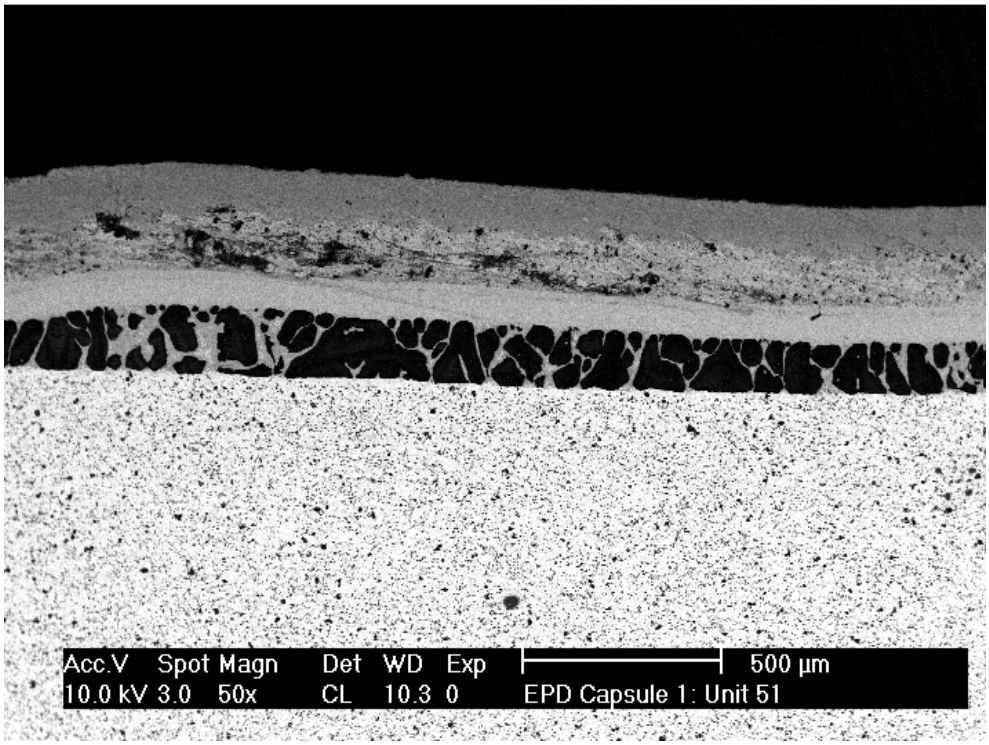


Figure 4.19: SEM of the cross section of sample 51.

4.3.2 Diamond powder pressed standards

The diamond laminate sample was compared with 0.5 and 2µm standards, which were prepared by the conventional powder pressing technology. The morphology and EDS results were analysed by SEM.

4.3.2.1 0.5µm powder pressed standard

The 0.5µm powder pressed standard was analysed by SEM and is shown in Figure 4.20. Massive grain growth was evident in the sample despite the fact that the DEC substrates and coated cups were used.

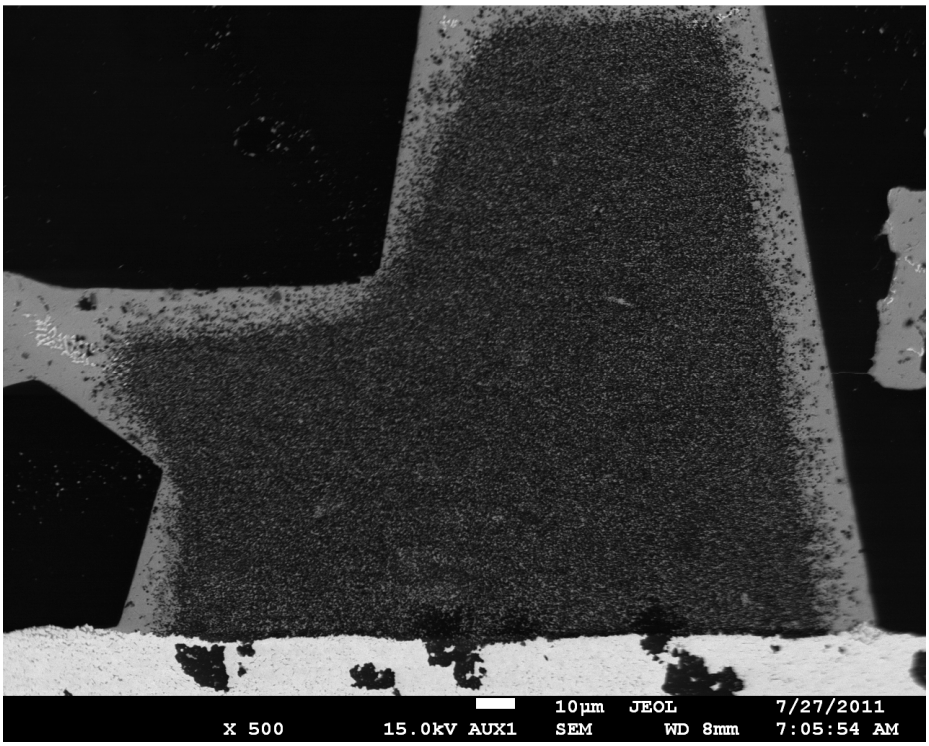


Figure 4.20: SEM of 0.5µm powder pressed standard.

Lighter and darker spots throughout the sample can be found. These spots were examined by EDS and were found to be regions if higher or lower localized cobalt concentration in the diamond table. This is a result of inhomogeneous packing of the diamond powder, These spots are visible in Figure 4.21.

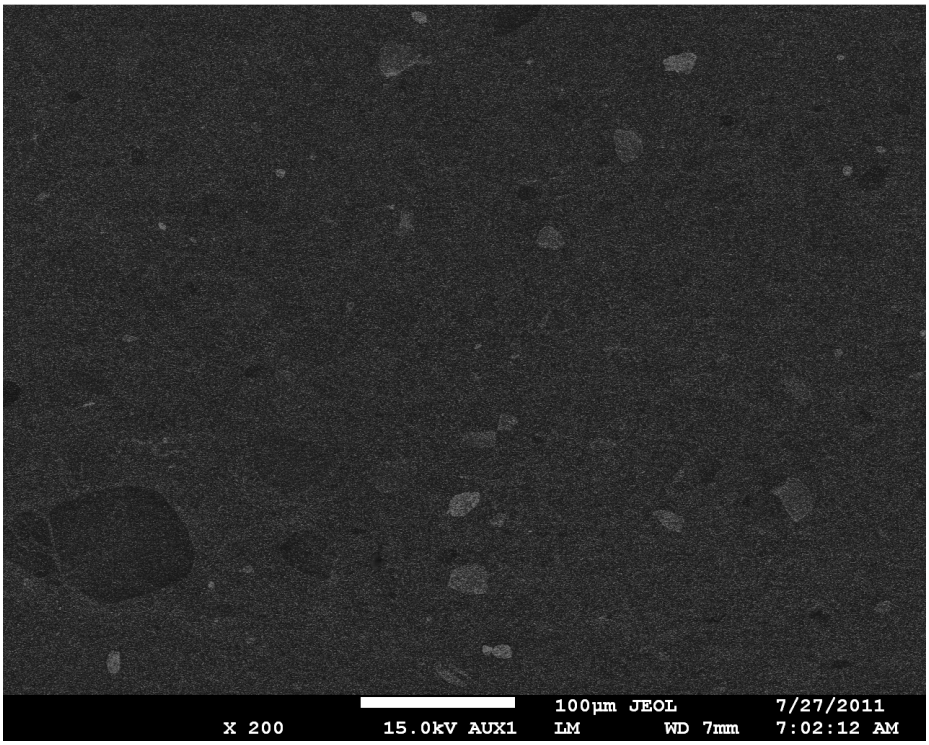


Figure 4.21: SEM showing light and dark spots in the diamond table of the 0.5µm powder pressed standard.

4.3.2.2 2µm powder pressed standard

The 2µm powder pressed standard had also suffered exaggerated grain growth to the same degree as the 0.5µm powder pressed standard. The standard was analysed by SEM and is shown in Figure 4.22.

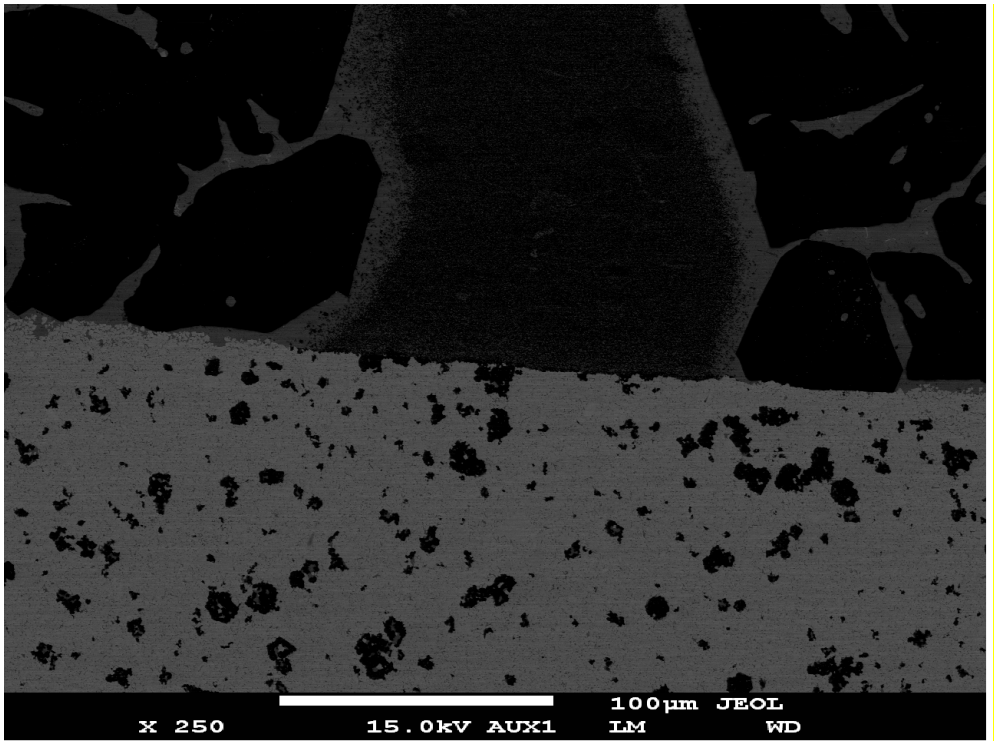


Figure 4.22: SEM of the 2µm powder pressed standard.

As with the 0.5µm powder pressed standard, light and dark spots representing localized higher or lower cobalt concentrations were also present in the 2µm powder pressed sample. An occurrence of this with a rather peculiar shape is shown in Figure 4.23.

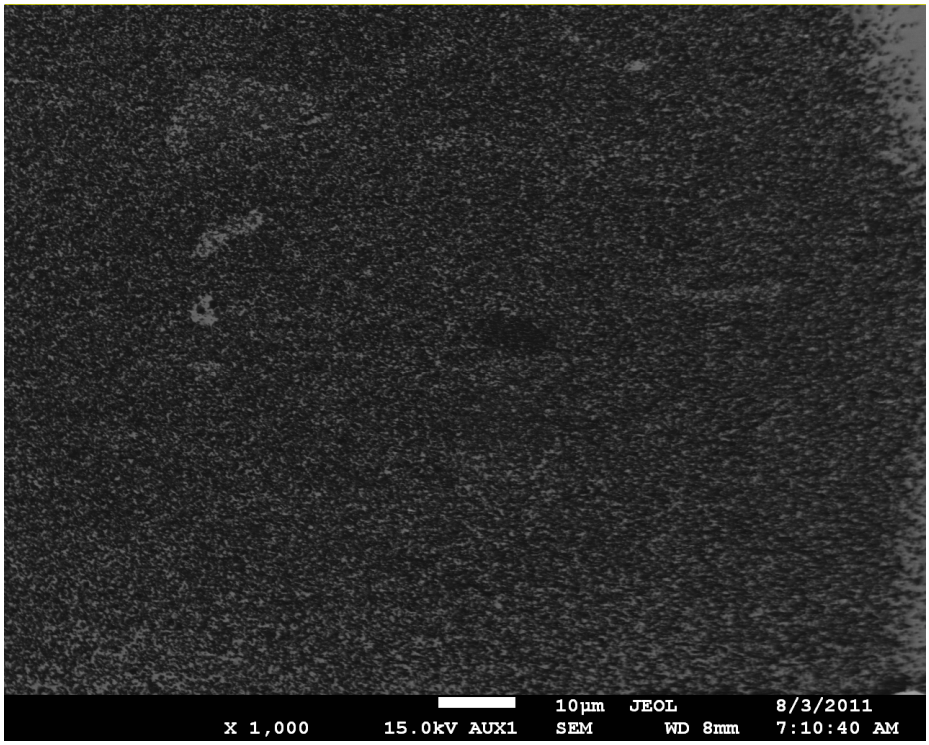


Figure 4.23: SEM showing light and dark spots in the diamond table of the 2µm powder pressed standard.

4.3.3 Deposition of laminate diamond.

Two laminate samples were made by consecutive deposition of alternating suspensions of 0.5µm and 2µm acid cleaned diamond. In both cases, the first layer was the 2µm layer. All suspension used in these experiments were at pH 8.5 and deposition was carried out on DEC substrates using an operating voltage of 1.25 V/cm. The consequent layers were made by immediately moving the electrodes from one suspension to the other after each layer. The choice of the number of layers was taken arbitrarily. The conditions of these two samples are tabulated in Table 4.8. From the table it is evident that the deposition rate has little or no dependence on the number of layers.

Table 4.8: Summary of EPD experiments of multi-layered samples deposited at pH 8.5.

Sample No.	Conc. (g/100mL)		Time (each layer) (min)	Total number of layers	Total Time (min)	Voltage (Volt/cm)	Total Deposit Weight (mg/cm^2)	Total Deposition Rate ($mg.cm^{-2}.min^{-1}$)
	0.5µm	2µm						
56	5%	10%	30	4	120	1.25	48.0	0.40
57	5%	10%	7.5	16	120	1.25	43.9	0.37

An SEM image was taken of the interface between the layers of the green state of Sample 56. The interface is shown in Figure 4.24. From the image, it is evident that the interface is relatively straight and the two layers are well bonded. No cracking was observed from the drying step.

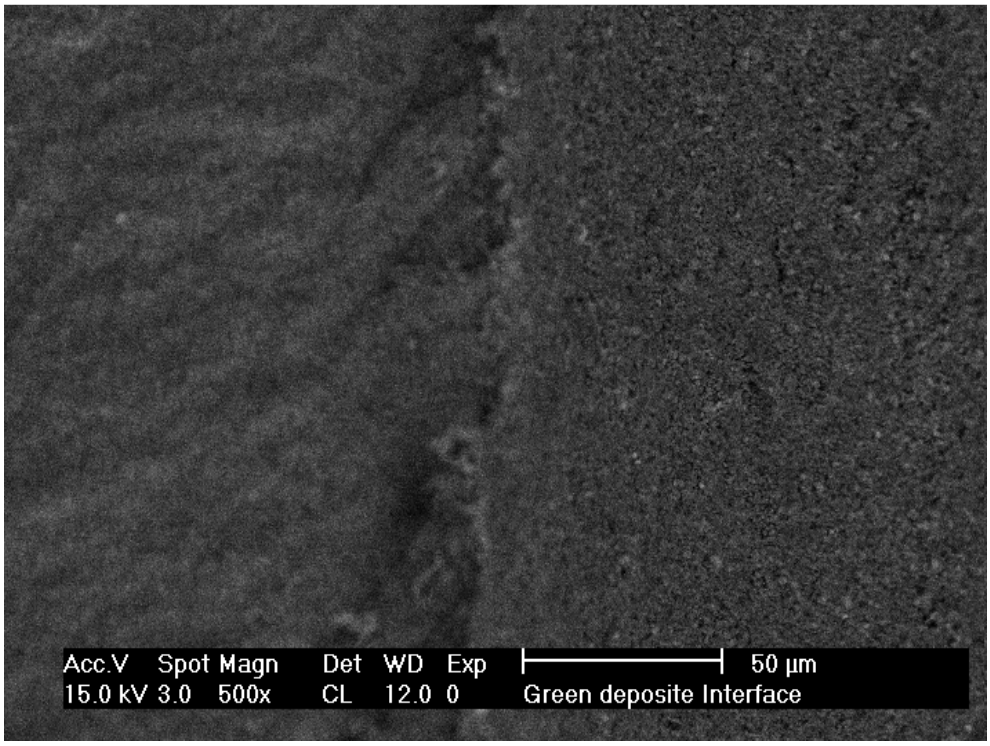


Figure 4.24: SEM micrograph of the fracture surface of the interface between a 0.5µm and a 2µm grade layer in a green deposit.

4.3.4 Sintered laminate deposit

Sample 57 was sintered. The cut and polished sample was investigated under an optical microscope (Figure 4.25). The laminate was made to have a total of 16 layers. However, upon inspection of the microscope picture, it would appear that more layers are present due to the shifting of some layers. No AGG was observed in the diamond laminate. The sintered sample had a total average thickness of 946µm.

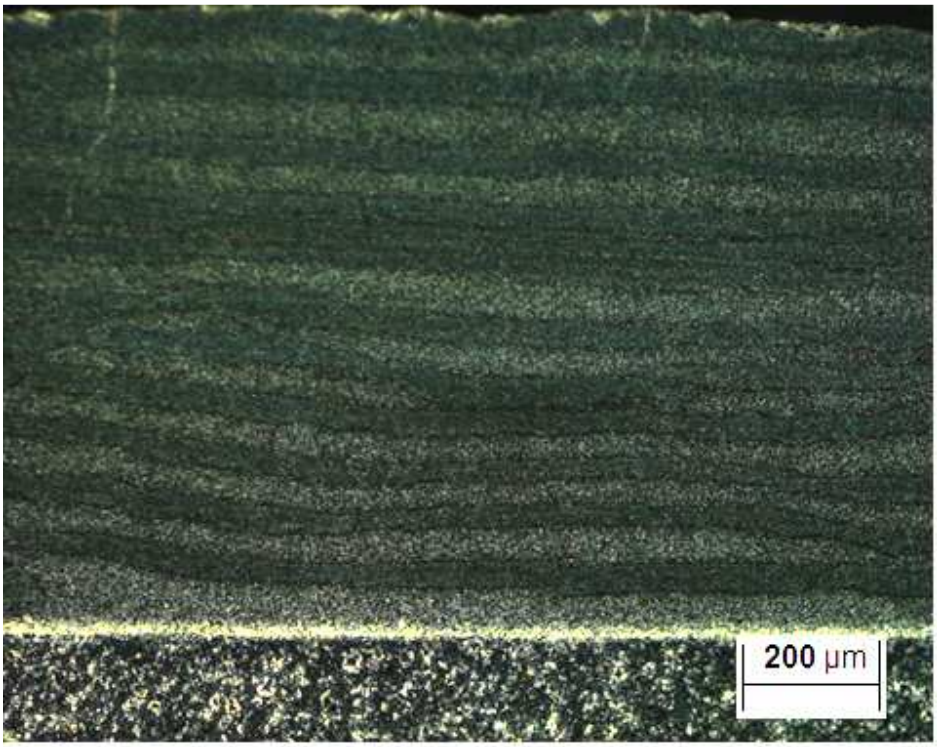


Figure 4.25: Optical microscope picture of the diamond laminate sample showing the overall structure.

The 2µm grade diamond layers appear lighter when viewed under the optical microscope and have an average thickness of 48 ± 1 µm. The 0.5µm layers appear darker and have an average thickness 40 ± 1 µm. The average thickness of the layers

was measured in an area where the layers are uniform. This area is shown in Figure 4.26. Under examination by SEM, the 0.5µm grade layers appear lighter while the 2µm grade layers appear darker. This is opposite to that observed under the light microscope. The layers appear relatively straight and uniform in thickness.

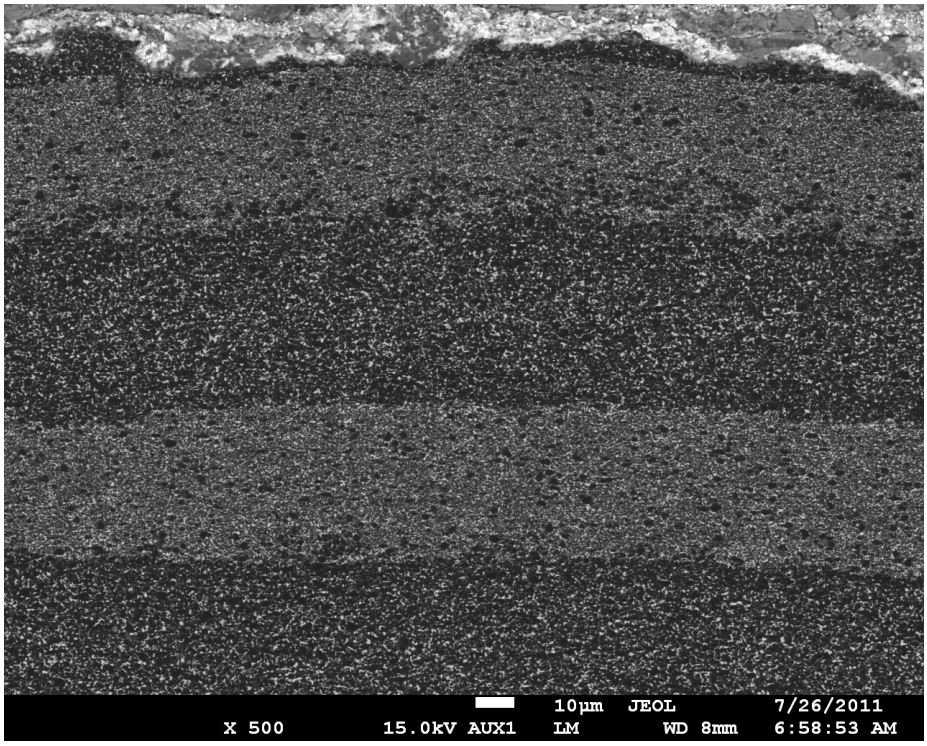


Figure 4.26: SEM micrograph of a uniform section showing the morphology of the layers.

EDS was performed on the first four layers from the carbide-diamond interface in an area where the layers were uniform. These measurements were performed to determine differences in cobalt concentrations for these layers. The scanning area was taken within the layer to be measured.

The EDS scans for layer 1 and 2 are shown in Figure 4.27. The first layer was a 2µm layer and the second layer was a 0.5µm layer.

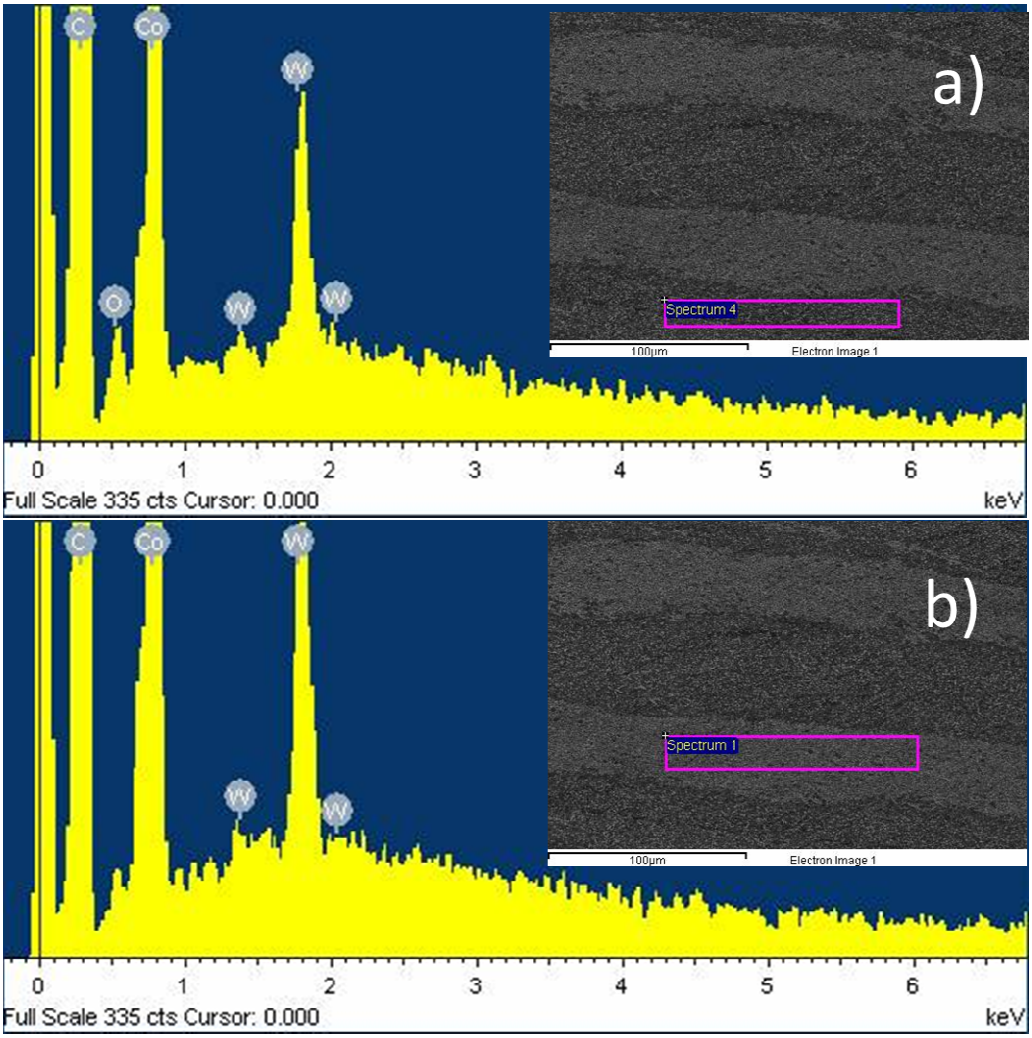


Figure 4.27: EDS scans for the first 2µm layer (a) and the first 0.5µm layer (b) of the diamond laminate sample.

The semi-quantitative results of the elemental concentration measured by EDS scan areas for of the first four layers are tabulated in Table 4.9. Oxygen content was

dismissed as an organic contaminant and the values recalculated accordingly. The 2µm grade layers contain about 16% cobalt, which is considerably less than the 0.5µm grade layers which contain about 25% cobalt. This cobalt is the residual cobalt which is left in the diamond layer after infiltration during sintering. The 2µm grade layers also have higher carbon content, at around 81% carbon as compared with the 72% for the 0.5µm grade layers. The 0.5µm grade layers have higher tungsten content. No nickel is observed in the EPD layers. This is due to the acid washing step done on the diamond prior to EPD experiments.

Table 4.9: Table showing the EDS results of the first four layers taken at a uniform area in the EPD laminate.

Element	Weight%			
	Layer 1 (2µm)	Layer 2 (0.5µm)	Layer 3 (2µm)	Layer 4 (0.5µm)
C	81	72	81	72
Co	16	25	17	25
W	2	3	2	3

The surface of the sample was analysed using lower acceleration voltages, it was discovered at that most of the surface cobalt had been pulled out during the polishing of the laminate sample. This, combined with the fact that the EDS has not been calibrated makes the EDS results questionable. Thus, the sample was ion-polished to ensure a flat surface. A comparison of the standard polished and ion-polished surface images can be seen in Figure 4.28.

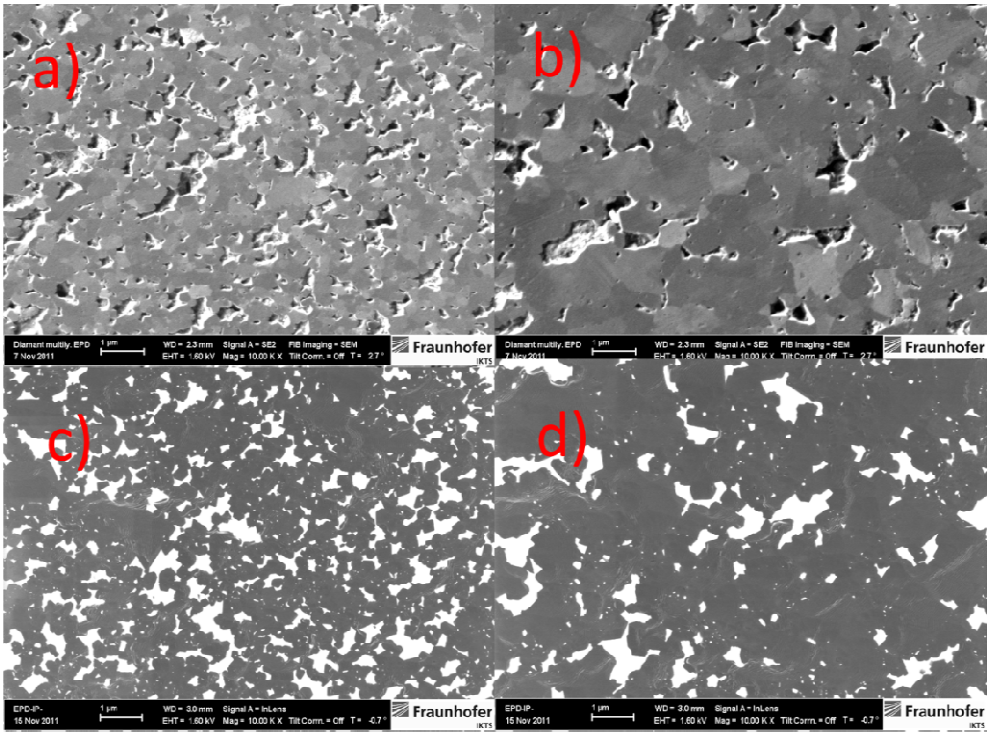


Figure 4.28: Comparison of polishing techniques: a) 0.5µm layer standard polish, b) 2µm layer standard polish, c) 0.5µm ion polish, 2µm ion polish.

SEM images were taken at low acceleration voltages the ion-polished laminate surface. By performing image analysis on the ion-polished surface, a more accurate cobalt content was determined. Image analysis works by setting colour thresholds for the different phases in the image (Figure 4.29). Thus, the black areas correspond with the diamond phase and are assigned a green colour. The white areas correspond with the WC and Co phases and are assigned a red colour. Due to the fact that both WC and Co both appear white on the image, summing their areas was necessary. However, the WC content in the PCD is typically low and therefore a valid estimation of Co content can be ascertained.

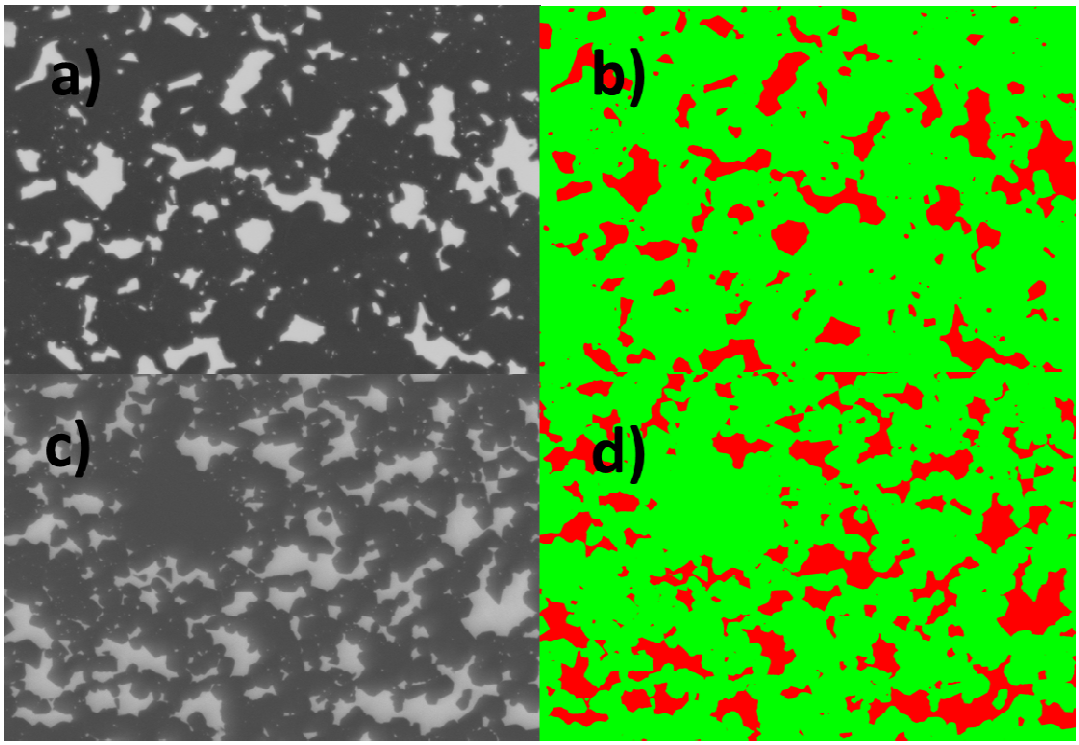


Figure 4.29: SEM Image analysis showing the phase thresh-holding for the 2µm layer in a) and b) and the 0.5µm layer in c) and d).

From Figure 4.28, it is evident that the WC and Co pools are smaller in size in the 0.5µm layer. Even though the pools are smaller in the 0.5µm layers, there are more of them, and this would translate to a higher non-diamond phase content. The 9 best images for layer 3 and 4 respectively were used for image analysis. The area of the phases was calculated for these layers, converted to weight % and reported in Table 4.10.

Table 4.10: Table showing the phase composition of layers 3 and 4 as measured by image analysis.

Element	Volume %	
	Layer 3 (2µm)	Layer 4 (0.5µm)
C	73 ± 1	61 ± 2
Co + W	27 ± 1	39 ± 2

4.3.5 Defects

Several defects were noticed with the laminate sample. The most obvious of defects are the skew and non-continuous layers. These defects are clearly visible in Figure 4.30. A large dark spot is also present to the left of the image in the centre; this is likely to be a surface artefact.

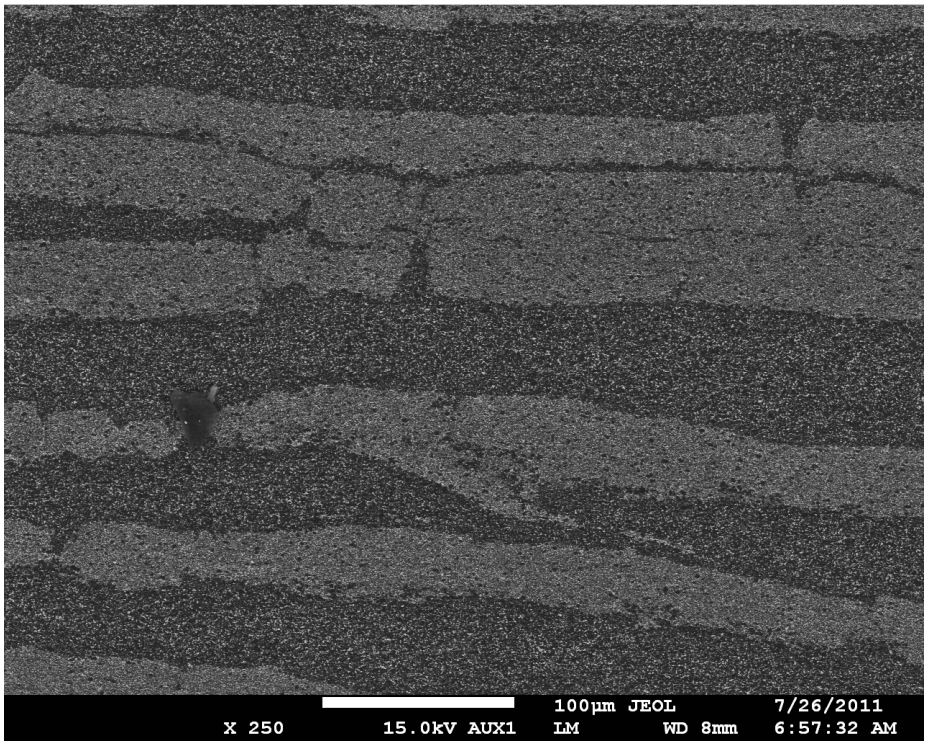


Figure 4.30: SEM micrograph of layer defects present in the diamond laminate.

Major defects were observed in the diamond layers at the edge of the sample close to the niobium canister wall. Such defects include disconnections and/or dislocations of some of the layers. These discontinuous layers can be seen in Figure 4.31

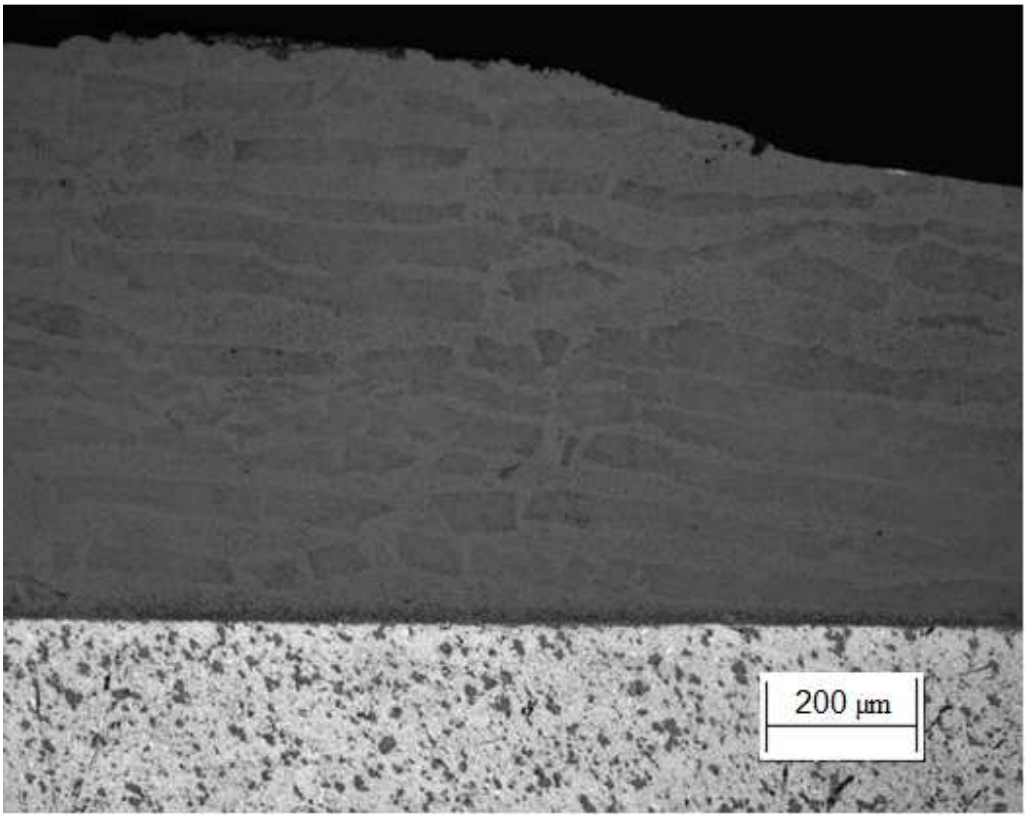


Figure 4.31: Optical microscope picture showing damage sustained at the edge of the sample.

Another defect observed is the inclusion of larger grains in the finer grade layer. This phenomenon is visible with higher magnification in Figure 4.32. These inclusions appear as dark spots in the lighter area and are distributed in a uniform manner throughout the fine grade layers.

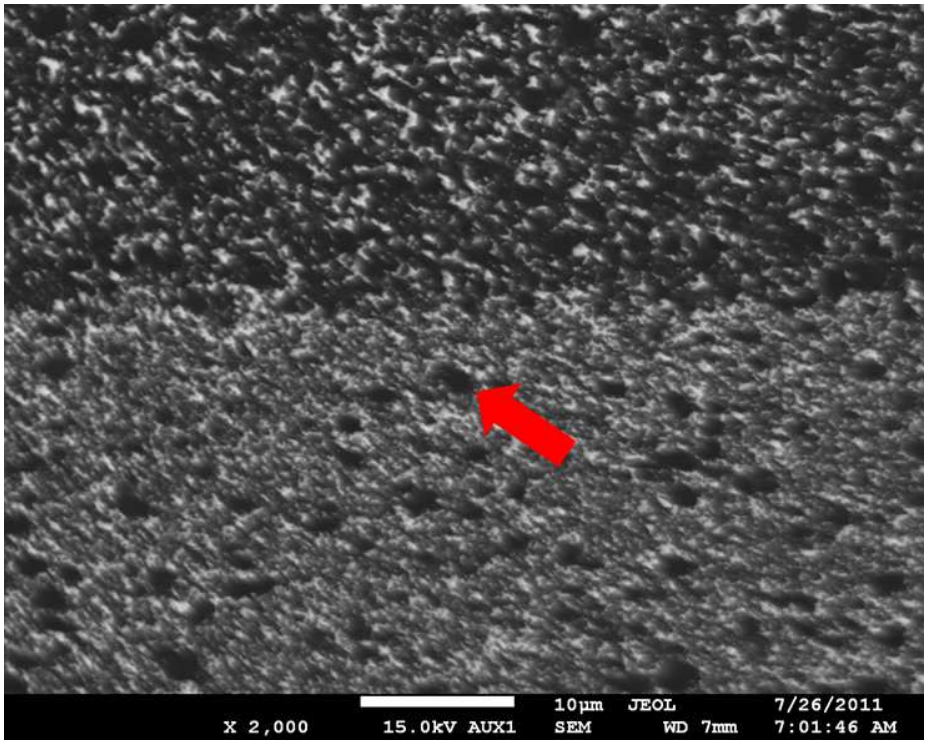


Figure 4.32: SEM showing the inclusion of larger grains in the fine grade layer.

4.3.6 Fracture of diamond laminate

The sintered diamond laminate sample was fractured using the 3-point bend jig to determine if a crack would deflect between the layers. Evidence of crack deflection would provide indication of existing residual stresses in the sintered laminate.

An optical microscope picture of the crack path can be seen in Figure 4.33. The crack was relatively straight and showed very little crack deflection. Areas where slight crack deflection was observed are highlighted red in the image. In these areas, the crack propagates straight through the 0.5µm layer (darker layer) and deflects when entering the 2µm layer (lighter layer).

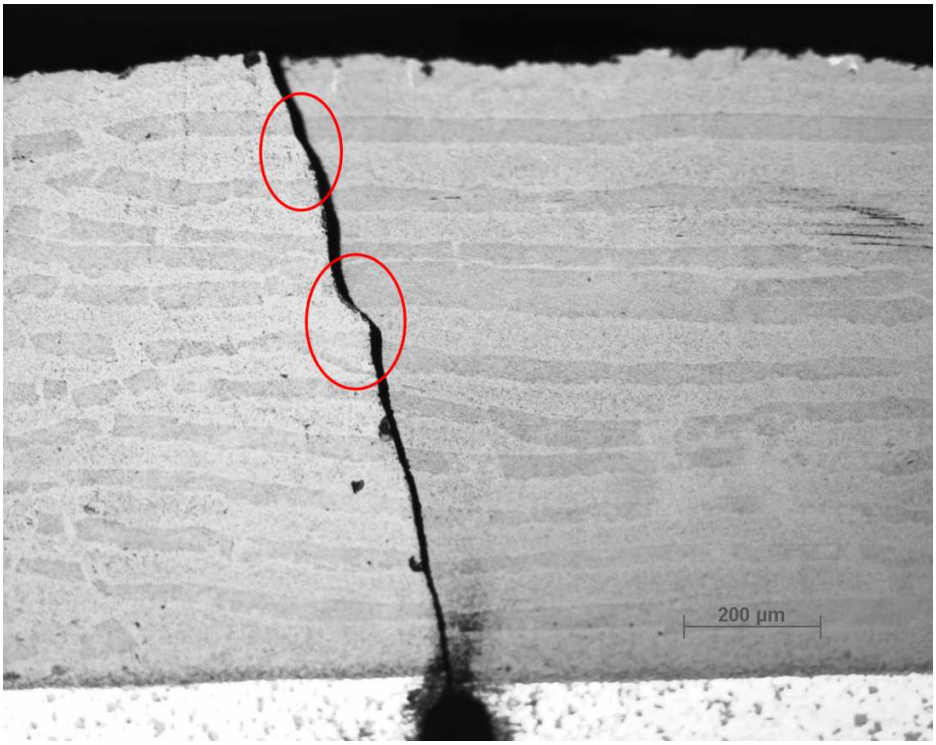


Figure 4.33: An optical microscope picture showing the direction of a forced crack path.

The load versus displacement graph as recorded by the Tinius Olsen machine for the sintered diamond laminate is shown in Figure 4.34. The graph shows does not show the characteristic fracture profile expected for laminate composites during fracture analysis.

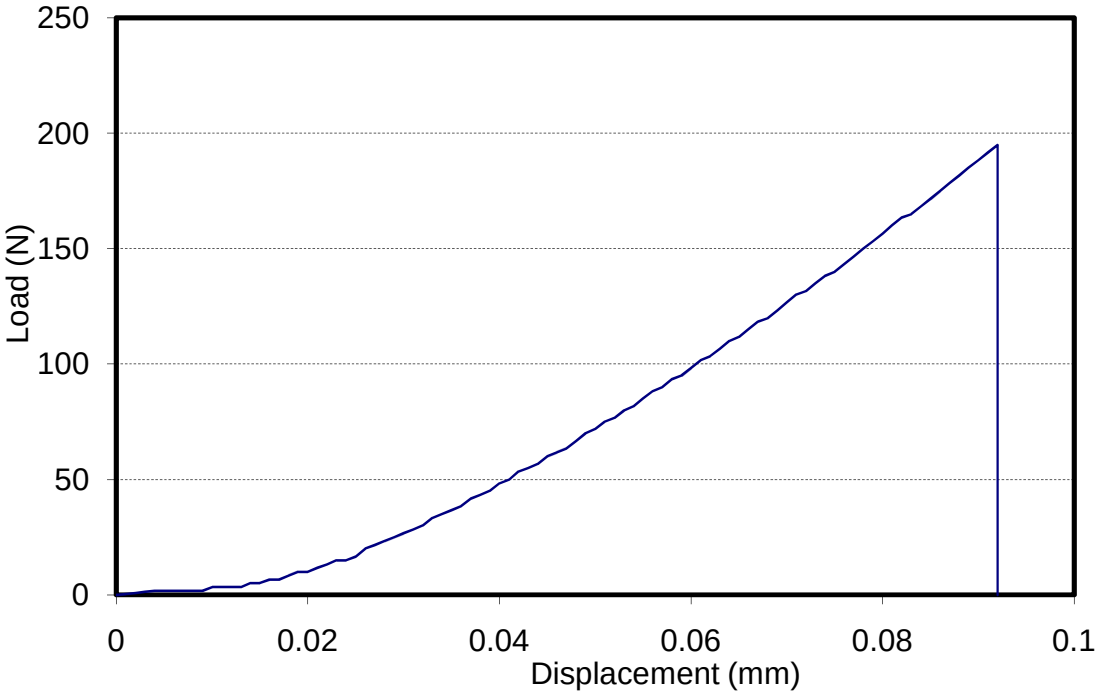


Figure 4.34: Load vs. displacement graph of the sintered diamond laminate as recorded during 3-point bend testing.

Upon closer inspection of the sintered laminate, a pre-existing crack exhibiting clear crack deflection was observed. This crack was found at the top of the sample in the last six layers close to the diamond/coated cup interface. This crack is shown in Figure 4.35. It is suspected that the crack had occurred during some point in the sintering cycle. As confirmed by EDS, the light spots in the crack are contaminants introduced during polishing. Although the crack did not deflect immediately at the interface of the two layers, it started to bend in the close vicinity of the interface thus illustrating that the residual forces did indeed have an impact on the direction of the crack path. Similar to what was observed for the controlled crack, the crack propagates straight through the 0.5µm layers (lighter layer) and deflects upon entering the 2µm layers (darker layers).

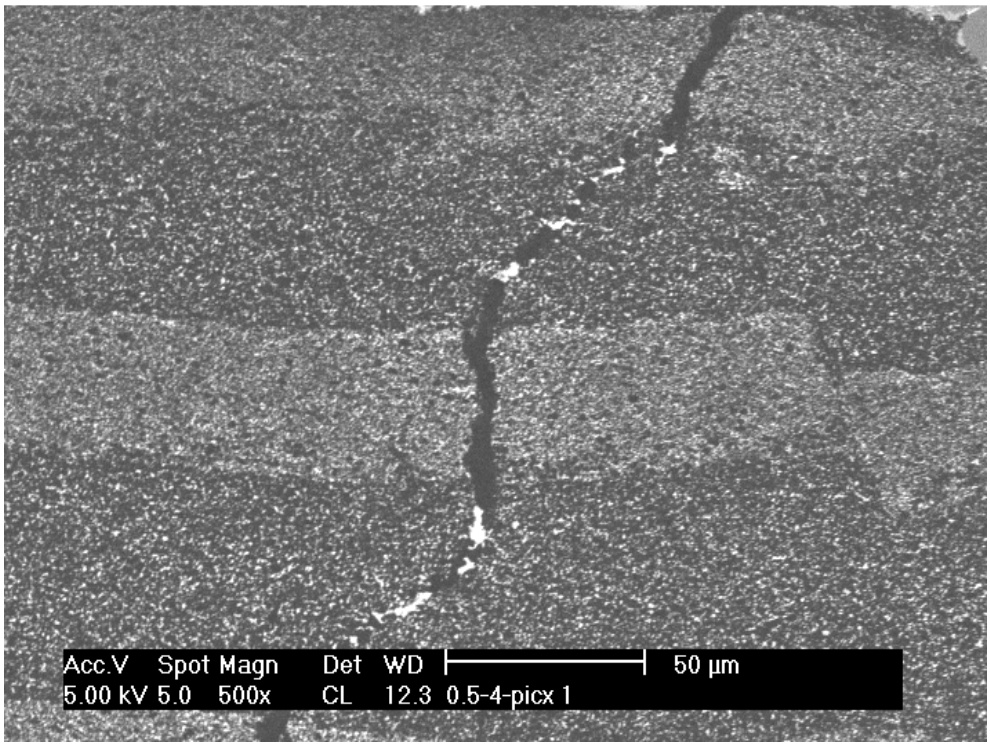


Figure 4.35: SEM micrograph of a pre-existing crack showing crack deflection in the laminate material.

5. Discussion

5.1 Introduction

This section contains a discussion of the results presented in Section 4. It is divided into two main sections. The first describes the results presented for the EPD experiments with alumina powder, and the second describes results for the EPD experiments with diamond powder.

5.2 EPD experiments with alumina powder

5.2.1 Alumina surface chemistry

The development of a surface charge on particles in an EPD setup is of utmost importance. A high surface charge will result in a more stable suspension which will resist sedimentation during the EPD process. Crucially, a high surface charge also results in improved electrophoretic mobility. With higher electrophoretic mobility, higher deposition rates are achievable during EPD.

The surface chemistry has a strong influence on the resultant charge of the particle once suspended in a liquid. The functional groups on the surface of these particles will interact with the liquid media and additives to develop the charge. Thus, study and optimization of the surface groups are fundamental to any EPD experiment.

The development of a surface charge on the particles can occur in a number of ways. These mechanisms are not exclusive and may compete with each other. Some of these mechanisms include [68]:

1. Dissolution/precipitation,
2. Selective dissolution/precipitation,

3. Selective adsorption,
4. Surface catalysis.

The mechanism for surface charge development of alumina in ethanol has been studied [68]. It was shown that the surface of the alumina particles acts as a catalyst for the dissociation of the ethanol into a hydrogen ion and an ethoxide ion. These ions are then adsorbed onto the surface of the alumina particle. Due to the fact that the ethoxide ion has a higher tendency to be desorbed from the surface than the hydrogen ion, a positive charge on the surface will result. This accounts for the positive zeta potential for alumina in the alcohol. Upon addition of HCl, the ethoxide ions react with the hydronium ion to form neutral water and ethanol. This results in the decrease of ethoxide ions on the surface and thus a higher positive charge. A schematic of this mechanism can be seen in Figure 5.1.

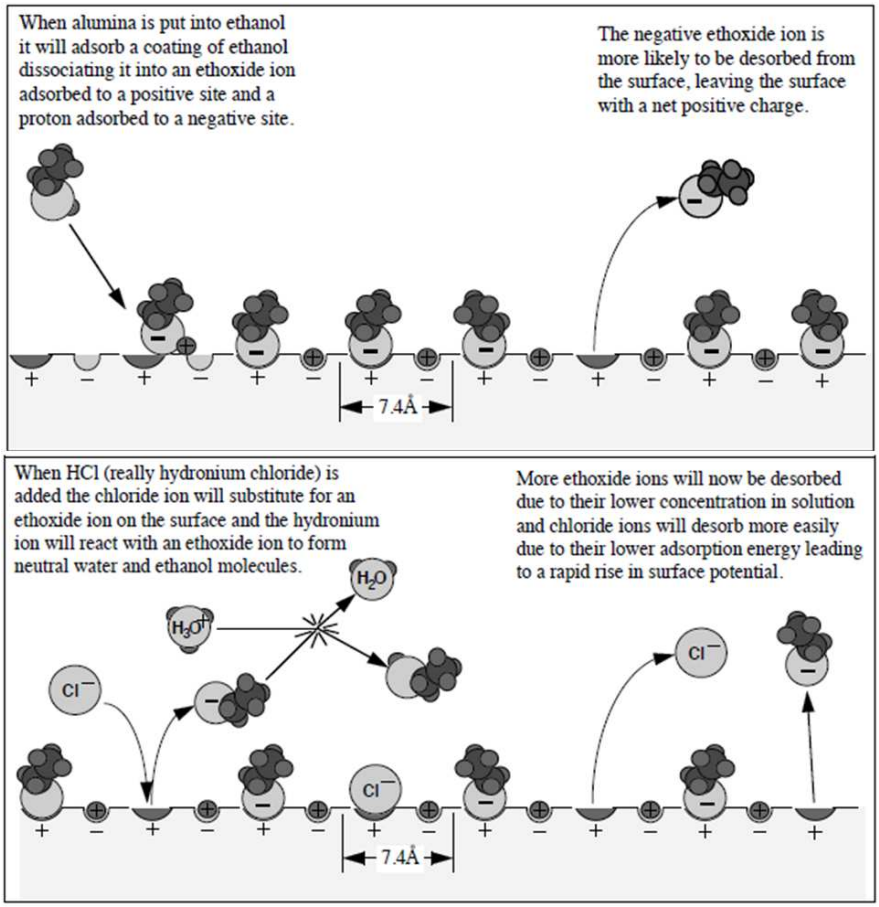


Figure 5.1: (Top) Mechanism of surface charging for alumina in ethanol. (Bottom) Effect of charged surface after the addition of HCl. [68]

Due to the fact that the properties and behaviour of ethanol and isopropanol are similar, alumina suspended in isopropanol should acquire a surface charge by the same mechanism presented. Since deposits formed only on the cathode, the surface of the alumina particle was likely to be positively charged. This observation is in agreement with the proposed mechanism of surface charging.

5.2.2 Alumina deposition

5.2.2.1 Experimental considerations

The deposition of alumina is well documented by Besra et al. [30]. In the setup, the stainless steel electrodes were masked using Teflon holders. In the experiments performed in this project; wax, plastic tape and plastic holders were used as masking agents. Deposition did not occur on the wax masking as is shown in Figure 4.1. This later proved especially important during the kinetic studies of EPD since the edges of electrodes would concentrate the electric field and result in higher deposition at the edges. It was also suspected that deposits occurring on the edges of electrodes may also have a connection with the cracking phenomenon during drying. Since deposition would also occur on the back of the working electrode, the electrodes required extensive masking, thus revealing only a controlled area for deposition. Therefore, precise control of the deposition area was essential. Drying presented a large problem due to the fact that cracks would begin to appear in thicker deposits during the drying process. This phenomenon is known to occur during drying of some green bodies due to capillary forces [28]. These forces cause the deposit to shrink as the liquid evaporates out the pores. Thus when a deposit begins to shrink on a stiff substrate, such as an electrode, large stresses may develop. These stresses are relieved by the formation of cracks. Keeping this in mind, alumina samples were made by depositing onto aluminium foil which allowed the deposit to dry on a more flexible substrate. This method proved successful in preventing the cracks as long as any deposit adhered to the masking agent was detached so that the deposit could contract freely during drying. Although the temperature was not measured during deposition, it is expected that it would rise due to the fact that there is a current flowing through the suspension.

5.2.2.2 Deposition rates and green densities

From the derived Equation 2.4-2, $w = (k)ECt$, where k is a constant, E the applied electric field, C the suspension concentration and t the time, it was clear that the weight

of the deposit should have a directly linear relationship with the three experimental parameters; voltage, time and concentration. Voltage and time were each tested while keeping the other variables constant. Deposit weight, versus both voltage and time, showed a good linear relationship with a R^2 fit of 99.1% and 99.5% respectively. The third and last variable, concentration, was not tested. This is due to the fact that creating multiple suspensions with exactly the same pH proved near impossible with organic suspensions. Measurements in alcohol cause the pH meter to give readings which do not stabilise and thus it was impossible to reach a desired pH value. The knowledge gathered during the kinetic studies, it proved rather easy to achieve close to the desired deposit weight in later experiments by simply adjusting one of the experimental variables.

The slope of deposit weight versus time in Figure 4.6 reveals the deposition rate of the EPD process. However, by interpolating the best fit trend line, it is evident that the line does not intercept through the origin as it would be expected by Equation 2.4-2. The intercept along the y-axis occurs at 3.0048 mg/cm^2. A possible explanation for this phenomenon is an electric field drop [69] and is demonstrated in Figure 5.2. This drop in voltage is caused by increasing deposit resistivity during deposition [70]. Since the thickness of the deposits in literature data was not available, a direct influence of the developing resistivity cannot be compared. Another explanation for this decrease in deposition rate over time is due to the depletion of charge carriers in the suspension [27]. To accept these explanations, the graph would have to show a continual decrease in the deposit weight over time. However, since the graph is linear and has an R^2 value of 99.5%, the cause of the y-intercept value must be due to some starting phenomenon which is not fully understood.

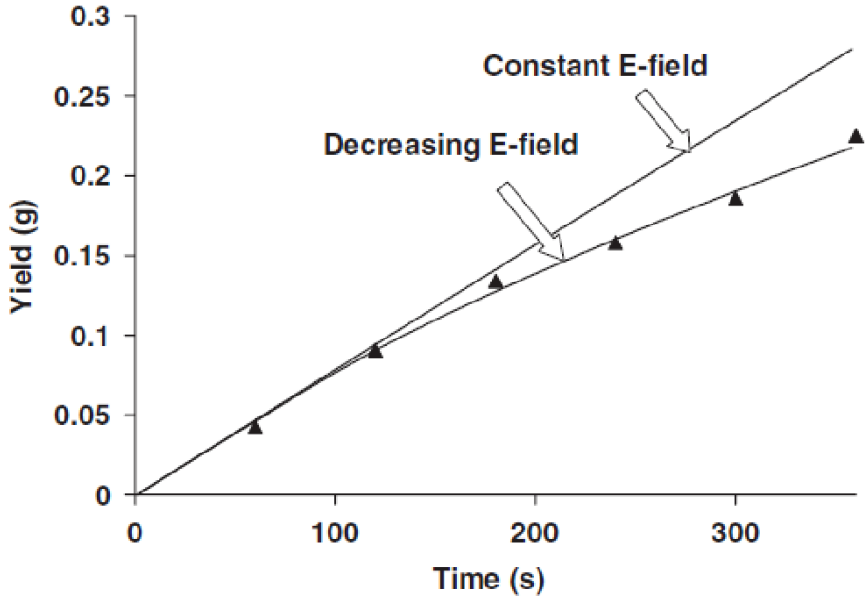


Figure 5.2: Graph showing the difference between predicted and experimental yield of deposited Al_2O_3 from ethanol-HNO_3 suspensions using a constant voltage of 42.7V/cm [69].

A possible explanation for this phenomenon could be the sudden deposition of particles at close proximity to the electrode thus creating a small depletion zone of particles which takes some time to replenish. More data points are needed for deposit weight at times below 5 minutes to fully understand this phenomenon.

A comparison of the deposition rate obtained in this work was tabulated against those obtained for alumina deposition in literature in Table 5.1. A deposition rate of a 10% (w/v) suspension made with a pH 5.0 at 100V/cm is 1.84mg/(cm^2.min). This value correlates well with the deposition rates obtained by Besra et al. [30]. Even though a higher voltage (166V/cm) and higher concentration (20.2g/100ml) was used in experiment conducted by Besra et al. [30], a lower deposition rate was achieved. This is probably due to the fact that the suspensions did not contain any additives to aid in charging of the surface. Butanol also has a dielectric constant of 17.5 which is lower than that of isopropanol which has a value of 18.3. These two factors would contribute to a lower surface charge of the particles and thus a lower deposition rate. Van der

Biest et al. [31] achieved a much higher deposition rate. The reason for this discrepancy could be due to the fact that ethanol has a higher dielectric constant of 24.3; however, it is unlikely that this change in dielectric constant could result in a deposition rate which is an order of magnitude higher than that presented in this work and that of Besra et al. [30]. Maca et al. [71] achieved even higher deposition rates in isopropanol. This is probably due to the MCAA/PVB additives which impart a much higher charge on the particles.

Table 5.1: Comparison of alumina deposition rates and green density obtained in this work and literature.

Reference	Colloidal suspension Formulation		Conc.	Voltage	Deposition Rate	Green Density
	Media	Additives	g/100mL	V/cm	mg/(cm^2.min)	% theoretical density
This work	Isopropanol	HCl (pH<5)	10	50	0.98	46
				100	1.84	45
Besra et al. [30]	Butan-1-ol	-	20.2	166	1.2	-
Van der Biest et al. [31]	Ethanol	HCl (pH<5)	10	16.5	11	53
Maca et al. [71]	Isopropanol	MCAA/PVB	13.9	30.8 (Constant current mode: 5mA)	~33-150	~58-64

Sample 42 had a green density of around 46%. This value is lower than that achieved by Van der Biest et al. [30] and Maca et al. [71] but is still within a reasonable range for a green body prepared without applied pressure. Besra et al. [28] suggest that since the EPD of a particulate film is a kinetic phenomenon, the rate of accumulation of these particles will ultimately affect their packing behaviour. Thus particles deposited with a

higher driving force are more likely to be influenced by disturbances in the suspension media. Such disturbances can arise from flow patterns due to stirring of the suspension or perhaps sedimentation of the particles. In these papers, it is also mentioned that at higher voltages, particles do not have enough time to find the optimal packing position since the higher driving force may reduce lateral movement of particles as they deposit.

As a general guideline, Basu et al. [72] state that moderate voltages of between 25-100V/cm result in more uniform deposits than those with voltages of greater than 100V/cm. Since both Sample 41 and 42 were made with voltages within this recommended range, both were relatively uniform. However Sample 42, which was made using a lower voltage had a slightly better surface morphology. It is also important to note that previous samples made with voltages of 175-200V/cm had a highly irregular surface morphology.

5.2.3 Alumina sintering

Sample 41, which was made with a higher voltage, had a slightly higher overall density of 99.1%. However, it also had a higher open porosity of 0.81%. Whereas, Sample 42 which was made with a lower voltage had a lower overall density of 98.9% as well as a lower open porosity of 0.46%.

Krell and Blank [73] have clarified that homogeneity of packing allows better densification of a ceramic during sintering despite the fact that it may have a lower green density. This is evident in Figure 5.3 where gel casted green bodies show the highest densification at the lowest temperature.

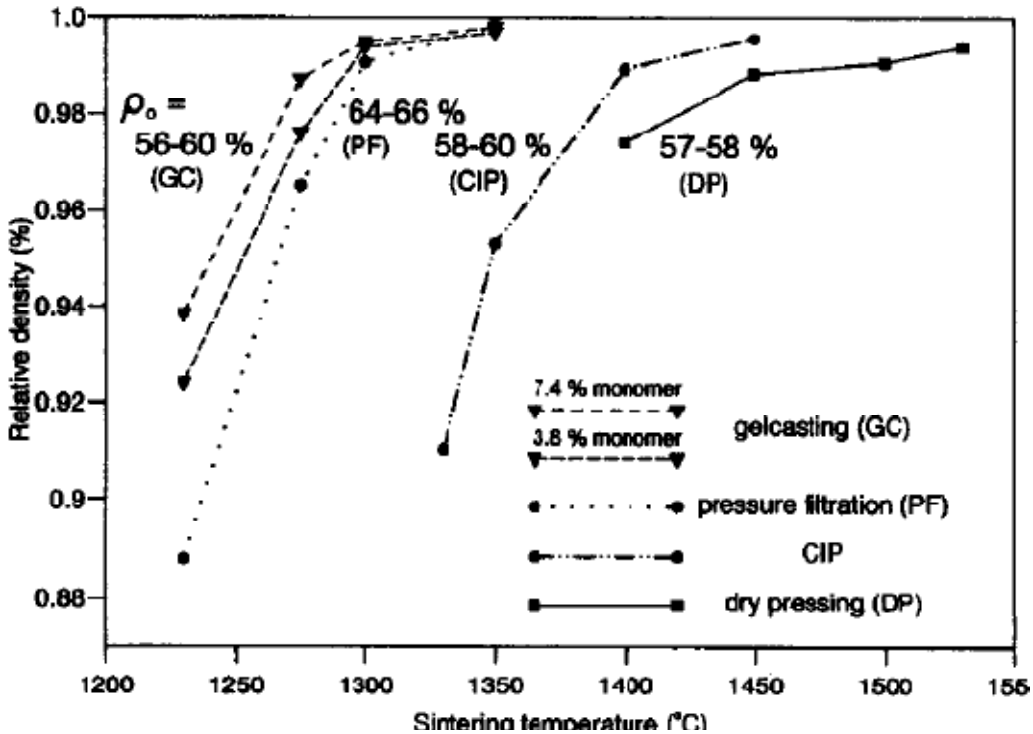


Figure 5.3: Effect of the shaping method and green density on the temperature effect on isothermal sintering for the same alumina powder [73].

Due to the fact that both EPD alumina samples had such high densities after pressure-less sintering without the use of any sintering aids, such as magnesium oxide, it can be concluded that the samples made by EPD had highly homogenous packing.

5.3 EPD experiments with diamond powders

5.3.1 Diamond surface chemistry

In contrast to the surface of alumina, the surface chemistry of diamond is a little more complicated due to the many surface groups available on diamond. Shergold and

Hartley [66] suggest that the primary groups found on the surface of diamond are a combination of epoxide, carbonyl, carboxyl and hydroxyl groups (Figure 5.4) as well as saturated and unsaturated hydrocarbons. Reactive unsaturated covalent bonds present on the diamond give rise to its rich surface chemistry. These bonds react with water and oxygen to form a number of oxygen containing surface groups [66]. Thus the charge developed on the surface of these particles upon immersion in a liquid are due to ionization of these groups in addition to selective ion adsorption from the solution [74].

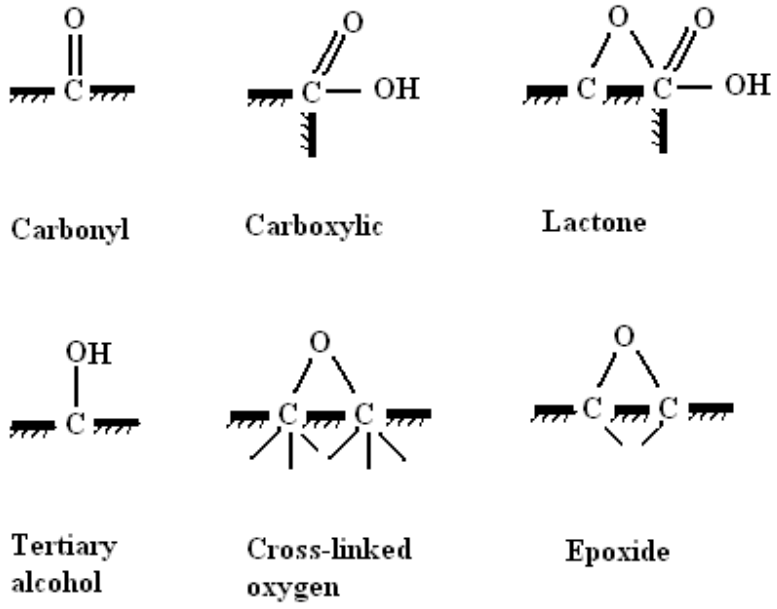


Figure 5.4: Some of the possible surface groups on diamond [66].

In order to achieve successful electrophoretic deposition, particles must obtain maximum charge. In polar solvents such as alcohols and water, polar groups on the surface of the diamond must dominate in order to achieve stable suspensions.

Non-polar groups such as the plain hydrocarbon groups aid in giving the diamond non-polar character. The ratio of polar and non-polar groups that exist on the diamond will decide its hydrophobicity. For our purposes, it was necessary to have the polar groups dominate so that the diamond exhibits stable behaviour in polar suspension media such as water or alcohols.

Due to the relatively strong –OH and –COOH bands at 3250cm^{-1} and 1600cm^{-1} respectively, it is suggested that these two groups are the dominant ionic groups on the surface of the diamond.

The –COOH group is mildly acidic and will deprotonate according to Equation 5.3-1.

$$-COOH + OH^- \rightarrow -COO^- + H_2O$$ **Equation 5.3-1**

In strongly acidic environments, the –OH groups will protonate according to Equation 5.3-2.

$$-OH + H^+ \rightarrow -OH_2^+$$ **Equation 5.3-2**

The zeta-potential curves for the acid washed powder in Figure 4.12 had an isoelectric point (IEP) at pH 2.7. At this pH, the particles have zero charge on them and the suspension of particles will collapse due to the lack of electrostatic forces between the particles. At a pH below 2.7, it is possible that the –OH groups protonate by Equation 5.2-2 to give the diamond particles a small positive charge. The adsorption of hydrogen ions on the diamond surface may also contribute to the positive charge at low pH. At pH above 2.7, the deprotonation of –COOH groups may give the diamond a negative charge by Equation 5.2-1. By using this mechanism, as the pH moves to higher value, more and more –COOH groups would deprotonate resulting in a more negative charge on the particle. The adsorption of hydroxide ions to the surface of the diamond may also contribute to its gradual increase in negative charge in increasingly alkaline environments. This behaviour gives the diamond the characteristic zeta-potential curve that was observed in Figure 4.12.

By observing the zeta potential plots for diamond in water, a working pH of 8.5 was selected for all aqueous suspensions for EPD. The reason for this choice was due to the fact that the zeta-potential achieves maximum value with the minimum amount of base addition. Achieving maximum surface charge with the minimum amount of ionic additives is important because it maintains a low conductivity of the suspension. When the conductivity of the suspension is low, more current is carried by the suspended particles migrating in the electric field between the electrodes and thus faster deposition rates are achievable. A pH of 8.5 was also desirable due to the fact that zeta-potential values are stable for pH ranges either side of this value. Thus, slight fluctuations in pH would still result in the same zeta-potential and this would help make experiments more reproducible.

Very little information exists on the zeta-potential studies of diamond suspensions, therefore an accurate comparison with literature data proved difficult; however, in a study on the effects of sodium oleate on the aqueous dispersion of detonation-synthesized diamond, Xu et al. [75] reveals a zeta-potential vs. pH plot for the detonated nano-diamond. The diamond powders were also washed with acids to remove metal impurities. The zeta-potential plot is shown in Figure 5.5. Curve a) corresponds with nano-diamond powder treated only with perchloric acid to remove atramentous impurities. Thus the powder in curve a) is the closest match to the diamond powder used in this work. The detonated powder suspension used by Xu et al. [75] has an isoelectric point at pH 4.3, which is at a less acidic position than the diamond used in this experiment. This may be as a result of the different surface chemistry on their diamond due to the detonation synthesis process which introduces additional $–NH_2$ groups. In a similar fashion to –OH groups, $–NH_2$ groups would protonate in the presence of acids to form $–NH_3^+$ thus leading to more a positive character in acidic environments. It is also of note that curve a) reaches a maximum negative zeta-potential of around -20mV which is significantly lower than the maximum used in this project (around -50mV). The sodium oleate treated powder does

however achieve a maximum zeta potential of around -50mV at pH 8.5 which corresponds well with the results obtained in this experiment.

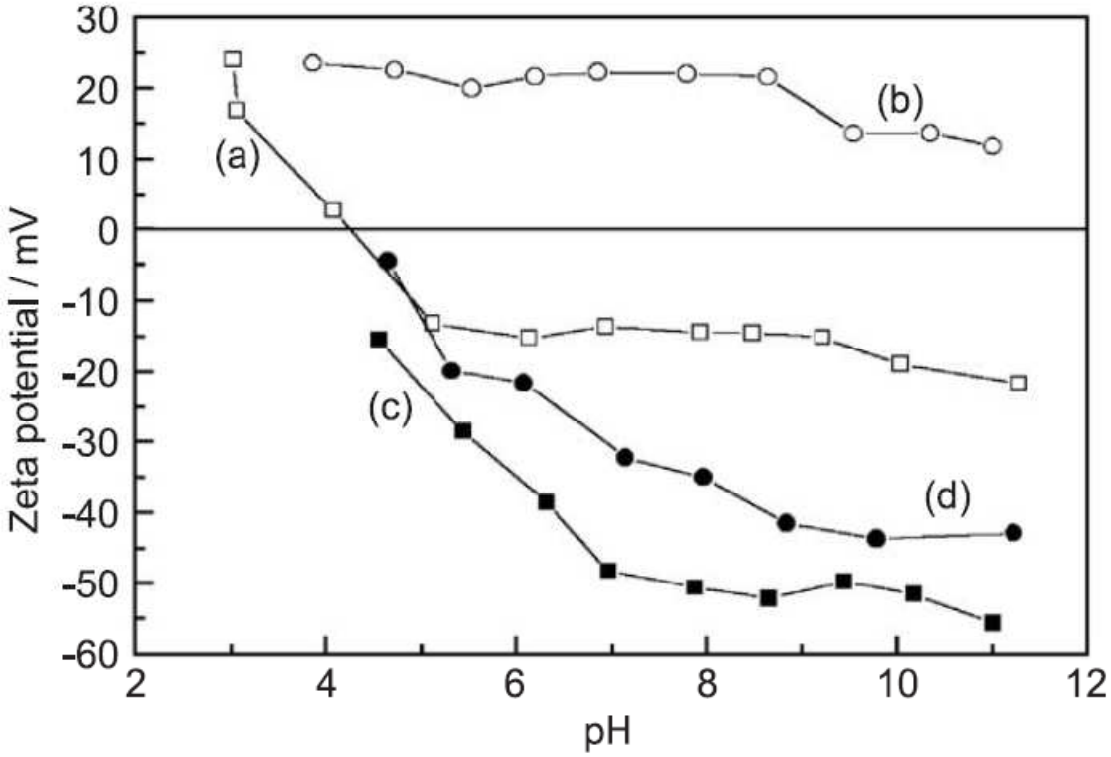


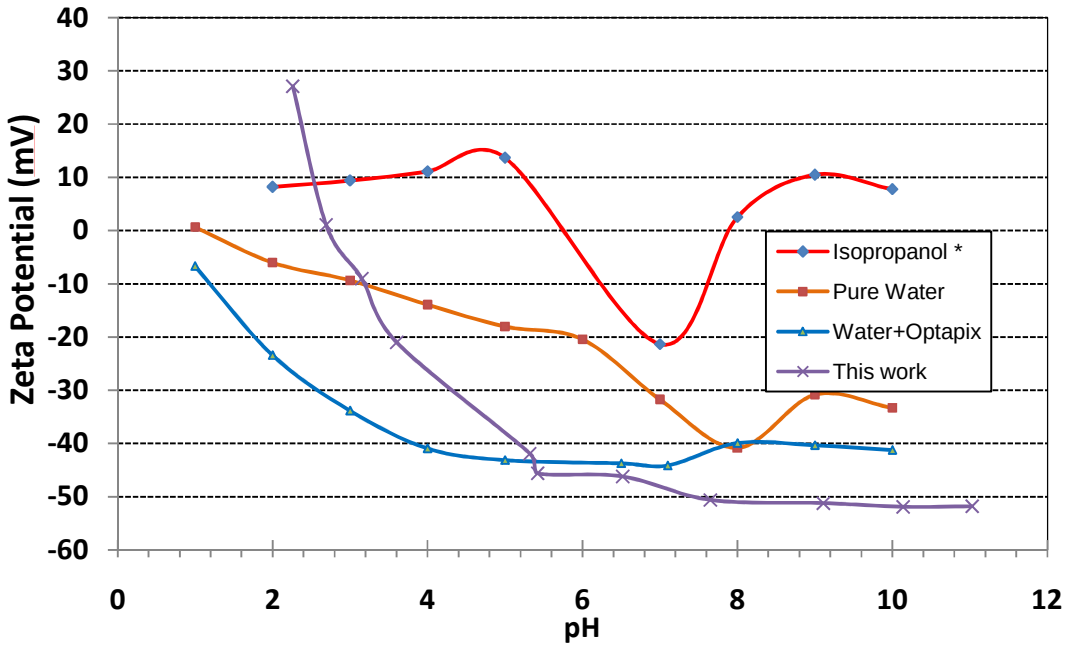
Figure 5.5: Zeta-potential vs. pH plot for detonated nano-diamond treated with: a) perchloric acid; b) sulphuric acid and potassium permanganate; c) perchloric acid and 10^{-3} mol.dm^{-3} sodium oleate; d) sulphuric acid, potassium permanganate and 10^{-3} mol.dm^{-3} sodium oleate [75].

Organic suspensions are usually the preferred choice for EPD due to the fact that alcohols do not hydrolyse at higher voltages. Therefore, high voltages may be used during EPD and this, in principal, would allow faster deposition times.

Zeta potential measurements proved to be valuable in helping to understand the behaviour of the diamond in suspension beyond the limited understanding provided by

the FTIR results. From Figure 4.11, it became evident that diamond suspensions made in isopropanol required the suspension to be aged for at least an hour before use due to the fact that the zeta potential increases over time. The reason for this is unknown; however the adsorption of hydrogen ions or other cations at the isopropanol-particle interface is likely.

Due to the limits of the scope of this project, binder studies for diamond did not form part of this research. However, under the supervision of the author, the effects of polymer binder Optapix 112 on 0.5µm acid washed diamond powder were performed by Masilela [76]. A zeta-potential versus pH plot for acid washed diamond in water and acid washed diamond in water with 1 wt% Optapix is shown in Figure 5.6. Despite the fact that the zeta-potential for the acid washed powder is lower than that observed in Figure 4.12, the addition of Optapix binder in this case increased the maximum surface charge by about 5mV. The binder also increased the zeta potentials over a wider range of pH values. This could be attributed to increased electrostatic repulsions between the particles. In Masilela's paper [76], stronger and more adherent deposits are also claimed.



** apparent pH*

Figure 5.6: The effects of Optapix polymer binder on the zeta-potential of 0.5µm acid washed diamond in water [76]

Attempts to stabilize the suspension of diamond particles in organic media were unsuccessful. Since the dielectric constant of isopropanol is lower than that of water, particles acquire a weaker charge when suspended in the alcohol. Control of the pH in isopropanol media also proved to be difficult, and unexpected results were often encountered as seen in Figure 5.6.

Attempts at trying to replicate isopropanol suspensions using the iodine, acetone and water method [36] did not yield a stable suspension either. The suspension became very hot to the touch during EPD thus indicating that the suspension had a high ionic strength because of the additives. Another reason may be due to the fact that the diamond powder used in literature was different to the powder used in this project. Because of varying amounts of metal impurities and the vast combinations of surface

groups possible, two batches of a diamond powder even from the same supplier, may differ and thus behave differently in suspension.

5.3.2 Diamond deposition

5.3.2.1 Experimental considerations

In earlier work, Panitz et al. [77] described the EPD of diamond particles smaller than 3µm. In this work, some of the limitations for the EPD of diamond are listed. The first and most interesting limitation mentioned in this literature is that water-based electrophoretic baths produce rough, irregular and poor quality coatings, due mostly to gas formation at the electrode. As one of the biggest limitations of aqueous EPD, it is well known that water will undergo electrolysis at voltages above 5V [25]. The diamond deposits in this project were made with a working voltage of 1.5V. During the time of deposition, the suspension remained stable with relatively little sedimentation. No bubble formation was observed. Thus the work in this project shows that the EPD of diamond in water can be achieved with few problems by using voltages below the threshold the voltage required for disassociation.

By observing the first diamond deposit obtained in Figure 4.13, it is evident that the deposit around the edges of the carbide disc was much thicker than that in the centre of the disc. This is due to the fact that edges concentrate the electric field. This feature of the current diamond EPD technology is unavoidable and is mentioned in the work by Panitz et al. [77]. One possible solution to this problem might include deposition onto a larger, flat and smooth substrate and then lightly machining the edges of the deposit so as to remove the ridges around the edge and thus make it fit into the capsule assembly for sintering. However, the diamond deposit was far too brittle to allow one to handle it and transfer it from the bigger substrate to the smaller one. As discussed previously,

the use of a water soluble polymer binder such as Optapix 112 may help improve the strength of the green deposits and thus allow the deposit to be handled.

Panitz et al. [77] also mention that diamond particles in the deposit are held together by hook-and-claw adhesion as well as Van der Waal's forces. With this in mind, the overall thickness of the deposit is limited by the cohesive strength of the deposit. When the weight of the deposit is larger than the cohesive forces within the deposit, the coating may begin to sag. Panitz et al. [77] state that deposits thicker than 250µm are likely to cause poor quality coatings. Usable deposits up to an approximate thickness of 1000µm were made in this project.

5.3.2.2 Deposition rates and green densities

Even though such a low voltage was used for EPD of diamond in aqueous media, reasonable deposition rates were achievable due to the fact that such a high surface charge was present on the diamond at pH 8.5. Deposition rates of 0.10 to 0.45mg/(cm^2.min) were achieved. This deposition rate is considerably lower (an order of magnitude) than that found for alumina and this may be attributed to the fact that alumina is a more polar molecule thus acquiring higher charge. A comparison of diamond deposition rates with literature is shown in Table 5.2. The deposition rate in this project is about two orders of magnitude lower than that achieved by Zhitomirsky [36]. This large discrepancy could be attributed to the much higher voltages that can be used in the alcohol EPD setup of used in the literature.

The deposition rate of the two multilayer experiments yield similar results. However, when the multi-layered rates are compared with the monolayer rates, a small but noticeable difference is observed. Considering that if an even number or alternating layers are used, it is expected that the multi-layer sample's deposition rate would be the average of the either of its single components. However, the multi-layered deposits show a higher deposition rate than either of the respective monolayer deposits. Thus, increasing the amount of times the electrodes are dipped into the suspension results in

a higher deposition rate. This phenomenon was also observed by Fischer et al. [26]. The literature doesn't give a reason for this increase in deposition rate. The increase may be connected with the starting effect seen for the deposition of alumina in Section 5.2.2.2. By taking into account that during the deposition of multi-layered deposits, the impact of the starting effect could be amplified with each subsequent layer deposited.

Table 5.2: Comparison of monolayer and multilayer diamond deposition rates with literature.

Reference	Deposited Material	Concentration (g/100ml)	Voltage (V/cm)	Suspension Formulation		Deposition Rate ($mg.cm^{-2}.min^{-1}$)	Green Density % TD
				Media	Additives		
This work	0.5µm diamond (monolayer)	5	1.25	Water	NaOH	0.34	48
This work	2µm diamond (monolayer)	10	1.25	Water	NaOH	0.29	47
This work	Diamond laminate (4layers)	5 (0.5µm) 10 (2µm)	1.25	Water	NaOH	0.40	-
This work	Diamond laminate (16 layers)	5 (0.5µm) 10 (2µm)	1.25	Water	NaOH	0.37	-
Zhitomirsky [36]	3-6µm diamond (monolayer)	3.35	200	Isopropanol	Iodine, Water, Acetone	~24	-

The green densities of the diamond deposits (48% for the 0.5µm diamond and 47% for the 2µm diamond) are consistent with the green density found for the alumina sample (46%). No mention of diamond EPD green density figures can be found in literature, this may be due to the difficulty of obtaining accurate measurements. As is evident in dry powder packing, Panitz et al. [77] suggest that increasing the distribution of particle size in the suspension may lead to an increased green density in the deposit. By inspecting the particle packing of the 2µm grade green deposit in Figure 4.15, it is evident that the particles showed a very well packed homogenous structure. The SEM

image of the green laminate in Figure 4.24 showed good packing. Therefore it can be said that the powder was well dispersed and particles migrated individually towards the electrode.

Although only limited experiments were possible in the scope of the project, the experiments summarised in Table 4.6 show that there is a general relationship between the three variables (time, voltage and concentration) and weight of the deposit. Suspensions with higher concentrations lead to deposits with higher mass provided the other variables stay constant. Similarly, increases in voltage result in faster deposition.

Sample 48, made from 0.5µm diamond and sample 53, made from a 2 µm powder, had similar deposition rates even though the concentration used to make sample 53 was more than double sample 48. Thus it can be said that suspensions made from 0.5µm diamond has a faster deposition rate than suspensions made from 2µm diamond. This is in line with the data collected by Yuan et al. [78] who found that the electrophoretic mobility of gold nano-particles were inversely proportional to the particle size.

A particle in suspension acquires a double layer due to the developed surface charge. During deposition, the electric field causes the charged particles to accelerate from a net-zero speed. The viscosity of the liquid causes a retardation force on the particle in a direction opposite the movement and causes it to move at a terminal velocity. Thus changes in the velocity of the particle can only be brought about by changes in the forces acting on the particle. The viscous retardation force, which is characterized by Stoke's law, is directly proportional to the size of the particle [79]. Thus larger particles, by virtue of their greater retardation force, will move at a slower velocity. Since electrophoretic mobility is a function of the charge to size ratio, decreasing the particle size should result in higher mobility. However, much dispute exists in literature regarding the relationship of electrophoretic mobility and particle size. Abdoli et al. [80] determined that the deposition rate of nano-aluminium nitride powder was lower than the micro-sized powder. This was thought to be due to the fact

that smaller particles, because of their higher surface area, attain a higher electrolyte concentration around the particle and this causes a drop in the zeta-potential. Similar results were found with Hyam et al. [81] who studied the effects of ball milling on the electrophoretic behaviour of boron particles.

5.3.3 Sintered diamond

5.3.3.1 Sintering of monolithic diamond deposits

The sintering of the first batch of diamond EPD samples yielded materials that had AGG present. A summary of the samples and whether AGG had occurred is presented in Table 5.3.

Table 5.3: Summary of the various sintering experiments performed and whether AGG resulted.

Sample	Substrate	Cup	AGG present
48	WC-13% Co	Standard Cup	Yes
49	WC-13% Co	Standard Cup	Yes
50	DEC	Standard Cup	Yes
51	DEC	Standard Cup	Yes
52	DEC	Standard Cup	Yes
0.5 micron powder pressed STD	DEC	Al2O3 Coated Cup	Yes
2 micron powder pressed STD	DEC	Standard Cup	Yes
Laminate sample	DEC	Al2O3 Coated Cup	No

Sample 48 contained AGG throughout the entire sample as is evident in Figure 4.16. This sample probably had abnormal grain growth that propagated from the WC-Co as well as the niobium cup interface. Sample 49 in Figure 4.17 only suffered from AGG in a small area. The reason for this is probably due to the fact that this sample

experienced uneven heating during the temperature ramp-up stage. Thus portions of the sample that experienced cooler temperatures did not sinter to completion. The reason for this is unknown, however this is known to occur occasionally in industry and these samples are simply discarded as defects. For Samples 50; 51 and 52, DEC substrates were used. The DEC substrate is known to control abnormal grain growth at the diamond-carbide interface by increasing the carbon concentration in the cobalt melt [48]. The micrographs of Sample 50 in Figure 4.18 suggest that the abnormal grain growth had occurred from the niobium-diamond interface and had progressed downwards due to the fact that AGG at the niobium-diamond interface is continuous while AGG at the WC-diamond interface is discontinuous. Therefore, the DEC substrates proved to be effective in controlling AGG at the diamond interface. This however posed the problem of AGG occurring at the niobium-diamond interface. This problem was solved by using niobium cups that are coated on the inner surface with alumina. These coated cups are hypothesized to supress AGG at the niobium-diamond interface since alumina is a stable carbide and will not react with the diamond and the cobalt.

The micrographs of Sample 51 in Figure 4.19 suggest that the effect of the grain growth from the niobium-diamond interface was more pronounced in these samples than in sample 50 due to the fact these samples were much thinner and thus the AGG was able to progress throughout the entire diamond table. It is also suggested that the AGG had started at the niobium-diamond interface and had progressed downward through the entire sample.

5.3.3.2 Comparison with powder pressed standards

Both of the powder pressed standards suffered from AGG. This phenomenon is known to occur in monomodal fine grade samples made by the traditional powder pressing technology [51]. It is known that the embedded diamond in the carbide substrate helps

supress AGG by increasing the diamond content in the infiltrating cobalt at the interface. [48]

Despite efforts such as DEC substrates and coated cups, the 0.5µm standard shown in Figure 4.20 still suffered from AGG. It is thought that this is due to the inefficient packing of the diamond particles. The light and dark spots occurring in the non-AGG area of the 0.5µm standard in Figure 4.21 correspond with areas that have higher or lower cobalt content as compared with that of the general bulk. It is suspected that these spots occur with monomodal powder in specific areas where packing of the diamond powder before sintering was not homogenous. Thus a spot lighter than the bulk corresponds with an area where the packing of the powder was less dense and thus more of the infiltrating cobalt occupied this space. The converse phenomenon is expected for the darker spots where the density of the localised packing of the powder was higher than the bulk. These spots were also present in the 2µm standard as is visible in Figure 4.23 and it is thought that they had occurred due to the same reasons.

5.3.3.3 Sintered diamond laminate

By examining the diamond laminate after HPHT treatment (Figure 4.25), it is possible to see that the diamond laminate was properly sintered. The AGG that was present in the powder pressed standards was not observed with the diamond laminate. The reason for this is due to the fact that the 2µm particles were deposited as the first layer and served to buffer the 0.5µm layer from the area directly in contact with the substrate. Thus, by the time the cobalt had infiltrated through the first 2µm layer and reached the 0.5µm layer, it would be sufficiently saturated with dissolved carbon to prevent the abnormal growth of diamond grains. The spots seen in the powder pressed standards were not observed in the sintered EPD sample. This is because the EPD technique allows a more homogenous packing of particles as compared to dry powder pressing [82]. Thus, because of the homogenous particle packing of the EPD process, localized areas of different density within a layer were not observed.

The sintered laminate had coarse layers with an average thickness of 48 ± 1 µm, and fine layers having an average thickness of 40 ± 1 µm. Closer control could possibly be achieved by adjusting the time of deposition for one of the layers.

The ion-beam polishing of the sample before SEM for image analysis ensured a flat surface for the electron beam. Since the cobalt pools remained intact after ion-beam polishing, a more accurate determination of non-diamond phase was possible. EDS and image analysis results are compared in

Table 5.4. Since WC and Co were indistinguishable during image analysis, they were added together and the sum was reported. As is known in diamond sintering, the WC content in the PCD table is typically low and thus Co + W sum is a reasonable estimate of the cobalt content.

Table 5.4: Table showing the comparison in phase analysis between EDS and image analysis for layers 3 and 4.

Element	Weight%			
	Image Analysis		EDS	
	Layer 3 (2µm)	Layer 4 (0.5µm)	Layer 3 (2µm)	Layer 4 (0.5µm)
C	73 ± 1	61 ± 2	81	72
Co + W	27 ± 1	39 ± 2	19	28

Although EDS and image analysis offer different values, both techniques are in agreement that the 0.5µm layers contain more cobalt metal. This corresponds well with Miess and Rai [54] who found that the cobalt content in PCD is inversely proportional to the grain size. Even though the finer powder has smaller pores, it is known that when working with relatively fine grade incompressible ceramics, the finer the starting

powder, the higher the overall volume of the pores the green compact will have [83]. Since the pores are infiltrated by liquid cobalt during the heating stage of sintering, the finer grade diamond due to its higher porosity and smaller pore volume can by means of better wetting, uptake more cobalt into the PCD layer. Thus this will result in a higher residual cobalt concentration [83].

5.3.3.4 Defects

Several defects were observed with the laminate sample. The most obvious of which was the skew and non-continuous layers (Figure 4.30). This may be related to the speed of the incoming particles and effect of the stirring action in the cell. These defects would thus get progressively worse with the deposition of each consequent layer. A possible approach to achieving smoother and straighter layers would entail lowering the operating voltage and/or the concentration of the suspension so that slower deposition takes place. Decreasing the intensity of the stirring action during deposition may also help but at the expense of a higher settling rate.

The non-continuous layers were thought to be due to damage sustained to the green deposit during assembly into the coated niobium cup for sintering. Since the geometry of the cup tapers slightly at base, the deposit would suffer damage at the edges when pushed right to the end. A dramatized illustration of this is shown in Figure 5.7. This effect would be further enhanced during the cold compaction stage of the sintering process. A possible solution to this problem would be the use of straight-ended cups that do not have the tapering.

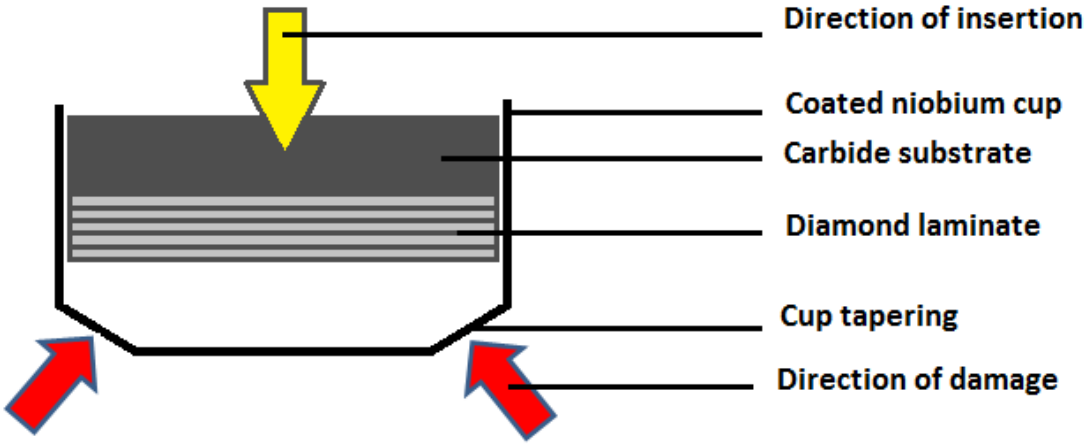


Figure 5.7: Illustration showing the effect of the cup tapering on the edges of the diamond laminate.

Another defect is the inclusion of coarser grains in the fine grade layers as shown in Figure 4.32. This was due to cross-contamination caused by the repeated movement of electrodes from one suspension to the other. Non-deposited particles adhered to the electrode holder and counter electrode from one suspension would be released when submerged into the other suspension. This phenomenon most likely also occurred with fine grade particles contaminating the coarse grade suspension, but evidence of this was not observed since the fine grade particles would dissolve and re-precipitate onto the larger particles during sintering. The cross-contamination of particles could possibly be reduced or eliminated by incorporating a washing step before each subsequent submersion of the electrodes into the other suspension. Such a washing procedure could involve dipping the electrodes into distilled water to allow contaminated particles to be liberated before submersion into the other suspension.

5.3.3.5 Fracture analysis

Crack propagation by means of the 3-point bend jig showed very little sign of crack deflection. The load-displacement curve for the laminate (Figure 4.34) is fairly smooth and does not show the jagged saw-tooth type graph expected for layered materials.

Similarly, inspection of the crack path under the microscope (Figure 4.33) shows no significant crack deflection. It is thought that the lack of deflection is caused by the thermal expansion mismatch of the carbide substrate and the diamond. Tungsten carbide has a higher thermal expansion co-efficient than the diamond (Table 5.5). Thus, during the cooling stage of the sintering cycle, the WC substrate will want to contract stronger than the diamond. However, due to the constraint of the diamond table, compressive stresses are generated at the diamond-carbide interface after sintering (Figure 5.8).

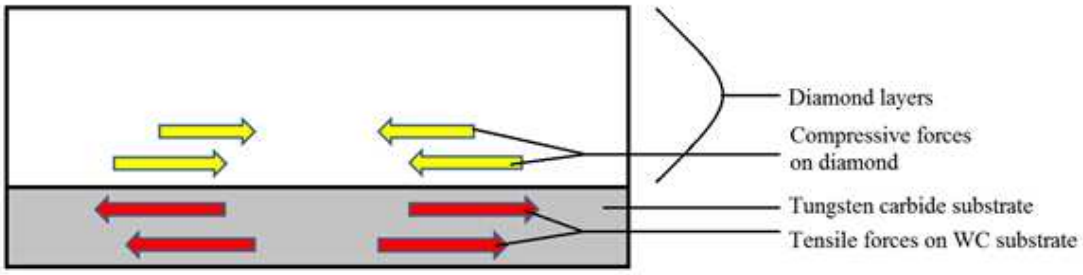


Figure 5.8: Schematic illustration of the compressive forces generated due to the mismatch in thermal expansion between the diamond and the substrate.

The compressive stress on the diamond at the vicinity of the diamond-carbide interface is likely to be higher than the residual stresses that exist between the individual diamond layers.

The residual stresses due to thermal mismatch $\sigma_{res,i}$ can be estimated by using Equation 5.3-1 [84] by assuming that the mismatch only results from different thermal strains of the different layers. Ideal elastic materials and neglecting the influence of external surfaces by considering infinitely long plates are further assumptions necessary to fulfil the requirements of the equation [84].

$$\boldsymbol{\sigma_{res,i}} = \frac{\boldsymbol{E_i}}{\boldsymbol{1-\nu_i}}(\bar{\boldsymbol{\alpha}} - \boldsymbol{\alpha_i})\Delta\boldsymbol{T}$$ Equation 5.3-1

Where E_i, α, and ν_i are the Young's modulus, thermal expansion co-efficient and Poisson's ratio of the i^{th} layer respectively and $\Delta T = T_o - T_{Ref}$ where T_{Ref} is the stress relax temperature during sintering (1000°C [49]) and T_o is room temperature. The term $\bar{\alpha}$ is defined as the averaged thermal expansion co-efficient of the laminate (Equation 5.3-2).

$$\bar{\boldsymbol{\alpha}} = \frac{\sum_{i=1}^{N}\frac{\boldsymbol{E_i t_i \alpha_i}}{\boldsymbol{1-\nu_i}}}{\sum_{i=1}^{N}\frac{\boldsymbol{E_i t_i}}{\boldsymbol{1-\nu_i}}}$$ Equation 5.3-2

Where t_i is the thickness of the i^{th} layer and N is the number of layers. By using the values listed in Table 5.5 , it is possible to calculate the residual stresses present in the sample. By using Equation 5.3-1, it is estimated that the diamond table would have a compressive stress of about 755MPa. This value is close to the value obtained by Chen et al. [49] who found through Finite Element Analysis (FEA) a maximum compressive stress at the interface to be 690MPa.

Table 5.5: Physical properties of PCD, WC-Co and Co.

Property	PCD	WC-Co	Co
E (GPa)	890 [85]	579 [85]	215 [86]
α (10^{-6} K^{-1})	4.5 [87]	5.2 [85]	16.8 [86]
ν	0.07 [85]	0.22 [85]	0.32 [86]

Since the physical properties of 0.5 and 2µm sintered diamond could not be found, the values were calculated by using the law of mixtures and the volume fractions of PCD

and Co obtained by image analysis. By using Equation 5.3-1, it was estimated that the 2µm layers experience a compressive stress of about 133MPa and the 0.5µm layers experience a tensile stress of about 160MPa. From these estimations, it is clear to see that the compressive stress existing in the diamond table as a result of the thermal mismatch with the substrate is much larger than the stress fluctuations in the individual diamond layers. As such, the crack would propagate without deflection near the substrate interface.

The compressive stress in the diamond table would become smaller further away from the interface. At a distance sufficiently far from the compressive forces of the interface, the energy of a propagating crack is likely to be much higher than the local stress fluctuations in the individual layers and thus no deflection would be seen here either.

Interestingly, crack deflection was found with a pre-existing crack in Figure 4.35. Due to the absence of cobalt in the crack, it can be assumed that it had developed during the cooling stage of the sintering cycle. This crack was found at the top of the sample opposite the carbide-diamond interface. Thus, it was sufficiently far from the compressive forces of the carbide substrate to show crack deflection. As was hypothesized in Section 2.6.2, the crack propagates straight through the 0.5µm layers and deflects just after entering the 2µm layers. This is due to the fact that the 0.5µm layers have higher cobalt content, thus these layers experience more tensile forces than the 2µm layers. However, upon entering the 2µm layer, the crack path begins to deflect from its original direction. This is due to the fact that this layer has lower cobalt content, causing this layer to experience more compressive stresses thus causing it to deflect. A schematic diagram showing the distribution of the expected stresses in the layers is shown in Figure 5.9.

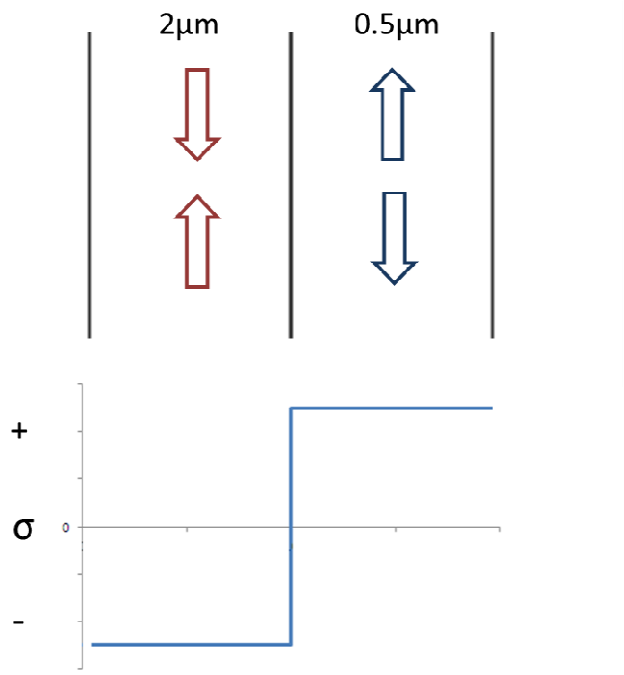


Figure 5.9: A schematic diagram showing the stress distribution in the layers.

From a biomimetic point of view, two aspects of mimicry were evident in this project. The first aspect considered is that in biological systems the forming techniques of the organisms are hard-coded in their genetic make-up and as a result, these organisms can use the body's resources to build new material. Thus biological systems will always have the advantage in that mild processing conditions are needed to achieve the desired outcomes. In this sense, EPD as a forming technique requires relatively mild conditions (room temperature and pressure) when compared with other traditional forming techniques such as cold compaction. The second biomimetic aspect was the intention for the microstructure to resemble that of nacre. In this regard, a layered structure could be formed using the EPD technology. Although the expected toughening mechanisms of nacre and diamond laminate are completely different, the idea for the latter material was conceived by inspiration from the former. As such, biomimetics may still play a promising and key role in the development and design of future materials.

6. Conclusion and recommendations

The purposes of the work presented in this project were:

- Firstly, to addresses the plausibility of making a diamond/diamond laminate structure using two different alternating grades of diamond by using EPD technology;
- Secondly, to deal with the ability to sinter the layered deposit such that a densified sample with functionally graded cobalt content is achieved;
- And lastly, to observe the layered sample for evidence of alternating residual stresses as evidence for crack deflection and thus possibly a tougher material.

To acquire the technology of EPD as well as develop a basic understanding of the technique, tests with alumina powder were conducted before experiments with the EPD of diamond were carried out. From these training experiments, EPD proved to be an effective shaping technique that allows homogenous packing of ceramic particles onto a substrate. Deposition parameters such as time, voltage and concentration allows for a reasonably precise control of weight of the coating.

With knowledge obtained from the alumina portion of the work, the deposition of diamond was investigated. Due to problems encountered with the organic suspensions of diamond particles, an aqueous suspension was chosen. Stable suspensions of diamond were achieved by changing the pH of the aqueous suspension to become alkaline. Any further surface-group modification of the diamond powder showed little improvement to the zeta potential in aqueous media. After optimization of the aqueous suspension, diamond could be deposited directly onto tungsten carbide substrates. An electric field of 1.25V/cm was sufficiently low to prevent bubble formation at the electrodes by electrolysis. However, having such a low driving force of the particles also affected the deposition rates which were low by literature standards. Multi-layer deposition was possible by submerging the electrode in out and of the respective suspensions.

The diamond laminate produced by EPD could be sintered in a HPHT press using DEC substrate and alumina-coated niobium cups without any AGG. The sintered sample had a total average thickness of 946µm with 2µm grade diamond layers having an average thickness of approximately 48 ± 1 µm and the 0.5µm having an average thickness of approximately 40 ± 1 µm. As hypothesized, the 0.5µm layers showed higher cobalt content than the 2µm layers as demonstrated by EDS and image analysis measurements.

In theory, the differing cobalt content of the diamond layers was expected to produce alternating residual stresses which would result in crack deflection. However, upon fracture analysis using 3-point bend strength measurement, very minimal crack deflection was observed. The load versus displacement graph obtained during the fracture did not show any of the typical saw-tooth plots evident in layered materials. It is thought that the compressive forces of the carbide substrate were sufficiently high to overcome the smaller residual forces within the layered material necessary for crack deflection. However, a pre-existing cooling crack was found, away from the carbide interface, which exhibited the expected crack deflection behaviour.

Considering the novelty of both the aqueous deposition of diamond as well as the sintering of diamond deposits produced by EPD, some defects in the material were expected. A more detailed investigation into defect control is necessary. Due to the constraints of time and resources, only one laminate was made for testing and analysis. Further optimisation of the deposition technique, the use of surfactant binder and the redesign of the sintering capsule are recommended. Additionally, quantitative exploration of different grades of diamond, layer control and the effect of the carbide substrate on crack deflection are also recommended. Future work done in this direction could yield a tougher diamond cutter.

7. Bibliography

[1] Ozbayraktar, S., *Element Six: Private communication*, 2008.

[2] Huang Y., Zan Q., Guo H., Cai S. Wang C., "Biomimetic structure design — a possible approach to change the brittleness of ceramics in nature," *Materials Science & Engineering C*, vol. 11, pp. 9-12, 2000.

[3] Lai M. J., Lin M. C., Chan C. C., Chiu S. C Tuan W. M., "The mechanical performance of alumina as a function of Grain size," *Materials Chemistry and Physics*, vol. 36, pp. 246-251, 1994.

[4] Rainforth W. M., Wadsworth T., Stevens R. Wang J., "The effect of notch width on the SENB toughness for oxide ceramics," *Journal of the European Ceramic Society*, vol. 10, pp. 21-31, 1992.

[5] Rowcliff D. J., Edington J. W. Henshall D., "Fracture toughness of single crystal silicon carbide," *Journal of the American Ceramic Society*, vol. 60, pp. 373-375, 1977.

[6] Swab J. J., Hill D. Quin G. D., "Fracture toughness by the surface crack in flexure (SCF) method: New results," *Ceramic Engineering and Science Proceedings*, vol. 18, pp. 163-172, 1997.

[7] Guillou M. O.,Henshall J. L. and Hooper R. M. Maersky C., "Indentation hardness and fracture toughness in single crystal TiC0.96," *Materials Science and Engineering A*, vol. 209, pp. 329-336, 1996.

[8] Quinn G. D. Getting R. J., "Surface Crack in Flexure (SCF) Measurement of the Fracture toughness of Advanced Ceramics," *Ceramic Engineering and Science Proceedings*, vol. 16, pp. 539-544, 1995.

[9] Baudin C. Osendi J. M. I., "Mechanical properties of mullite materials," *Journal of the European Ceramic society*, vol. 16, pp. 217-224, 1996.

[10] Aoki H., Kobayashi Y., Kamata K. Moriyama M., "The mechanical Properties of Hot-pressed TiN ceramics with various additives," *Journal of the Ceramic Society of Japan*, vol. 101, pp. 279-284, 1993.

[11] Cooper G. A. Tze-Pin Lin, "Measurement of the fracture toughness of polycrystalline diamond using the double-torsion test," *Journal of Materials Science*, vol. 29, pp. 4750-4756, 1994.

[12] Katti K. S., Katti D. R., "Why is nacre so tough and strong ?," *Materials Science& Engineering C*, vol. 26, pp. 1317 - 1324, 2006.

[13] Bramblett C. A. Steele D. G., *The Anatomy and Biology of the Human Skeleton*. Texas: Texas A&M University Press, 1988.

[14] Remizov S. M., Prujansky L. Y., Matveevsky R. M., "Wear Resistance and Microhardness of Human Teeth," *Journal of Engineering in Medicine*, vol. 205, no. 3, pp. 201-202, 1991.

[15] Tian X.P, Zhou B.L, "A biomimetic model of short fiber reinforced composite materials: I. Stress distribution of composite reinforced by dumbbell fibers," *Acta Metallurgica Sinica*, vol. 30, no. 4, pp. 180-186, 1994.

[16] Tian X.P, Zhou B.L, "A biomimetic model of short fiber reinforced composite materials: II. Strength theory of imperfect-bonding interface," *Acta Metallurgica Sinica*, vol. 30, no. 4, pp. 187-193, 1994.

[17] Jia X., Cheng H.M., Zhou B.L., Zheng G.B., Shen, Z.H., *'94 Fall Symposium of Chinese Materials Resources Society*, pp. 21–1353, 1994.

[18] Fu S.Y., Zhou B.L., Lung C.W, "On the pull-out of fibers with fractal-tree structure and the inference of strength and fracture toughness of composites," *Smart Materials and Structures*, vol. 1, pp. 180–185, 1992.

[19] Fu S.Y., Li S.H., He G.H., Zhou B.L., Lung C.W., "A study on branched structure fiber-reinforced composites," *Scripta Metallurgica et Materialia*, vol. 29, pp. 1541–1546, 1993.

[20] Mano J. F. Luz G. M., "Biomimetic design of materials and biomaterials inspired by the structure of nacre," *Philosophical Transactions of the Royal Society A*, vol. 367, pp. 1587-1605, 2009.

[21] Sarikaya, M., Gunnison, K. E., Yasrebi, M. Aksay, I. A., "Mechanical property–microstructural relationship in abalone shell," *Proceedings of the Materials Research Society Symposium*, vol. 174, pp. 109–116, 1990.

[22] Neves, N. M., Mano, J. F, "Further contributions on the structure/mechanical behaviourrelationships in crossed-lamellar sea shells," *Material Science Engineering C*, vol. 25, pp. 113–118, 2005.

[23] Phillipps A. J., Clegg W. J., Clyne T. W., "The failure of layered ceramics in bending and tension," *Composites*, vol. 25, no. 7, pp. 524-533, 1994.

[24] Sarkar P., Nicholson, P. S., "Electrophoretic deposition (EPD): mechanism,kinetics and application to ceramics," *Journal of the American Ceramic Society*, vol. 79, pp. 1987–2002, 1996.

[25] Van der Biest O., Vandeperre L., "Electrophoretic deposition of materials," *Annual Review of Materials Science*, vol. 29, pp. 327-352, 1999.

[26] Fischer, R., Fischer, E., De Portu, G., Roncari, E, "Preparation of ceramic micro-laminate by electrophoresis in aqueous system," *Journal of Materials*

Science Letters, vol. 14, no. 1, pp. 25-27, 1995.

[27] Van der Biest O., Vandeperre L., "Electrophoretic deposition of materials," *Annual Review of Materials Science*, vol. 29, pp. 327-352, 1999.

[28] Besra L., Liu M., "A review on the fundamentals and applications of electrophoretic deposition (EPD)," *Progress in Material Science*, vol. 52, pp. 1-61, 2007.

[29] Reed J. S., *Principles of Ceramics Processing*, 2nd ed. New York: Wiley InterScience, 1995.

[30] Besra L., Samantaray P., Bhattacharjee S., Singh B. P., "Electrophoretic deposition of alumina on stainless steel from non-aqueous suspension," *Journal of Materials Science*, vol. 42, pp. 5714-5721, 2007.

[31] Van der Biest O., Vandeperre L., Put S., Anné G., Vleugels J., "Laminated and functionally graded ceramics by electrophoretic deposition," *Advances in Science And Technology*, vol. 45, pp. 1075-1084, 2006.

[32] De Riccardis, M. F., Carbone, D., Rizzo, A., "A novel method for preparing and characterizing alcoholic EPD suspensions," *Journal of Colloid and Interface Science*, vol. 307, pp. 109-115, 2007.

[33] Clasen, R., "Electrophoretic deposition of compacts of nano-sized particles," *Science, Technology, and Applications of Colloidal Suspensions*, pp. 169-184, 1995.

[34] Valdes, J. L., Mitchel, J. W., Mucha, J. A., Seibles, L., Huggins, H., "Selected-Area Nucleation and Patterning of Diamond Thin Films by Electrophoretic Seeding," *Journal of the Electrochemical Society*, vol. 138, no. 2, pp. 635-636, 1991.

[35] Affoune A. M., Prasad B. L., Sato H., Enoki T., "Electrophoretic Deposition of Nanosized Diamond Particles," *Langmuir*, vol. 17, no. 2, pp. 547-551, 2001.

[36] Zhitomirsky, I., "Cathodic electrodeposition of diamond particles," *Materials Letter*, vol. 37, pp. 72-78, 1998.

[37] Neirinck B., Fransaer J., Vleugels J., Van der Biest O., "Aqueous Electrophoretic Deposition at High Electric Fields," *Key Engineering Materials*, vol. 412, pp. 33-38, 2009.

[38] Clegg W. J., Kendall K., Alford N., Button T. W., Birchall J. D., "A simple way to make tough ceramics," *Nature*, vol. 347, no. 455-457, 1990.

[39] Oechsner M., Hillman C., Lange F., "Crack bifurcation in laminar ceramic composites," *Journal of the American chemical society*, vol. 79, pp. 1834-1838, 1996.

[40] Nicholson P. S, Sarkar P., Huang X., "Electrophoretic deposition and its use to synthesize ZrO2 / Al2O3 micro-laminate ceramic / ceramic composites," *Journal of Materials Science*, vol. 28, pp. 6274-6278, 1993.

[41] You C., Jiang D. L., Tan S. H., "SiC / TiC laminated structure shaped by electrophoretic deposition," *Ceramics International*, vol. 30, pp. 813-815, 2004.

[42] Ferrari, B., Sánchez-Herencia, A.J., Moreno, R., "Aqueous electrophoretic deposition of AL2O3/ZrO2 layered ceramics," *Materials Letters*, vol. 35 , no. 5-6, pp. 370-374, 1998.

[43] Zhitomirsky I., Gal-Or L., "Formation of hollow fibers by electrophoretic deposition," *Materials Letters*, vol. 38, pp. 10–17, 1999.

[44] Vandeperre L. J, Van der Biest O., "Graceful failure of laminated ceramic tubes formed by electrophoretic deposition," *Journal of the European Ceramic*

Society, vol. 18, pp. 1915-1921, 1998.

[45] Katzman H., Libby W. F., "Sintering diamond compacts with a cobalt binder," *Science*, vol. 172, pp. 1132-34, 1971.

[46] Rocco R. H. and Wentorf W. A., Patent SAP 7315038, 1973.

[47] Semerchan L. F. and Veraschagin A., Patent UKP 1382080, 1975.

[48] McKie A., "PhD Thesis: Carbon enriched thermal sprayed hard metal coating used in PCD sintering," *University of the Witwatersrand*, 2011.

[49] Chen F., Xu G., Ma C.D., Gu G.P, "Thermal residual stress of polycrystalline diamond compacts," *Transactions of Nonferrous Metals Scoiety of China*, vol. 20, pp. 227-232, 2010.

[50] Gong S. W, Zhao F. J., "Failure analysis of polycrystalline diamond compact cutters for breaking rock by bending waves theory," *Journal of Central South University of Technology*, vol. 15, pp. 112-116, 2008.

[51] Shin T. J., Oh J. O., Oh K. H., Lee D. N., "The mechanism of abnormal grain growth in polycrystalline diamond during high pressure-high temperature sintering," *Diamond Related Materials*, vol. 13, pp. 488-494, 2004.

[52] Akaishi M., Ohsawa T., Amaoka S.Y , "Sythesis of fine-grained polycrystalline diamond compact and its imcrostructure," *Journal of the American Ceramic Society*, vol. 74, no. 1, pp. 5-10.

[53] Yu H.C. , Li S.J. , Hu E.L., "Sintering of ultrafine diamond particles under high temperature and high pressure," *Diamond and Related Materials*, vol. 3, 1994.

[54] Miess D., Rai G., "Fracture toughness and thermal resistance of polycrystalline diamond compacts," *Material Science and Engineering A*, vol. 209, pp. 270-

276, 1996.

[55] Matthias T.R, Patent GB 2462080, 2010.

[56] Slack G.A., Bartram S.F., "Thermal Expansion of Some Diamondlike Crystals," *Journal of Applied Physics*, vol. 46, no. 1, pp. 89-98, 1975.

[57] Touloukian Y. S., *Thermophysical Properties of Matter*. New York: IFI/Plenum, 1975, vol. 12.

[58] Munro R. G., "Evaluated Material Properties for a Sintered alpha-Al2O3," *Journal of the American Ceramic Society*, vol. 80, pp. 1919-1928, 1997.

[59] Bewilogua K., Richter F., "Vapor Phase Deposition of Cubic Boron," *Handbook of Ceramic Hard Materials*, vol. 1, p. 421, 2000.

[60] Clark C.D., Collins A.T., Woods G.S., *The Properties of Natural and Synthetic diamond*, Field J.E., Ed. London: Academic Press, 1992, ch. 2, p. 35.

[61] Stanishevsky A., Catledge S.A., Vohra Y., "Surface modification and functionalization of nanostructured carbons," *Journal of Achievements in Materials and Manufacturing Engineering*, vol. 37, no. 2, pp. 348-353, 2009.

[62] Remes Z., Kromka A., Kozak H. , Vanecek M., Haenen K. , Wenmackers S., "The infrared optical absorption spectra of the functionalized nanocrystalline diamond surface," *Diamond and Related Materials*, vol. 18, pp. 772-775, 2009.

[63] Li Y.L., Tero R. , Nagasawa T., Nagata T., Urisu T., "Deposition of 10-undecenoic acid self-assembled layers on H-Si (111) surfaces studied with AFM and FT-IR," *Applied Surface Science*, vol. 238, pp. 238-241, 2004.

[64] Liu H.B., Xiao S.J., Chen Y.Q. , Chao J. , Wang J. , Wang Y. , Pan Y. , You X. Z , Gu Z.Z., "Grazing angle mirror-backed reflection (GMBR) for infrared

analysis of monolayers on silicon.," *Journal of Physical Chemistry B Letters*, vol. 110, no. 36, pp. 17702-17705, 2006.

[65] Zhu Y., Xu F., Shen J., Wang B., Xu X., "Study on the modification of nanodiamond with DN-10," *Journal of Material Science Technology*, vol. 23, no. 5, pp. 599-603, 2007.

[66] Shergold H. L, Hartley C.J., "The surface chemistry of diamond," *International Journal of Mineral Processing*, vol. 9, pp. 219-233, 1982.

[67] Xu N.S., Chen Jian, Deng S.Z., "Effect of heat treatment on the properties of nano-diamond under oxygen," *Diamond and Related Materials*, vol. 11, pp. 249–256, 2002.

[68] Van Tassel J. J., "PhD Thesis: Electrophoretic deposition: fundamentals, mechanisms and examples with an in depth examination of the ion depletion effect," *The Pennsylvania State University*, 2004.

[69] Anne G., Vanmeensel K., Vleugels J., Van der Biest O., "A mathematical description of the kinetics of the electrophoretic deposition process for Al203-based suspensions," *Journal of the American Ceramic Society*, vol. 88, no. 8, pp. 2036–2039, 2005.

[70] Sarkar P., De D., Rho H., "Synthesis and microstructural manipulation of ceramics by electrophoretic deposition," *Journal of Materials Science*, vol. 39, no. 3, pp. 819–823, 2004.

[71] Maca K., Hadraba H., Cihlar J., "Electrophoretic deposition of alumina and zirconia: I. Single-component systems," *Ceramics International*, vol. 30, pp. 843-852, 2004.

[72] Basu R.N., Randall C.A., Mayo M.J., "Fabrication of dense zirconia electrolyte

films for tubular solid oxide fuel," *Journal of the American Ceramic Society*, vol. 84, pp. 33-40, 2001.

[73] Krell A., Blank P., "The influence of shaping method on the grain size dependence of strength in dense submicrometre alumina," *Journal of rhe European Ceramic Society*, vol. 16, pp. 1189-1200, 1996.

[74] Zhukov A. N., Zviaguilskaya, Y.V., Benndorf, C., "Effect of the surface conductance on electrokinetic potential calculated from electrophoretic mobilities of the diamond particles in ethanol electrolyte solutions ," *Colloids and Surfaces A: Physicochemical and Engineering Aspects*, vol. 222, pp. 341-348, 2003.

[75] Xu X., Yu Z., Zhu Y., Wang B., "Effect of sodium oleate adsorption on the colloidal stability and zeta potential of detonation synthesized diamond particles in aqueous solutions," *Diamond and Related Materials*, vol. 14, pp. 206– 212, 2005.

[76] Masilela C., Dzepina B., Sigalas I., "Surface modification of diamond powder for electrophoretic deposition," *University of the Witwatersrand*, 2011.

[77] Panitz J. K. G., Tallant D. R., Hills C. R., Staley D. J., "Properties of chemical vapor infiltration diamond deposited diamond powder matrix," *Journal of Vacuum Science & Technology A: Vacuum, Surfaces & Films*, vol. 12, no. 4, pp. 1480-1486, 1994.

[78] Yuan H., Cheow P. S., Ong J., Toh C. S., "Characterization of the electrophoretic mobility of gold nanoparticles with different sizes using the nanoporous alumina membrane system," *Sensors and Actuators B: Chemical*, vol. 134, pp. 127-132, 2008.

[79] Raissi B., Marzbanrad E. , Gardeshzadeh A.R., "Particle size separation by

alternating electrophoretic deposition," *Journal of the European Ceramic Society*, vol. 29, pp. 3289–3291, 2009.

[80] Abdoli H., Zarabian M., Alizadeh P., Sadrnezhaad S.K., "Fabrication of aluminum nitride coatings by electrophoretic deposition:Effect of particle size on deposition and drying behavior," *Ceramics International*, vol. 37, pp. 313–319, 2001.

[81] Hyam R.S., Subhedar K.M., Pawar S.H., "Effect of particle size distribution and zeta potential on the electrophoretic deposition of boron films," *Colloids and Surfaces A: Physicochemical Engineering Aspects*, vol. 315, pp. 61-65, 2008.

[82] Corni I., Ryan M. P., Boccacini A. R., "Electrophoretic deposition: From traditional ceramics to nanotechnology," *Journal of the European Ceramic Society*, vol. 28, pp. 1353–1367, 2008.

[83] "Proprietary knowledge: Element Six, Private communication".

[84] Sestakova L., Bermejo R., Chlup Z., Danzer R., "Strategies for fracture toughness, strength and reliability optimisation of ceramic-ceramic laminates," *International Journal of Materials Research*, vol. 102, no. 6, pp. 613-626, 2011.

[85] Paggett J.W., Drake E.F., Krawitz A.D., Winholtz R.A., Griffin N.D., "Residual stress and stress gradients in polycrystalline diamond compacts," *International Journal of Refractory Metals and Hard Materials*, vol. 20, pp. 187-194, 2002.

[86] Betteridge W., "The properties of metallic cobalt," *Progress in Materials Science*, vol. 24, pp. 51-142, 1979.

[87] Reeber R.R., Wang K., "Thermal expansion, molar volume and specific heat of diamond from 0 to 3000K," *Journal of Electronic Materials*, vol. 25, pp. 63-67,

1996.

[88] Anné G., Neirinck B., Vanmeensel K., Van der Biest O., Velugels J., "Influence of electrostatic interactions in the deposit on the electrical field strength during electrophoretic deposition," *Key Engineering Materials,* vol. 314, pp. 181-186, 2006.

[89] Zhang J., Li H., Zhou Z., Chen G., Song Z., "Study on micro-hardness and wear resistance of human tooth at different depth".